Charakterisierung von Natriumsignalen in neuronalen Kompartimenten

Inaugural-Dissertation

zur Erlangung des Doktorgrades der
Mathematisch-Naturwissenschaftlichen Fakultät
der Heinrich-Heine-Universität Düsseldorf

vorgelegt von

Christian Kleinhans

aus Bochum

Düsseldorf, 2016

aus dem Institut für Neurobiologie

gedruckt mit Genehmigung

der Mathematisch-Naturwissenschaftlichen Fakultät

der Heinrich-Heine-Universität Düsseldorf

Gutachter:

Prof. Dr. rer. nat. Christine Rose, Heinrich-Heine-Universität Düsseldorf

Prof. Dr. rer. nat. Kurt Gottmann, Heinrich-Heine-Universität Düsseldorf

Tag der mündlichen Prüfung: 23.06.2016

„Wenn ein unordentlicher Schreibtisch

ein Zeichen für einen unordentlichen Geist ist,

was sollen wir dann von einem leeren Schreibtisch denken?“

Albert Einstein

Inhalt

1 Zusammenfassung

Die Aufrechterhaltung einer definierten Ionenverteilung zwischen Intra- und Extrazellulärraum im Gehirn und der daraus folgende elektrochemische Gradient über die Zellmembran ist die Grundvoraussetzung jedes kognitiven Vorganges. Der Natriumgradient im Besonderen dient als Triebfeder einer Vielzahl an Prozessen in Neuronen. Die elektrische Funktion von Nervenzellen wird durch transiente Depolarisation der Zellmembran ermöglicht, die durch einen Natriumeinstrom via liganden- oder spannungsaktivierte Ionenkanäle vermittelt und durch den elektrochemischen Gradienten getrieben wird. Insofern hat das Verhalten von Natrium in der Zelle und die Wechselwirkung mit der intrazellulären Umgebung unmittelbare Auswirkung auf die momentane Signalverarbeitung in Neuronen.

Die Depolarisation durch Natrium ist darüber hinaus eng verknüpft mit dem Einstrom sekundärer Botenstoffe wie Calcium. Dadurch spielt Natrium eine Vermittlerrolle bei vielen nachgeschalteten Prozessen wie synaptischer Plastizität und ist mittelbar für die Adaption synaptischer Strukturen verantwortlich.

Mithilfe von Zwei-Photonen-Imaging eines natriumsensitiven Farbstoffs, unter Verwendung von Patch-Clamping sowie verschiedener Stimulationsmethoden konnte in dieser Arbeit eine qualitative und quantitative Beschreibung von Natriumsignalen vorgenommen werden. Dabei lag der Fokus auf kleinsten neuronalen Strukturen, auf Dendriten und Spines.

Erstmalig wurden Natriumsignale in Spines und Dendriten in Abhängigkeit von deren Morphologie charakterisiert. Insbesondere der Spine Neck verhielt sich in Abhängigkeit seiner Geometrie als Diffusionshindernis, das die Natriumtransienten dämpfte und verzögerte. In Übereinstimmung mit diesen Resultaten lag der experimentell ermittelte apparente Diffusionskoeffizient deutlich unter den in anderen Arbeiten angegebenen Werten, die in größeren Strukturen bestimmt wurden. Die Befunde konnten des Weiteren in einer numerischen Simulation vollumfänglich bestätig werden. Zusammengenommen ist dies ein starkes Indiz für eine biochemische Kompartimentierung von Natrium in Spines und impliziert potentielle Auswirkungen sowohl auf die Anpassung der diffusiven Isolation einzelner Spines durch den Spine Neck als auch auf die elektrische Signalintegration einzelner Synapsen. Eine solche Kompartimentierung konnte bisher lediglich für Calcium gezeigt werden und stellt in Bezug auf Natrium eine entscheidende, neue Erkenntnis dar.

Die in dieser Arbeit präsentierten Erkenntnisse sind ein Beitrag zum tieferen Verständnis der Funktion der elementaren signalverarbeitenden Einheiten im Gehirn. Es konnten erstmals starke Hinweise auf die Existenz einer Natriumkompartimentierung in Spines gezeigt werden. Darüber hinaus legen die Resultate den Schluss nahe, dass der Beitrag einzelner Synapsen zur Zellkommunikation durch Anpassung der Spinegeometrie reguliert werden kann.

2 Abstract

Maintenance of a well-defined distribution of ions between extra- and intracellular space in the brain and the consequential electrochemical gradient across the cell membrane is constitutive of every cognitive capacity.

The sodium gradient in particular fuels a multitude of neuronal processes. Transient cell membrane depolarization as a consequence of sodium influx upon ligand- or voltage-gated opening of ion channels is the foundation of electric signaling. Thus, the behavior of intracellular sodium and its interplay with the cellular environment directly affects the ongoing signal processing in neurons.

Moreover, depolarization via sodium is closely linked to influx of second messengers such as calcium. Thus, many downstream mechanisms, e.g. synaptic plasticity, are mediated by sodium. As a result, sodium has an indirect influence on the adaptation of synaptic structures.

By means of sodium sensitive two-photon imaging combined with patch-clamping techniques and various stimulation procedures, we have qualitatively and quantitatively described sodium signals in neurons. In particular, we focused on spines and dendrites, the smallest neuronal subdomains.

For the first time, the dependency of sodium transients on the morphology of these host structures was assessed. Spine necks acted as diffusional barriers which, determined by their geometry, dampened and delayed sodium signals. In accordance with these findings, we have determined an apparent diffusion coefficient which is notably smaller than those shown in other studies that were performed in larger structures. Additionally, our results were confirmed by numerical simulations to its full extent. This strongly indicates a biochemical compartmentalization of sodium in spines and implies potential effects on the regulation of diffusional isolation as well as on electrical integration of single synapses. So far, such a compartmentalization has only been shown for Calcium and represents novel insight with regard to sodium.

The results presented in this work are a contribution to understanding the basic functional units of signal processing in the brain. For the first time, experimental evidence on a compartmentalization of sodium in spines is provided. Furthermore, a possible regulation of the contribution of single synapses to cell communication by adapting the spine geometry is conceivable.

3 Fragestellung

Die morphologischen Aspekte hippocampaler Zellen, besonders der CA1-Pyramidenzellen, sind wissenschaftlich gut beschrieben (siehe Kapitel 5). Ihre Synapsen, die großen Einfluss auf viele kognitive Leistungen haben, sind bereits seit Langem im Fokus der Neurowissenschaften. Die Erforschung der physiologischen Funktion dieser synaptischen Strukturen ist zum Teil weit fortgeschritten. Ein Beispiel sind neuronale Calciumsignale, deren grundlegende Parameter und funktionale Folgen insbesondere im Hinblick auf synaptische Plastizität experimentell und theoretisch in einer Vielzahl an Publikationen abgehandelt worden sind (siehe Kapitel 6). Allerdings sind diese Aspekte für Natrium größtenteils nicht bekannt. Der Natriumgradient über die Zellmembran dient als Triebfeder vielfältiger neuronaler Prozesse, allen voran der Bildung elektrischer Signale während synaptischer Aktivität. Folglich stellen Natriumsignale, also ein Einstrom von Natrium in das Zellinnere bei Öffnung von meist glutamatergen Ionenkanälen, den Hauptmediator einer temporären, lokalen Zellmembrandepolarisation dar. Ihnen fällt somit eine Kernrolle bei der Funktion von Neuronen und des Gehirns zu.

Insbesondere das Verhalten von Natrium in Mikrodomänen wie Spines und Dendriten hat großen Einfluss auf die Signalintegration in der Zelle (siehe Kapitel 6.3). Kenngrößen wie der Diffusionskoeffizient von Natrium, die Amplitude, Anstiegs- und Abfallkinetik von Natriumsignalen in den erwähnten Domänen und ihre Beeinflussung durch morphologische Gegebenheiten sind von fundamentalem Interesse. Die genannten Aspekte werden in dieser Arbeit qualitativ und quantitativ beleuchtet. In akuten, hippocampalen Gewebeschnitten wurden mithilfe von Zwei-Photonen Fluoreszenzimaging und des Natriumindikatorfarbstoffes SBFI Natriumsignale aufgezeichnet und analysiert. Einzelne Zellen wurden mithilfe der Patch-Clamp-Technik mit Farbstoff gefüllt und elektrophysiologisch untersucht.

Die wichtigsten Techniken sollen im Folgenden kurz erläutert werden.

4 Natriumimaging

4.1 Zwei-Photonen-Imaging

Fluoreszenzimaging in lebendem biologischem Gewebe stellt in vielerlei Hinsicht eine Herausforderung dar. Die wichtigsten limitierenden Faktoren sind dabei die Eindringtiefe des verwendeten Lichts in die Probe, der potentiell zellschädigende Energieeintrag in das Gewebe, das beugungsbegrenzte räumliche Auflösungsvermögen sowie die zeitliche Auflösung, die von der verwendeten mikroskopischen Technik abhängt.

In dieser Arbeit wurde vorrangig auf die Zwei-Photonen-Fluoreszenzmikroskopie (2PLSM, *Two-Photon Laser Scanning Microscopy*) zurückgegriffen, die für die Erfordernisse sehr gut geeignet ist. Der gesamte Messstand, der dazu zum Einsatz kam, ist in (Kleinhans et al., 2014) ausführlich beschrieben.

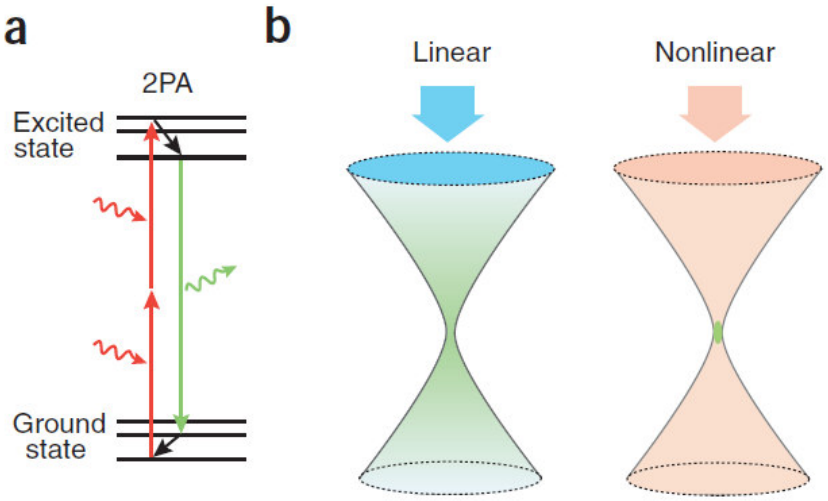

Abbildung 1: Nichtlineare optische Effekte beim 2PLSM. (a) Jablonski-Diagramm einer Zwei-Photonen-Absorption. Zwei gleichzeitig eintreffende Photonen halber Energie des Übergangs versetzen das Molekül in einen angeregten Zustand, das daraufhin unter Aussendung eines Photons spontan relaxiert. (b) Bei konfokaler Fluoreszenzmikroskopie emittiert in der Probe ein großer Bereich entlang des Strahlengangs (links, in grün dargestellt), während dieser Bereich bei der 2PLSM fast ausschließlich auf den Brennpunkt begrenzt ist (rechts). Modifiziert aus (Helmchen and Denk, 2005).

Die Zwei-Photonen-Technik beruht auf dem Phänomen, dass ein Fluorophor anstelle eines einzelnen Photons einer geeigneten Wellenlänge vereinfacht ausgedrückt ebenso zwei koinzident (i.e. innerhalb von ~0.5 fs) eintreffende Photonen der doppelten Wellenlänge (und somit der halben Energie) absorbieren kann, bevor es zur Fluoreszenz

kommt (siehe Abbildung 1a). Die Wahrscheinlichkeit für diesen Vorgang wird von vielen Parametern beeinflusst, ist aber sehr gering. Daher sind für eine ausreichende Fluoreszenz hohe Lichtintensitäten erforderlich, die in der Praxis nur mit gepulsten Lasern erreicht werden (Diaspro et al., 2006). Ebenso beschränkt sich der Bereich solcher hohen Intensitäten (und infolgedessen der effektiven Anregung und Emission) auf ein sehr geringes fokales Volumen um den Brennpunkt herum (siehe Abbildung 1b), wodurch sich speziell die räumliche Auflösung entlang der Achse des Lichtpfades verbessert. Zusätzlich bleiben ein hoher Energieeintrag und potentielle phototoxische Effekte auf ebendieses Volumen begrenzt (Diaspro et al., 2006). Erstmalig umgesetzt wurde die 2PLSM durch Denk und Strickler (Denk et al., 1990). Seitdem fand die Technik immer mehr Anwendung, was zu einem exponentiellen Anstieg der Veröffentlichungen führte, in denen sie zum Einsatz kam (Zipfel et al., 2003).

Die im Fokus stehenden, subzellulären Strukturen wie Dendriten und deren Spines haben eine Ausdehnung in der Größenordnung von wenigen Mikrometern, teils sogar darunter (siehe Kapitel 5.1). Die beugungsbegrenzte, räumliche Auflösungsgrenze für konventionelle Lichtmikroskopie beträgt bei 800 nm, einer typischerweise genutzten Anregungswellenlänge, $\lambda/2NA \approx 400$ nm (Hell, 2007). Für den Fall, dass hauptsächlich die Morphologie der betreffenden zellulären Strukturen beurteilt werden soll, kommt der zeitlichen Auflösung wiederum eine nachrangige Bedeutung zu. Da in der vorliegenden Arbeit vor allem intrazelluläre Natriumsignale mit einem natriumsensitiven Farbstoff mittels Fluoreszenzimaging untersucht wurden, war zudem eine hohe Bildgebungsfrequenz gefordert. Bei Raumtemperatur zeigen synaptisch induzierte Natriumsignale eine Zeitkonstante von etwa 10 s (Rose et al., 1999; Rose and Konnerth, 2001). Da in vielen Fällen allerdings die ansteigende Phase des Signals von Interesse ist, muss die Framerate deutlich unter einer Sekunde liegen. Mit dem hier verwendeten Zwei-Photonen-Fluoreszenzmikroskop sind räumlich betrachtet zweidimensional (als Zeitserie einer Bildebene) höchstens Samplingraten von 10 Hz, eindimensional (im Line-Scan-Modus) allerdings bis zu 700 Hz möglich (siehe Kapitel 8.1).

Oftmals liegt die untersuchte Region in akuten Gewebeschnitten nicht an der Oberfläche der Probe, sondern zwischen 20 und 80 µm darunter. Einer der Hauptvorteile der Zwei-Photonen-Mikroskopie im Vergleich zu konfokalen oder Weitfeld-Techniken liegt in der

möglichen Eindringtiefe des verwendeten Anregungslichts. Bei dem hier vorrangig verwendeten Farbstoff SBFI liegt die Anregungswellenlänge im UV-Bereich bei etwa 340-380 nm. In diesem Fall läge also die Laserwellenlänge (aufgrund der Addition der Energien zweier Photonen) bei ca. 700-800 nm. Die Eindringtiefe des einfallenden Lichts wird begrenzt durch Absorptions- und Streuungseffekte, wobei erstere in biologischem Gewebe nur eine Nebenrolle spielen. Letztere werden besonders durch Inhomogenitäten im Brechungsindex entlang des Lichtpfades hervorgerufen, die in Gewebeschnitten umso stärker sind (Diaspro et al., 2006). Das Ausmaß der Streuungsphänomene ist proportional zu $1/\lambda^4$ und somit stark von der Wellenlänge abhängig (Helmchen and Denk, 2005). Die mittlere freie Weglänge, also die durchschnittliche Strecke bis zu einem Streuungsvorgang, liegt bei Gehirngewebe für eine Wellenlänge von 800 nm bei etwa 200 µm und unterscheidet sich zwischen Präparationen und Gehirnregionen. Die daher deutlich höhere mögliche Imagingtiefe stellt einen weiteren Vorteil der 2PLSM im Vergleich zu anderen Verfahren dar, der sogar *in vivo* Imaging im lebenden Organismus zulässt (Stosiek et al., 2003).

Je nach Anwendungsgebiet bieten sich teils Alternativen zur 2PLSM an. So sind mit kamerabasierten Weitfeld-Imagingsystemen weitaus höhere Aufnahmeraten zu erzielen (Baranauskas et al., 2013), da die Probe nicht mit einem Laser Zeile für Zeile abgerastert, sondern ganze Bilder des Sichtfeldes verarbeitet werden. Dadurch ist bei entsprechender Färbung, zum Beispiel mit initial zellmembrangängigen Farbstoffen über das Bad oder als Bolusfärbung (Schreiner and Rose, 2013), das gleichzeitige Beobachten mehrerer Zellen eines Netzwerkes möglich. Dabei muss allerdings ein deutlicher Auflösungsverlust hingenommen werden, sodass einzelne Dendriten meist nicht mehr sichtbar sind. Eine durch kürzere Wellenlängen des Anregungslichts etwas höhere Auflösung kann, bei Einbußen in der Imagingtiefe, mit konfokaler Laserscanningmikroskopie erzielt werden.

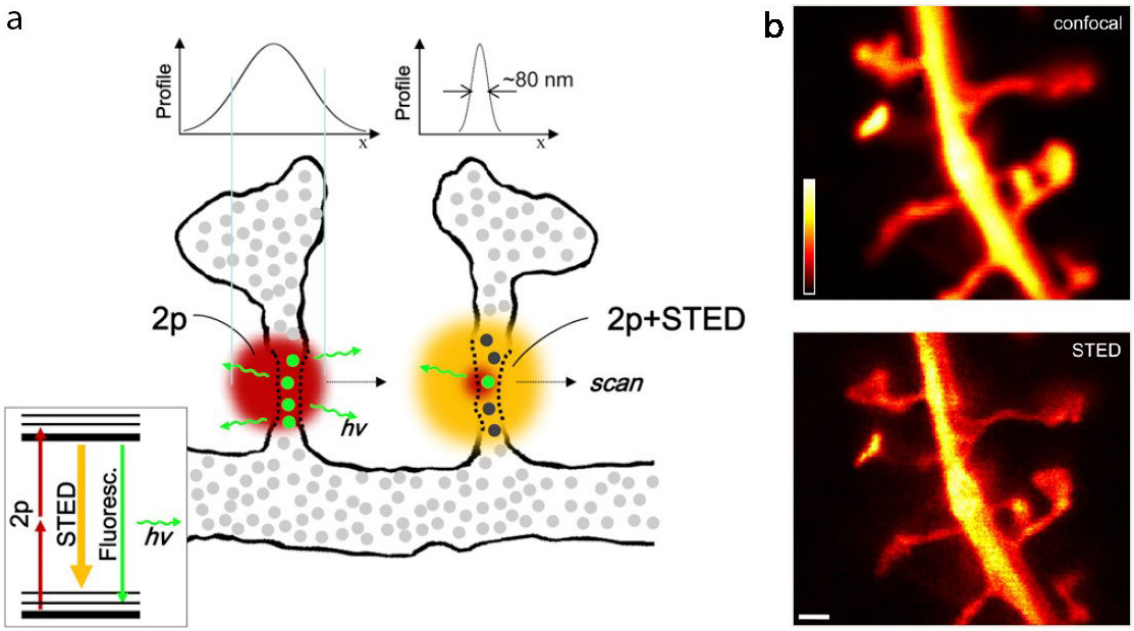

Abbildung 2: Fluoreszenzmikroskopie von dendritischen Strukturen. (a) Schema zweier dendritischer Spines, darüber das Fluoreszenzprofil quer über dem Spine Neck. Links: Anregung mit einem Nahinfrarotlaser. Die Halbwertsbreite des Intensitätsprofils ist wesentlich breiter als der Spine Neck. Rechts: STED-Mikroskopie, bei der nach Exzitation mit einem Nahinfrarotlaser die Fluoreszenz mit einem zweiten Laserstrahl kürzerer Wellenlänge in einem doughnutförmigen Bereich (hier gelb dargestellt) unterdrückt wird. Übrig bleibt ein Fluoreszenzsignal aus einem wesentlich kleineren Bereich. Unten links: Im skizzierten Jablonski-Diagramm wird das STED-Prinzip veranschaulicht. Zwei koinzidente infrarote Photonen regen das Molekül an; in einem räumlich eingeschränkten Bereich werden Fluoreszenzmoleküle durch induzierte Emission unterdrückt, die übrigen Moleküle relaxieren spontan unter Aussendung der bildgebenden Fluoreszenz. (Loew and Hell, 2013). (b) Aufnahmen derselben Dendriten und Spines mit konfokalem (oben) oder STED-Laserscanningmikroskop. Maßstabsbalken: 0,5 µm. Modifiziert aus (Nagerl et al., 2008).

Sollen noch kleinere Strukturen dargestellt werden, kommen lichtmikroskopisch nur noch sogenannte nicht-beugungsbegrenzte Verfahren in Frage (Yamanaka et al., 2014).

Das von diesen bei lebenden Präparaten am vielseitigsten Einsetzbare ist die STED-Mikroskopie (*Stimulated Emission Depletion*), die eine Lateralauflösung bis circa 50 nm ermöglicht (siehe Abbildung 2). Auf diese Weise konnte etwa die Plastizität neuronaler Spine Necks (siehe Kapitel 6.3) bei Stimulation einzelner Synapsen beobachtet werden (Nagerl et al., 2008; Tønnesen et al., 2014). Für die Erfindung dieser Methode erhielt Stefan Hell 2014 den Nobelpreis für Chemie (Nobelprize.org, 2014).

4.2 Deconvolution

Die Bildgebung an einem (Fluoreszenz-) Mikroskop besteht mathematisch aus einer Faltungsfunktion der Form

$$g = f \otimes h,$$

wobei g das aufgenommene Bild, f ein ideales Abbild der Probe, h die Punktabbildfunktion oder auch Punktspreizfunktion (PSF) und $\otimes$ die Faltungsoperation darstellen. Die PSF ist durch viele Einflussfaktoren bestimmt, so zum Beispiel durch Beugung an Blenden, optische Inhomogenität von Gewebe, Einflüsse des Sensors und andere Abbildungsfehler und verzerrt so das Abbild der Probe (Dao et al., 2015). Wird die PSF nun experimentell oder theoretisch bestimmt und ein Bild aufgenommen, kann durch eine

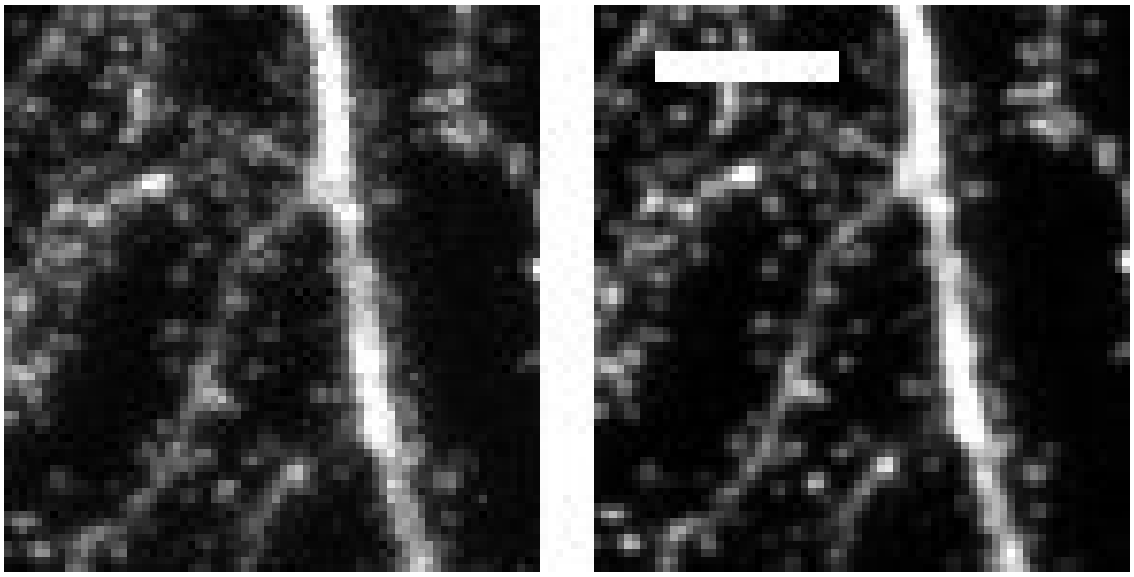

Abbildung 3: Beispiel für Deconvolution. Projektion eines z-Stapels aus 161 optischen Schnitten einer Dicke von 0.2 µm eines Dendriten einer hippocampalen CA1-Pyramidenzelle. Auch in x-y-Richtung wurde die Aufnahme mit einer spezifischen Auflösung von 0,2 µm / Pixel überabgetastet, was für die Entfaltungsprozedur von Vorteil ist. Die Zelle wurde per Patch-Clamping mit dem Farbstoff Alexa 488 gefüllt. Links die Ausgangsaufnahme, rechts das Ergebnis nach Deconvolution mit der Software „Huygens Professional" (Scientific Volume Imaging B.V., Hilversum, Niederlande). Sowohl Signalqualität als auch Auflösungsvermögen, besonders im Bereich der Spines, zeigen Verbesserung. Maßstabsbalken: 5 µm.

computergestützte Invertierung der ursprünglichen Faltung, der sogenannten Entfaltung oder Deconvolution, das ideale Abbild der Probe näherungsweise bestimmt werden. Dabei handelt es sich nicht um eine willkürliche Bildbearbeitung, sondern um eine numerische Restauration, die eine Verbesserung in der Bildauflösung und dem Hintergrundrauschen liefert (Periasamy et al., 1999).

In dieser Arbeit kam Deconvolution insbesondere zur Restauration der z-Stapel aus mehreren optischen Schnitten zum Einsatz (siehe Abbildung 3), um kleine Strukturen wie Spines in der bestmöglichen Auflösung und Signalqualität darzustellen und zu analysieren.

4.3 Der Farbstoff SBFI als Natriumindikator

Um intrazelluläre Natriumsignale detektieren zu können, ist ein Fluoreszenzfarbstoff vonnöten, dessen spektrale Eigenschaften sich bei Veränderung der Na^+-Konzentration ändern. Dieser muss, um als Sensor für Natrium zu fungieren, in der Zelle vorliegen. Im Falle des hier verwendeten Farbstoffs *Sodium-Binding Benzofuran Isophtalate* (SBFI) bestehen dazu zwei Möglichkeiten. Zum einen können einzelne Zellen über eine

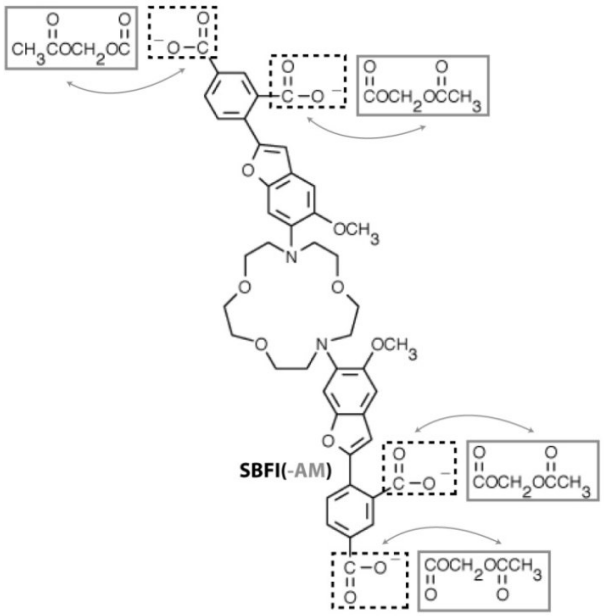

Abbildung 4: Die chemische Struktur von SBFI. In den grauen Kästen ist die funktionelle AM-Gruppe gezeigt, die die Membranpermeabilität ermöglicht und nach Eintritt in die Zelle von Enzymen abgespalten wird. Bei Verwendung des K+-Salzes dieses Farbstoffs ist die AM-Gruppe nicht vorhanden (Schreiner and Rose, 2013).

Patchpipette direkt mit dem gelösten, zellmembranimpermeablen K^+-Salz des Fluorophors beladen werden. Dadurch kann bei ausreichender Ladezeit und somit vollständiger Dialyse des Cytosols mit einer künstlichen, SBFI enthaltenden Intrazellulärlösung die Konzentration des Natriumsensors vorgegeben werden (üblicherweise etwa 1 mM). Zum anderen besteht die Möglichkeit, eine ganze Zellpopulation zu färben. Dazu wird ein Acetoxymethylester- (AM-) Derivat des

Farbstoffes verwendet, der lipophil und unpolar ist und folglich Membranpermeabel (siehe Abbildung 4). Über Perfusion der Probe oder eine lokale Druckapplikation angewandt, gelangt der Farbstoff in die Zellen, woraufhin cytosolische Esterasen den lipophilen Teil abspalten und er in der Zelle verbleibt (Schreiner and Rose, 2013).

SBFI wird im Ultravioletten angeregt, wobei das Absorptionsspektrum recht breit ist und von etwa 300 bis 400 nm reicht. Die spektralen Eigenschaften *in vitro* und *in situ* unterscheiden sich stark (Baartscheer et al., 1997), weswegen hier im Besonderen auf die Situation *in situ* eingegangen werden soll. Die Emission ändert sich chemisch bedingt vom ungebundenen zum gebundenen Zustand, sodass mit steigender Natriumkonzentration bei konstanter Farbstoffkonzentration die Fluoreszenzintensität in der Zelle abnimmt. Dies geschieht im Bereich bis etwa 50 mM näherungsweise linear, obwohl grundsätzlich eine Michaelis-Menten-Kinetik vorliegt (Karus et al., 2015a). Bei anderen Natriumindikatorfarbstoffen wie etwa CoroNa Green vergrößert sich im Vergleich die Emissionsintensität bei steigender Natriumkonzentration. Dadurch ist es möglich, relative Natriumänderungen zu detektieren (siehe Abbildung 5). Eine Besonderheit von SBFI ist es, dass auch bei Verschiebung der Anregungswellenlänge eine Änderung der Emissionseigenschaften eintritt. Am sogenannten isosbestischen Punkt (bei ca. 340 nm) ist infolgedessen kaum Natriumsensitivität (Meier et al., 2006). Dies ermöglicht ratiometrisches Imaging, wobei abwechselnd bei einer maximal natriumsensitiven Wellenlänge und am isosbestischen Punkt angeregt und die Emission detektiert wird (siehe Abbildung 5). Danach wird der Quotient aus beiden Signalen gebildet, der unabhängig von der absoluten Konzentration des Farbstoffes ist. Dadurch können Verfälschungen eines Experiments durch Störfaktoren wie Bleichen des Fluorophors oder kleine Bewegungen der Probe umgangen werden.

Die Affinität des Farbstoffs zu Natrium wird durch die Dissoziationskonstante K_D beschrieben, bei der im Mittel die Hälfte der Farbstoffmoleküle gebunden vorliegt. Der K_D von SBFI beträgt etwa 26 mM (Rose et al., 1999; Meier et al., 2006). Dadurch ist der Farbstoff gut geeignet, um Natriumänderungen im physiologischen Bereich zu messen. Die Ruhekonzentration beträgt intrazellulär ca. 13 mM (Kelly and Rose, 2010; Azarias et al., 2012), während bei neuronaler Aktivität transiente Natriumerhöhungen um die 20 mM auftreten können (siehe Kapitel 6.1). Die Affinität des Farbstoffes zu anderen

einwertigen Kationen ist um ein Vielfaches geringer als für Natrium (Minta and Tsien, 1989), wodurch Beeinflussung der Resultate, zum Beispiel durch hohe Kaliumkonzentrationen in der Zelle, minimiert werden. Aufgrund des geringen Verhältnisses von Farbstoffkonzentration zu Natriumkonzentration und des K_D für die SBFI:Na^+-Reaktion kann die Pufferung von Na^+ durch Bindung an den Farbstoff und daraus resultierender Verzerrung der Signale vernachlässigt werden (Fleidervish et al., 2010).

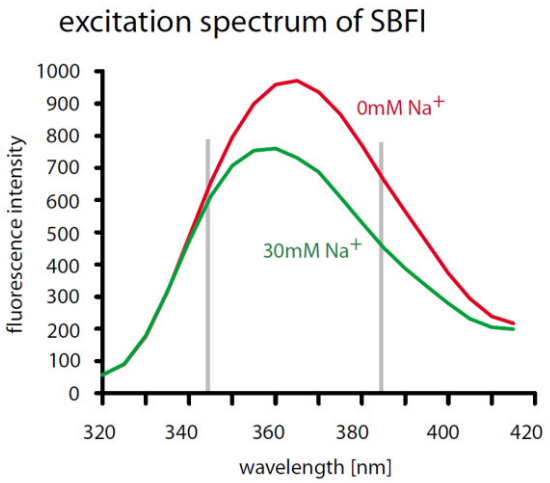

Abbildung 5: Die Emission von SBFI bei >440 nm für Anregungswellenlängen zwischen 320 und 420 nm. Die Graphen zeigen Messungen bei Natriumkonzentrationen von 0 und 30 mM. Bei ca. 340 nm ist der isosbestische Punkt zu erkennen, an dem die Emission näherungsweise invariant gegenüber Änderungen im Na^+ ist. Die grauen Markierungen zeigen die beiden typischen Anregungswellenlängen bei ratiometrischem Imaging.

Abbildung zur Verfügung gestellt von J. Langer, Institut für Neurobiologie, Heinrich-Heine-Universität Düsseldorf.

4.4 Stimulationsmethoden

Um die basalen biophysikalischen Eigenschaften von Natrium in einem intrazellulären Milieu und unter möglichst physiologischen Bedingungen zu untersuchen, muss zunächst ein transienter Einstrom von Na^+ induziert werden. Dessen Verlauf kann daraufhin mit den in Kapitel 4.1 bis 4.3 beschriebenen Methoden aufgezeichnet und ausgewertet werden.

4.4.1 Uncaging

Die Applikation von Botenstoffen, zum Beispiel Glutamat, stellt eine der physiologischen Funktion nahe kommende Form der Stimulation einer Nervenzelle dar. Ligandengesteuerte Öffnung ionotroper Rezeptoren führt, wie bei synaptischer Aktivität, unter anderem zu einem Einstrom von Natrium in die Zelle. Am einfachsten lässt sich dies durch kurze, lokale Druckapplikation dieser Botenstoffe mittels Mikropipetten erreichen. Dadurch ergeben sich Nachteile; so kann es potentiell zu Bewegungsartefakten kommen, die bei Imaging mit hoher Auflösung hinderlich sein kann.

Diese Problematik kann durch den Einsatz von Photolyse- oder Uncagingtechniken umgangen werden (Ellis-Davies, 2007; Kleinhans et al., 2014). Hierbei wird über das Probenbad oder eine lokale Druckapplikation ein Neurotransmitter in die zu stimulierende Region gebracht, der durch eine photolabile Bindung an einen chemischen „Cage“ biologisch zunächst inert ist (Ellis-Davies, 2007).

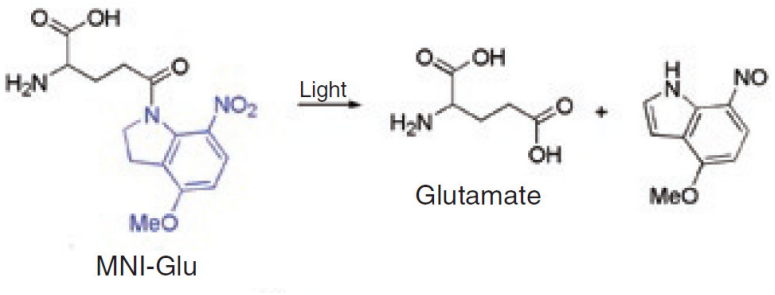

Abbildung 6: Chemische Strukturformel von MNI-Glutamat. In der linken Form ist die Verbindung biologisch inert und bindet nicht an postsynaptische glutamaterge Rezeptoren. Bei der Absorption eines Lichtquants wird der Neurotransmitter, wie rechts zu sehen, freigesetzt und wird biologisch aktiv. Aus (Ellis-Davies, 2007).

Bei Absorption von Licht einer bestimmten Wellenlänge, in der Regel im UV-Bereich, wird der Transmitter durch Photolyse freigesetzt und, wie in Abbildung 6 dargestellt, biologisch aktiv (Ellis-Davies, 2007; Trigo et al., 2009; Palma-Cerda et al., 2012). Das sogenannte *Uncaging* kann mit verschiedenen Lichtquellen durchgeführt werden, darunter Blitzlampen, LED-Lichtquellen oder Lasern. Letztere bieten im Vergleich die höchste räumliche Spezifität, was insbesondere dann von Vorteil ist, wenn der entsprechende Stoff nur sehr lokal freigesetzt werden soll (Korkotian et al., 2004b).

Es konnte gezeigt werden, dass die Photolyse von MNI-(4-Methoxy-7-Nitroindolinyl-) Glutamat an Dendriten von CA1-Pyramidenzellen zu reproduzierbaren, lokalen Natriumeinströmen führt (Kleinhans et al., 2014). Dabei kam ein konfokales Laserscanning-System zum Einsatz, dass die computergesteuerte Ausrichtung des Laserstrahls eines 355 nm-Festkörperlasers in der Fokusebene des Imagingmikroskops erlaubte. Der geringe Durchmesser des Strahls von ca. 2 µm erlaubte gezielte Stimulation einzelner zellulärer Strukturen (Kleinhans et al., 2014). Im Rahmen dieser Arbeit wurde der Messaufbau dahingehend verbessert, dass der Uncaginglaser anhand des Bildes aus der Imagingmessung, also mit höchst möglicher Präzision, auf die gewünschte Stelle auf der Probe ausgerichtet werden konnte. Zuvor war vorgesehen, die Ausrichtung anhand des mit einer Kamera aufgezeichneten Durchlichtbildes des Mikroskops vorzunehmen. Es

waren somit hard- und softwareseitig Modifikationen vonnöten. Eine Datenverbindung zwischen Imaging- und Uncaging-Steuereinheit erlaubte, zusammen mit anderen Änderungen, ein Einspeisen des Imaging-Bildsignals in die Uncagingsoftware in Echtzeit. Nach einer Kalibrierung konnte also das Fluoreszenzbild einer mit Farbstoff gefüllten Zelle zur Steuerung des Photolyselasers genutzt werden (beschrieben in (Kleinhans et al., 2014)).

Prinzipbedingt ergeben sich einige mögliche Nachteile des konfokalen Uncagings. Wird das Cage-Molekül über das Bad appliziert und ist dementsprechend entlang des Lichtweges des UV-Lasers überall vorhanden, wird dieser aufgrund der hohen Absorption bis zur Probe abgeschwächt. Dabei wird ebenfalls der gebundene Stoff freigesetzt (Trigo et al., 2009). Dies lässt sich durch lokale Druckapplikation des Cage-Moleküls an der gewünschten Stelle umgehen. Es bleibt jedoch bei der durch die kurze Wellenlänge des Uncaging-Lasers eingeschränkten Gewebeeindringtiefe (siehe Kapitel 4.1). Diese Limitationen entstehen bei Zwei-Photonen-Uncaging nicht, für das jedoch wesentlich teurere Geräte benötigt werden. Der Photolyseprozess findet nur in einem kleinen Volumen höchster Intensität im Brennpunkt statt, womit auch eine höhere räumliche Spezifizität einhergeht (Palma-Cerda et al., 2012; Kleinhans et al., 2014). Durch den um mehrere Größenordnungen geringeren Wirkungsquerschnitt der Cage-Moleküle für Nahinfrarotstrahlung sind für Zwei-Photonen-Uncaging allerdings sehr hohe Lichtintensitäten nötig, die potentiell phototoxisch sein können (Palma-Cerda et al., 2012).

4.4.2 Elektrische Stimulationsmethoden

Eine weitere Methode, um möglichst lokal einen Einstrom von Natrium zu kreieren, stellt die direkte elektrische Stimulation oder Elektroporation dar. Dabei macht man sich zunutze, dass die Zellmembran bei Anlegen eines elektrischen Feldes geeigneter Stärke Nanoporen bildet, die auch unselektiv durchlässig für geladene Teilchen sind (Neumann et al., 1998; Wang et al., 2010). Dieser Effekt ist nur von sehr kurzer Dauer. So schließen sich die Poren innerhalb weniger Millisekunden (Ryttsen et al., 2000). Die Wirkung des elektrischen Feldes hat eine sehr kurze Reichweite. Diese beträgt bei den typischerweise verwendeten Stimulationsspannungen (~15 V für <10 ms) weniger als 3 µm in jede Richtung (Nevian and Helmchen, 2007), womit die Stimulation sehr lokal und sehr kurz

wirkt und auch auf sehr kleine Zellkompartimente angewendet werden kann. Aufgrund des Natriumgradienten über der Zellmembran kommt es während des Bestehens der Poren zu einem starken Einstrom von Natrium und zur Depolarisation der Zelle (Nevian and Helmchen, 2007). Eine für die räumlich sehr begrenzte Erzeugung von Poren bewährte Form der Elektroporation ist die Nutzung einer Mikropipette als Stimulationselektrode (Nevian and Helmchen, 2007). Diese wird, zusammen mit einer Badelektrode als Erde, an einen Stimulator angeschlossen und die Spannung zum Aufbau des elektrischen Feldes angelegt (Olofsson et al., 2003; Wang et al., 2010). In der sehr großen Mehrheit aller Fälle kann die Elektroporation mehrmals wiederholt werden, ohne dass es zu Einschränkungen der Vitalität der Zelle kommt (Nevian and Helmchen, 2007). Die erzeugten Natriumtransienten waren in ihren grundlegenden Parametern wie Zeitkonstante, Amplitude und Signalanstieg denjenigen sehr ähnlich, die über Applikation von Glutamat ausgelöst wurden (siehe Kapitel 6.1 und 8.1). Dies wurde an anderer Stelle bereits für Calciumtransienten gezeigt (Nevian and Helmchen, 2007). Somit stellt die Elektroporation eine alternative Stimulationsmethode dar, mithilfe derer schnelle, räumlich und zeitlich stark begrenzte Natriumeinströme induziert werden können.

4.5 Präparat

Für diese Studie wurden als Präparat Akutschnitte des Hippocampus der Maus verwendet (Meier et al., 2006; Kleinhans et al., 2014). Der Hippocampus befindet sich bilateral symmetrisch in beiden Hemisphären des Gehirns. Er stellt eine Struktur dar, die für die Gedächtniskonsolidierung von zentraler Bedeutung ist (McKenzie and Eichenbaum, 2011). Seine Anatomie und Funktion ist sehr gut beschrieben, wodurch er ein vielgenutztes experimentelles System darstellt (Strange et al., 2014).

Der Hippocampus hat eine gebogene, schlauchähnliche Form und besteht aus den Regionen der *Cornu Ammonis* (CA) und *Gyrus Dentatus*. Die *Cornu Ammonis* ist entlang ihrer Längsachse eingeteilt in die Regionen CA1-4. Quer dazu teilt sie sich in mehrere Schichten auf. Im *Stratum Pyramidale* befindet sich die Mehrzahl der Pyramidenzellen, Neurone, die im *Stratum Oriens* Basaldendriten und im *Stratum Radiatum* sowie im *Stratum Lacunosum Moleculare* Apikaldendriten bilden.

Innerhalb der hippocampalen Formation projizieren die Körnerzellen des *Gyrus Dentatus* über die Moosfasern auf die Dendriten der Pyramidenzellen der CA3-Region. Diese

wiederum bilden über ihre Axone, die Schaffer-Kollaterale, glutamaterge synaptische Verbindungen mit den Spines der apikalen Dendriten der CA1-Pyramidenzellen. Diese Spines sollen im Folgenden näher beschrieben werden.

5 Dendritische Spines zentraler Neurone

Dendritische Spines sind Ausstülpungen der neuronalen Zellmembran. Sie bestehen aus einem Spine Head und einem dünnen Spine Neck, durch den sie das Neuron, in der überwiegenden Mehrzahl an einem Dendriten, kontaktieren (siehe Abbildung 7, (Bourne and Harris, 2008)). Umschlossen von den Ausläufern von Astrocyten bilden Spines zusammen mit den Endigungen der Axone anderer Neurone die *Tripartite Synapse* (Araque et al., 1999). Spines finden sich in verschiedenen neuronalen Populationen aller Vertebraten sowie einiger Invertebraten und beherbergen die postsynaptische Struktur von mehr als 90% aller erregenden Synapsen; somit befinden sich im menschlichen Gehirn mehr als 10^{13} Spines (Nimchinsky et al., 2002). Als Voraussetzung der synaptischen Funktion und Plastizität enthalten sie, insbesondere im Bereich der postsynaptischen Dichte (PSD), Rezeptoren für Neurotransmitter, Ionenkanäle und weitere Komponenten zur Signalübertragung sowie diverse Organellen. Darüber hinaus können Spines einzelne biochemische Kompartimente für verschiedene Neurotransmitter und Ionen bilden (Bourne and Harris, 2008) und sind deswegen die kleinste Einheit der Signalintegration im Gehirn (Denk et al., 1995; Yuste and Denk, 1995).

Spines und somit die synaptischen Verknüpfungspunkte einzelner Neurone unterliegen ständigen Änderungen. Ausgelöst durch sensorische Reize werden sie fortwährend neu gebildet, in ihrer Geometrie angepasst oder vollständig eliminiert. Folgerichtig sind sie von entscheidender Wichtigkeit für Lernprozesse und Gedächtnisbildung (Yuste and Bonhoeffer, 2001; Holtmaat and Svoboda, 2009). Aufgrund ihrer fundamentalen Bedeutung für die Funktion des Gehirns sind Spines seit ihrer Entdeckung durch

Abbildung 7: Hochauflösende 3D-STED Aufnahme eines Dendriten mit Spines aus einer hippocampalen organotypischen Schnittkultur. Die Aufnahme besteht aus einem z-Stapel mit 8 optischen Schnitten in jeweils 0.5 µm Abstand. Maßstabsbalken: 1 µm (Nagerl et al., 2008).

Rámon y Cajal Ende des 19. Jahrhunderts (Garcia-Lopez et al., 2007) Gegenstand der neurowissenschaftlichen Forschung.

5.1 Morphologie

Hippocampale dendritische Spines, die in dieser Arbeit im Fokus stehen, divergieren in ihrer Morphologie. Mit hochauflösenden bildgebenden Verfahren, vor allem Elektronenmikroskopie und nicht-beugungsbegrenzter Laser-Scanning-Mikroskopie (STED), wurden umfassende Daten bezüglich ihrer Größe erhoben.

Spines haben ein Volumen von ~0,001 – 1 µm³ (Nimchinsky et al., 2002). Der Spine Head weist hierbei einen Durchmesser von etwa 200 – 1500 nm auf. Er ist über einen Neck mit dem Dendriten verbunden, der im Durchmesser 60-250 nm, in der Länge jedoch 80-2300 nm misst (Nagerl et al., 2008; Tønnesen et al., 2014; Wijetunge et al., 2014).

Man unterteilt Spines grob in drei Kategorien, die in Abbildung 8 verdeutlicht sind: Dünne, filopodienähnliche Strukturen („Thin Spines“), kurze Spines ohne erkennbaren Neck

(„Stubby Spines“) und solche mit einem großen, ausgeprägten Spine Head („Mushroom Spines“) (Bourne and Harris, 2008).

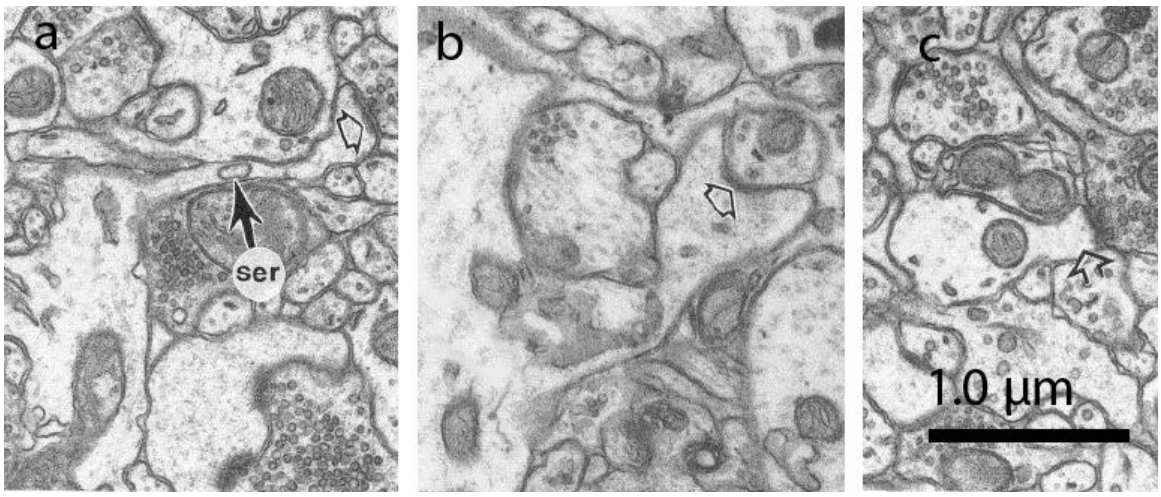

Abbildung 8: Elektronenmikroskopische Aufnahmen von Spines in der CA1-Region des Hippocampus. (a)Thin Spine, (b) Mushroom Spine, (c) Stubby Spine. Unbeschriftete Pfeile zeigen den Bereich der PSD. ser: Glattes endoplasmatisches Retikulum (Harris et al., 1992).

In der Zellmembran des Spine Heads befindet sich die Postsynaptische Dichte (PSD) mit einer durchschnittlichen Fläche von 0.08 µm² (Arellano et al., 2007), in der direkt am synaptischen Spalt eine Vielzahl an Rezeptoren und Ionenkanälen konzentriert sind (Nimchinsky et al., 2002). Darunter fallen beispielsweise NMDA- und AMPA-Rezeptoren sowie weitere, für die synaptische Funktion essentielle Proteine. Des Weiteren finden sich innerhalb des Spine-Komplexes Actin-Mikrofilamente, in den meisten Fällen glattes endoplasmatisches Retikulum (sER) sowie der Spine Apparat, der vor allen Dingen für die Funktion der Langzeit-Potenzierung (LTP) von Bedeutung ist (Segal et al., 2010). Durch das Vorhandensein dieser Strukturen ist das effektive Volumen des Spines, insbesondere im Bereich des Spine Necks, weiter verringert.

5.2 Kompartimentierung

Ob und wie die starke morphologische Diversität sich auf die Funktion der Spines als postsynaptische Struktur auswirkt, wurde lange kontrovers diskutiert (Araya et al., 2006a; Araya et al., 2006b; Araya et al., 2007; Grunditz et al., 2008; Bloodgood et al., 2009; Harnett et al., 2012; Araya et al., 2014; Takasaki and Sabatini, 2014; Bywalez et al., 2015).

Durch die teils starke strukturelle Trennung der Spines von ihrem Dendriten bildet der Spine Neck eine mehr oder minder große Diffusionsbarriere. Moleküle, die zwischen diesen Kompartimenten über den Neck ausgetauscht werden, müssen also eine sehr

begrenzte Passage niedrigen Volumens durchqueren. Hinzu kommt, dass sich entlang des Spine Necks Pumpen und Transporter wie die Natrium-Kalium-ATPase (NKA) und der Natrium-Calcium-Austauscher (NCX) befinden, die den Ionenfluss weiter einschränken (Lorincz et al., 2007; Blom et al., 2011).

Durch die beschriebenen Einschränkungen bei der Diffusion entlang eines langen, schmalen Spine Necks kommt es zu einer partiellen biochemischen Entkopplung vom Dendrit. Kommt es zum Beispiel während synaptischer Aktivität zu einem wiederholten Einstrom von Calcium, treten in der Folge einer starken Kompartimentierung Akkumulationseffekte auf, die zu einer höheren Amplitude und einem langsameren Rückgang der Konzentration führen. Dies konnte insbesondere für Calcium als einen sekundären Botenstoff übergeordneter Wichtigkeit für viele zelluläre Prozesse in

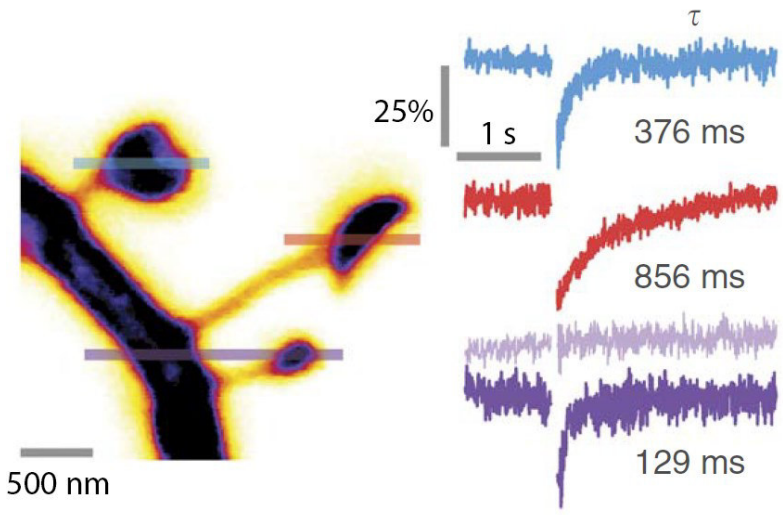

Abbildung 9: Spines stellen heterogene biochemische Kompartimente dar. Das Ausmaß der funktionalen Trennung vom Dendriten variiert stark mit der Morphologie. Die FRAP-Messspuren auf der rechten Seite zeigen die Fluoreszenz entlang der jeweils farblich korrelierenden Linie auf der linken Seite während eines Line Scans. Der hellviolette Graph repräsentiert die Fluoreszenz im Dendriten. Die Zeitkonstante τ der jeweiligen monoexponentiellen Fits des Fluoreszenzanstieges nach einem Bleichpuls dient als Maß der diffusiven Entkopplung. Als Farbstoff wurde YFP (Yellow Fluorescent Protein) verwendet. Modifiziert aus (Tønnesen et al., 2014).

mehreren experimentellen und numerischen Studien gezeigt werden (siehe auch Kapitel 6.2). Im Rahmen dieser Arbeit werden zudem erstmalig Hinweise auf eine Kompartimentierung in Bezug auf Natrium präsentiert, auf deren Folgen in Kapitel 6.3 eingegangen wird.

Somit bildet der Spine in Bezug auf verschiedene Moleküle eine eigene funktionale Einheit. Dies lässt sich anschaulich in FRAP-Experimenten (*Fluorescence Recovery After Photobleaching*) zeigen. Dabei dient die von den morphologischen Gegebenheiten abhängige Zeitkonstante, die nach starkem lokalen Bleichen eines Farbstoffes im Spine nötig ist, um die Farbstoffkonzentration durch Diffusion wieder anzugleichen, als Maß für die biochemische Trennung der Strukturen (siehe Abbildung 9, (Tønnesen et al., 2014)).

Dabei ist die Zeitkonstante τ durch die Formel

$$\tau = \frac{VL}{DA}$$

beschrieben (Alvarez and Sabatini, 2007). Hierbei ist V das Volumen des Spine Heads, L bzw. A die Länge und der Querschnitt des Spine Necks und D der Diffusionskoeffizient des Ions im Neck. Es wird deutlich, dass die Geometrie des Necks eine wichtige Rolle spielt. Dabei kommt es, wie sich in komplexen Simulationsstudien herausgestellt hat, neben der Länge (der vorrangige Bedeutung zugeschrieben wird) und des Querschnitts des Spine Necks auch auf die geometrische Form der Verbindung zum Spine Head an (Biess et al., 2007; Holcman and Schuss, 2011).

Natrium ist der Hauptladungsträger bei synaptischem Einstrom und verantwortlich für die Depolarisation der Zellmembran. Somit sind die biochemischen Eigenschaften Natrium betreffend eng verknüpft mit den elektrischen Eigenschaften eines Spines: Eine mögliche Beeinträchtigung des Überganges von Ionen zwischen Dendrit und Spine hätte gleichsam Auswirkungen auf den elektrischen Widerstand des Spine Necks. In der Tat ist die Frage nach der Existenz einer elektrischen Kompartimentierung bereits seit langer Zeit Gegenstand wissenschaftlichen Diskurses (Koch and Zador, 1993; Svoboda et al., 1996; Tsay and Yuste, 2004; Harnett et al., 2012; Yuste, 2013; Adrian et al., 2014). Dabei gibt es mehr und mehr Hinweise, dass Spines, abhängig von ihrer Geometrie, einen entscheidenden Einfluss auf die Signalintegration in Dendriten nehmen. Die äußert sich unter anderem in der Verstärkung oder Filterung von erregenden postsynaptischen Potentialen (EPSPs) (Araya et al., 2006a; Araya et al., 2006b; Araya et al., 2007; Harnett et al., 2012).

Zum Verständnis der elektrischen Eigenschaften eines Spines ist der Ohm'sche Widerstand R_{neck} seines Spine Necks ein kritischer Parameter. In Ermangelung der

Möglichkeit, diesen direkt zu messen, gibt es zwei verschiedene Approximationsmöglichkeiten. R_{neck} kann auf der Grundlage von Diffusionsmessungen (z.B. FRAP, siehe Abbildung 9) oder morphologischer Parameter abgeschätzt werden (Tønnesen et al., 2014):

$$R_{neck}^{\tau} = \frac{\tau \rho D}{V}$$

$$R_{neck}^{morph} = \frac{\rho L}{A}$$

Hier symbolisiert ρ den spezifischen Widerstand des Cytosols, D den Diffusionskoeffizienten, L die Länge und A den Querschnitt des Spine Necks, V das Volumen des Spine Heads sowie τ die Zeitkonstante (siehe oben). Die in der Literatur angegeben Werte für R_{neck} variieren, liegen aber für längere Spines im Bereich von 500 MΩ (Harnett et al., 2012) bis 1 GΩ (Araya et al., 2014). Aus dieser Tatsache ergibt sich ein wesentlich höherer Eingangswiderstand für den Spine im Vergleich zum Dendrit (Koch and Zador, 1993). Daher können Spannungsänderungen sich ohne große Abschwächung in Spines ausbreiten (wie etwa bei rückpropagierenden Aktionspotentialen), während synaptische Potentiale kaum in den Dendriten vordringen (Adrian et al., 2014). Als weitere Konsequenz entsteht bei gleichem Einstrom eine 1.5-45-fach höhere Depolarisation im Spine Head und damit eine signifikante Erhöhung der EPSPs (Harnett et al., 2012; Yuste, 2013).

Die Amplitude der EPSPs in Spine und Dendrit kann beschrieben werden durch

$$V_{spine} = \frac{E_{syn} g_{syn} (R_{dend.} + R_{neck})}{1 + g_{syn} (R_{dend.} + R_{neck})}$$

und

$$V_{dend.} = \frac{E_{syn} g_{syn} R_{dend.}}{1 + g_{syn} (R_{dend.} + R_{neck})}.$$

Daraus folgt für das Verhältnis der EPSP-Amplituden

$$\frac{V_{spine}}{V_{dend.}} = 1 + \frac{R_{neck}}{R_{dend.}},$$

wobei der Einfluss von R_{neck} auf den Potentialunterschied zwischen Spine und Dendrit deutlich wird (siehe Abbildung 10).

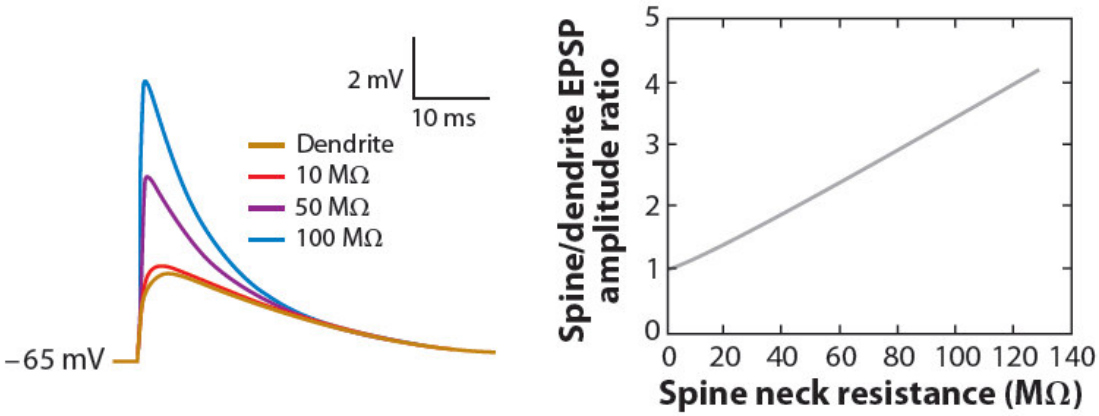

Abbildung 10: Numerische Simulation eines elektrisch passiven Spines. Links: Überhöhung der EPSPs im Spine Head im Vergleich zum Potential im Dendriten in Abhängigkeit vom elektrischen Widerstand des Spine Necks gezeigt. Rechts: Das Verhältnis der EPSP-Amplituden in Spine und Dendrit ist proportional zum Spine Neck-Widerstand. Aus (Yuste, 2013).

Auf die Konsequenzen einer Kompartimentierung auf die synaptische Funktion wird in Kapitel 6.3 näher eingegangen.

6 Wissenschaftlicher Kontext

6.1 Natriumsignale und -diffusion in zellulären Strukturen

Natriumsignale in Neuronen und Astrocyten wurden in der Literatur bereits beschrieben. Dabei wurde auf Fluoreszenzimaging zurückgegriffen und auf verschiedene Weise transiente Natriumerhöhungen ausgelöst. So konnte gezeigt werden, dass bei Induktion epileptiformer Netzwerkaktivität sowohl in hippocampalen Neuronen als auch in Astrocyten synchrone somatische Natriumsignale auftreten, die mit der Depolarisation des Ensembles korreliert sind ((Karus et al., 2015b), siehe Abbildung 11).

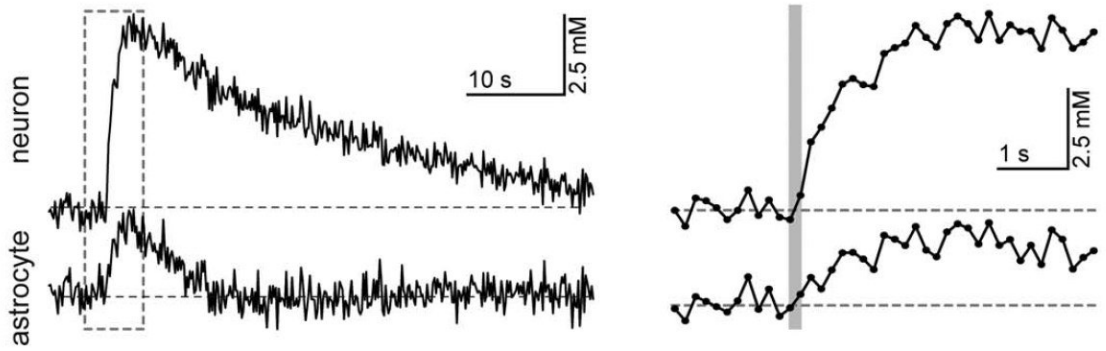

Abbildung 11: Somatische Natriumsignale in Neuronen und Astrocyten der CA1-Region des Hippocampus bei epileptiformer Aktivität. Die gestrichelte Box auf der linken Seite ist rechts vergrößert dargestellt. Der graue Bereich auf der rechten Seite zeigt den Beginn des Signals; beide Signalanstiege koinzidieren bei der genutzten Bildwiederholrate (6 Hz). Aus (Karus et al., 2015b).

Darüber hinaus wurden bei direkter elektrischer Stimulation von Astrocyten intra- und interzelluläre Natriumsignale beobachtet, die sich per Diffusion über Gap Junctions in benachbarte Astrocyten ausbreiten. Auch in subzellulären Strukturen, insbesondere in Dendriten und Spines von CA1 Pyramidenzellen des Hippocampus, wurden synaptisch induzierte oder durch Glutamat-Uncaging erzeugte Natriumsignale beobachtet (Rose and Konnerth, 2001; Kleinhans et al., 2014). Weiterhin wurden während der Auslösung von

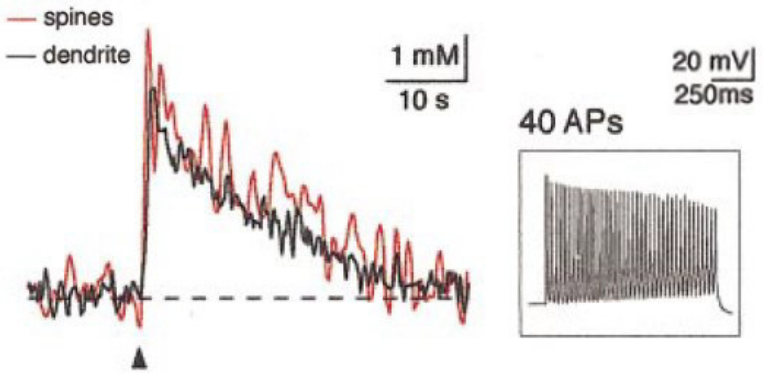

Abbildung 12: Natriumtransienten (links) in Spines (rot) und Dendriten (schwarz) während rückpropagierender Aktionspotentiale (rechts, (Rose et al., 1999)).

rückpropagierenden Aktionspotentialen in Spines größere Natriumerhöhungen gemessen als in den angrenzenden Dendriten ((Rose et al., 1999), siehe Abbildung 12).

Zur Beschreibung der Ausbreitung von Molekülen in zellulären Strukturen ist die Kenntnis des Diffusionskoeffizienten für den betreffenden Stoff in der jeweiligen Umgebung von großer Bedeutung. Beispielsweise stellt er mathematisch in den Fick'schen Diffusionsgesetzen die Proportionalitätskonstante zwischen dem Konzentrationsgradienten, der die Ursache der Diffusion ist, und dem resultierenden Teilchenfluss dar (Noguchi et al., 2005). Dieser Diffusionskoeffizient wurde in der Literatur für Natrium bis dato in wässriger Lösung (~1500 µm²/s, (Lobo, 1993)) und im Cytosol von Muskelzellen (600 µm²/s, (Kushmerick and Podolsky, 1969)), Oocyten (790 µm²/s, (Allbritton et al., 1992)) und Eidechsenaxonen (1300 µm²/s, (David et al., 1997)) bestimmt. Zum Vergleich beträgt er für Calcium etwa 220 µm²/s (Allbritton et al., 1992). Bei der Einordnung dieser Werte muss berücksichtigt werden, dass Diffusion in neuronalen Fortsätzen nicht ungehindert stattfindet. Vielmehr stellen sie verzweigte Strukturen dar, die zusätzlich sowohl Cytoskelett als auch Organellen beinhalten. Spines sind außerdem mit dem Spineapparat ausgestattet (Spacek and Harris, 1997; Segal et al., 2010), der neben ihren sehr kleinen Volumina im Femtoliterbereich als zusätzliches Diffusionshindernis in Frage kommt (siehe auch Kapitel 5.1). Als Konsequenz dieser Gegebenheiten kann sich der effektive Diffusionskoeffizient um etwa eine Größenordnung verringern (Soler-Llavina and Sabatini, 2006; Biess et al., 2011). Der diffusive Austausch von Molekülen zwischen Dendriten und Spines ist über den Diffusionskoeffizienten hinaus abhängig von der Geometrie des sie verbindenden Elementes, des Spine Necks (Biess et al., 2007).

6.2 Biochemische und elektrische Kompartimentierung

Der Austausch von Molekülen zwischen zellulären Strukturen wie Spines und Dendriten ist, wie in Kapitel 5.2 beschrieben, zu einem Teil abhängig von ihrer Geometrie. Diese direkte Wechselwirkung zwischen Morphologie und Funktion wurde für Second-Messenger-Moleküle wie Calcium bereits beschrieben (Yuste and Denk, 1995; Sabatini et al., 2002; Schmidt and Eilers, 2009), wobei besonders die Rolle des Spine Necks als diffusiv entkoppelndes Element aufgezeigt wird. Als Folge dessen agieren vor allem Spines, die über einen langen Neck mit dem Dendrit verbunden sind, als eigenständiges biochemisches Kompartiment und somit kleinste signalintegrierende Einheit in Neuronen. Es ist jedoch naheliegend, dass auch dieser Querschnitt einen Einfluss auf die Spine-Dendrit-Kopplung hat. Sowohl Simulationsstudien (Schmidt and Eilers, 2009) als auch experimentelle Hinweise aus FRAP-Messungen (*Fluorescence Recovery After Photobleaching*) unterstützen diese Annahme (Tønnesen et al., 2014).

Für Natrium konnte eine solche Kompartimentierung bis jetzt noch nicht gezeigt werden. Während der Öffnung ionotroper Glutamatrezeptoren bei erregender neuronaler Aktivität ist Natrium der Hauptladungsträger bei der Depolarisation der Zellmembran. Folglich stellt Natriumeinstrom in die Postsynapse einen grundlegenden Mechanismus bei der Ausbildung von erregenden postsynaptischen Potentialen (EPSPs) dar. Unterscheiden sich die Amplituden der EPSPs zwischen zwei verbundenen Strukturen stark und können infolgedessen als unabhängig fungierende Einheiten der Signalverarbeitung angesehen werden, spricht man von elektrischer Kompartimentierung, auf deren Existenz es viele Hinweise gibt (für eine tiefergehende Beschreibung siehe Kapitel 5.2 und (Yuste, 2013)).

6.3 Funktionale Folgen einer Kompartimentierung

Eine biochemische Kompartimentierung geht, wie obenstehend beschrieben, einher mit einer starken Beeinflussung der elektrischen Eigenschaften einer Synapse. Die vermutete Eigenschaft des Spine Necks, die Natriumdiffusion einzuschränken, hätte direkte Auswirkungen auf den elektrischen Widerstand desselben. Eine dadurch mögliche elektrische Kompartimentierung durch lange bzw. dünne Spine Necks hätte einige folgenschwere Implikationen. Beispielsweise würde sie zu einer substantiellen Erhöhung der EPSPs in der Postsynapse und somit im Spinehead führen (Tsay and Yuste, 2004;

Grunditz et al., 2008; Harnett et al., 2012; Yuste, 2013). In diesem Zusammenhang konnte bereits eine inverse Korrelation der EPSPs mit der Spine Neck-Länge beobachtet werden ((Araya et al., 2014), sieheAbbildung 13).

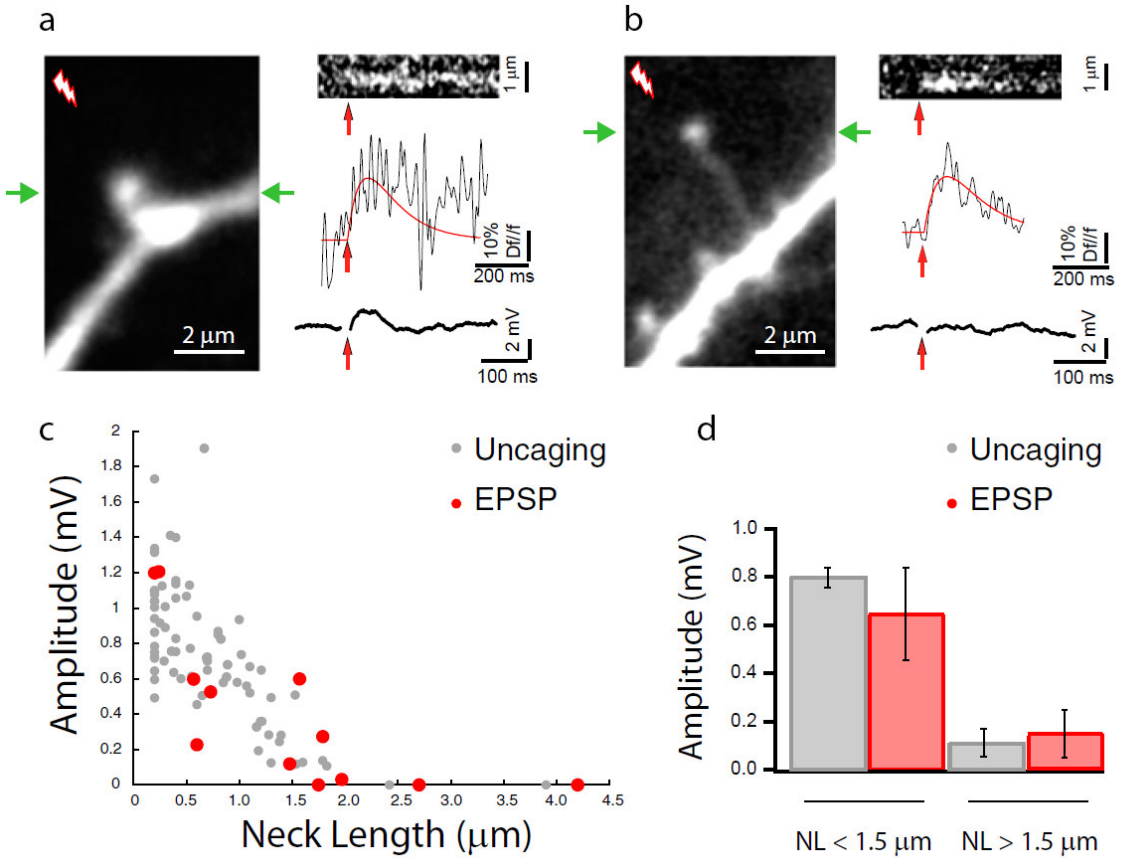

Abbildung 13: Inverse Korrelation zwischen EPSP-Amplitude und Spine Neck Länge. (a) Minimale synaptische Stimulation eines kurzen Spines erzeugt ein Calciumsignal im Spine Head und ein Spannungssignal im Soma. (b) Dieselbe Stimulation führt in einem langen Spine zu einem Calciumsignal, jedoch nicht zu einer Spannungsänderung im Soma. Die grünen Pfeile in a und b zeigen an, wo die Linie während des Line Scans verlief. (c) Amplitude der somatischen Spannungsänderungen, erzeugt durch minimale synaptische Stimulation eines Spines (rote Punkte) bzw. durch Zwei-Photonen Glutamat-Uncaging (graue Punkte) in Abhängigkeit der Spine Neck Länge. (d) Spannungssignale in c, aufgeteilt in Spines mit langen (<1.5 µm) und kurzen (>1.5 µm) Necks. Die Amplituden sind bei langen Spine Necks signifikant (P<0.01) reduziert zu denjenigen in kurzen Spines (Araya et al., 2014).

Da einige ionotrope Kanäle der Postsynapse im Gegensatz zu AMPA-Rezeptoren (AMPAR) keinen linear mit der Spannung steigenden Einstrom liefern, sondern im Falle von NMDA-Rezeptoren (NMDAR) und spannungsabhängigen Calciumkanälen (*high voltage activated calcium channels*, HVACC) erst bei ausreichender Depolarisation der Zellmembran geöffnet werden, würde ein EPSP umso mehr verstärkt werden. Dieser Effekt wird, wie in Abbildung 14 dargestellt, durch spannungsabhängige Natriumkanäle (Na_V) im Spine

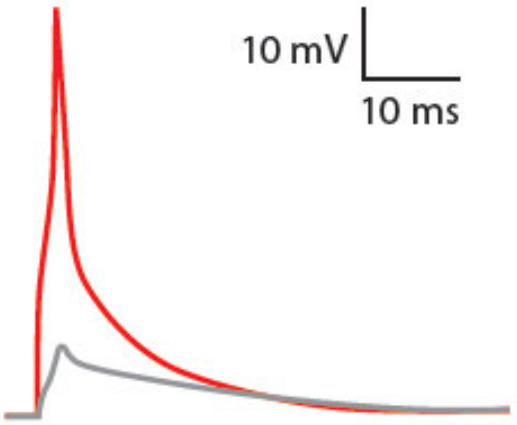

Abbildung 14: Numerische Simulation eines EPSPs in einem aktiven Spine mit Na_V (rot) und im Dendriten (grau). Voraussetzung für ein solches „lokales Aktionspotential" ist schwache elektrische Kompartimentierung durch einen Spine Neck Widerstand >100 MΩ (Yuste, 2013).

unterstützt, für deren Existenz es bereits in neocorticalen Neuronen (Araya et al., 2007) und Körnerzellen des *bulbus olfactorius* (Bywalez et al., 2015) Evidenz gibt. Die Erhöhung der Depolarisation kann folglich bis zum synaptischen Umkehrpotential und der damit einher gehenden Sättigung der Synapse fortschreiten. Eine der Hauptfolgen wäre, wie in Abbildung 15 skizziert, eine deutliche Erhöhung des Calciumeinstroms durch die verstärkte Depolarisation der Synapse. Dadurch kann es mit größerer Wahrscheinlichkeit zu nachgeschalteten Mechanismen wie Langzeitpotenzierung oder –depression, die Calciumvermittelt sind, kommen (Malenka, 1994; Matsuzaki et al., 2004; Xin et al., 2005; Kim and Linden, 2007). Spines sind dementsprechend nicht statisch in ihrer Geometrie, sondern vielmehr plastischen Änderungen unterworfen, die durch synaptische Aktivität ausgelöst werden (Alvarez and Sabatini, 2007; Wiegert and Oertner, 2013; Araya et al., 2014; Bosch et al., 2014; Gu et al., 2014; Meyer et al., 2014; Sala and Segal, 2014; Bailey et al., 2015).

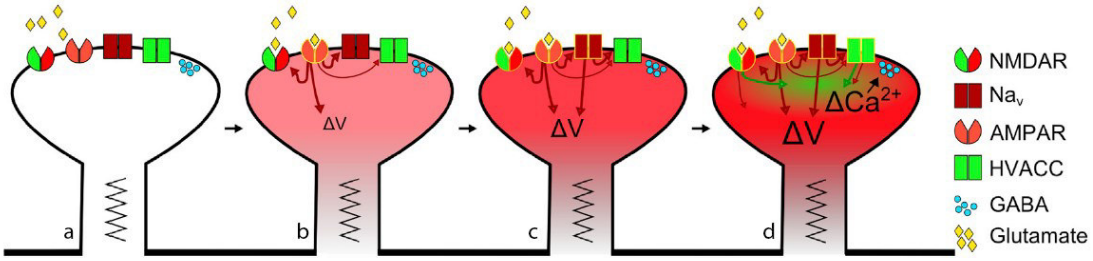

Abbildung 15: Schema der Aktivierungssequenz von Spines mit Na_V-Kanälen. (a) Spine mit für postsynaptische Signale wichtigen Leitfähigkeiten (siehe Legende rechts). (b) Glutamat aktiviert AMPARs und es kommt zur Depolarisation. (c) Einstrom durch AMPARs aktiviert Na_Vs, was eine weitere Verstärkung der Depolarisation zur Folge hat. (d) Durch diese hohe Umladung des Spines öffnen HVACCs, was zusätzlich zur Öffnung von NMDARs für eine substantielle Erhöhung des Calciumlevels sorgt. (modifiziert aus (Bywalez et al., 2015))

612

613 Diesbezüglich wurde im Rahmen einer Superresolution-Studie ((Tønnesen et al., 2014),
614 siehe Abbildung 16) gezeigt, dass bei wiederholter Stimulation von einzelnen Spines durch
615 sehr schwaches Glutamat-Uncaging in Mg^{2+}-freier Lösung deutliche, korrelierte
616 morphologische und elektrische Änderungen zu Tage traten, die über mindestens eine
617 Stunde aufrecht erhalten blieben. Im Gegensatz zu benachbarten Spines, die nicht von
618 der Stimulation betroffen waren, vergrößerte sich der Durchmesser der Necks der
619 stimulierten Spines um 30%, während die Länge derselben währenddessen um 25%
620 abnahm. Mit demselben Stimulationsprotokoll konnte die Effizienz und dadurch die
621 erregenden postsynaptischen Ströme (EPSCs) eines Spines um 75% erhöht werden.
622 Beinhaltete die Lösung während der Experimente Mg^{2+} und wurde ein Calciumeinstrom
623 durch NMDARs (unter der Voraussetzung geringer Depolarisation durch schwache
624 Stimulation) somit geblockt, konnten ebenfalls keine signifikanten Änderungen
625 beobachtet werden. Auch die Erhöhung der EPSCs blieb aus.

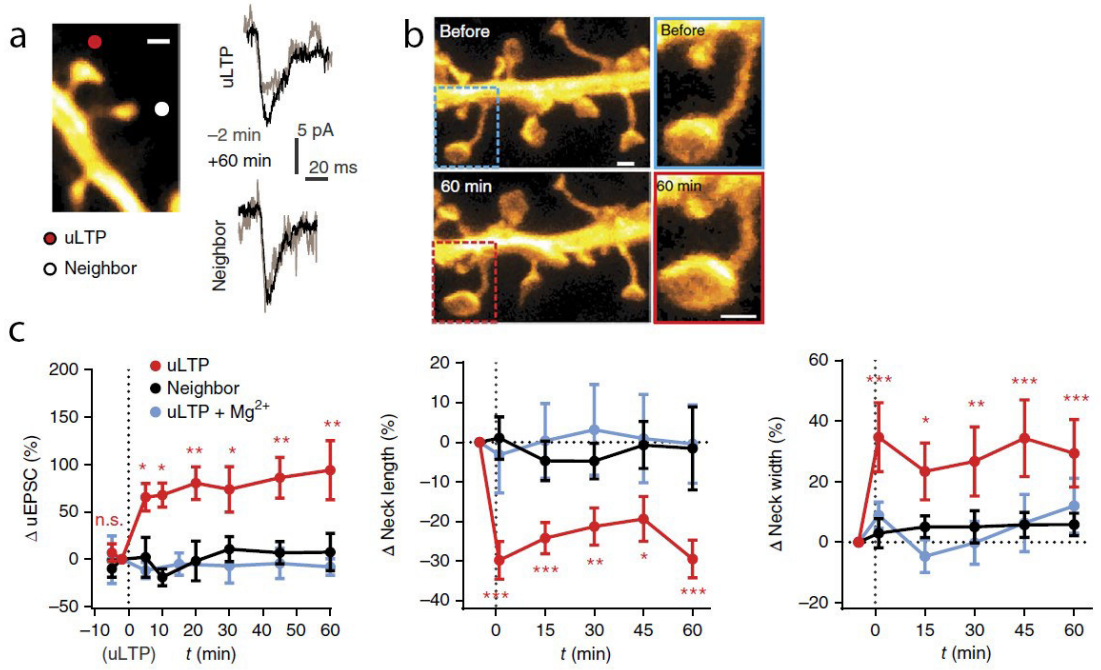

*Abbildung 16: Strukturelle Plastizität bei LTP. (a) Uncaging-EPSCs (uEPSCs) in einem stimulierten (roter Punkt) und einem benachbarten Spine (weißer Punkt) vor der Ausführung des Stimulationsprotokolls und 60 Minuten danach. (b) Beispiel eines potenzierten Spines vor und nach der Stimulation. Gestrichelte Boxen sind rechts daneben vergrößert dargestellt; Maßstabsbalken: 500 nm. (c) Effekt des LTP-Protokolls auf uEPSCs, Spine Neck-Länge und –Durchmesser von stimulierten Spines, benachbarten Spines und in Mg^{2+}-Lösung stimulierten Spines. Whisker zeigen den Standardfehler. Signifikanzniveaus: * P<0.05; ** P<0.01; *** P<0.001. Modifiziert aus (Tønnesen et al., 2014).*

Die dargestellte Wechselwirkung aus Funktion und morphologischer Beschaffenheit einer Synapse könnte folglich eine Art Regelschleife bilden, die dynamisch die biochemische und elektrische Kopplung mit dem Dendriten moduliert (Korkotian et al., 2004a; Sala and Segal, 2014). So könnte der Einfluss einer einzelnen Synapse auf die Signalintegration, ihre synaptische Effizienz, laufend angepasst werden (Magee, 2000; Tsay and Yuste, 2004; Arellano et al., 2007; Harnett et al., 2012).

7 Zusammenfassung und Einordnung der Resultate

Die in den vorangegangenen Kapiteln 3, 5 und 6 genannten Aspekte wurden in dieser Arbeit qualitativ und quantitativ behandelt. *In situ* wurde von Zwei-Photonen Fluoreszenzimaging Gebrauch gemacht, um mit dem Natriumindikatorfarbstoff SBFI Natriumsignale aufzuzeichnen. Durch das hohe räumliche und zeitliche Auflösungsvermögen dieser Methode war es möglich, die Signale auch in kleinsten Kompartimenten wie Spines zu untersuchen. Natriumsignale wurden entweder durch Photolyse von Glutamat als natürlicher Agonist oder durch direkte elektrische Stimulation bzw. synaptische Stimulation ausgelöst. Die Patch-Clamp-Technik lieferte elektrophysiologische Daten und erlaubte die selektive Füllung einzelner Zellen mit dem Farbstoff bis in feine Ausläufer hinein. Die genannten Techniken wurden so gekoppelt, dass ihre Messdaten zeitlich korreliert waren und somit in jeder Einzelmessung ein möglichst kohärentes Gesamtbild entstand. Ebenso konnte durch getriggerte Steuerung aller Komponenten ein standardisierter Ablauf ermöglicht werden, der die Vergleichbarkeit von einzelnen Messungen maximierte. Nach Abschluss der Experimente wurden, um die morphologischen Gegebenheiten möglichst akkurat wiederzugeben, hochauflösende Stapel optischer Schnitte der Zellkompartimente erstellt, die durch Deconvolution qualitativ weiter verbessert werden konnten.

7.1 Natriumsignale in Dendriten und Spines

Die vorliegende Arbeit bestätigt, dass die Aktivierung ionotroper Glutamatrezeptoren in hippocampalen CA1-Pyramidenzellen der Maus transiente, postsynaptische Natriumsignale in Spines und Dendriten nach sich zieht (Kleinhans et al., 2014). Photolytisch ausgelöste Signale zeigten eine durchschnittliche Amplitude von ca. 30 mM und einem monoexponentiellen Rückgang mit einer Zeitkonstante von etwa 4 s, die mit einem mittleren, am Soma gemessenen Ladungseinstrom von etwa 60 pC einhergingen. Diese Signale konnten sowohl in Dendriten als auch in Spines beobachtet werden und gingen konform mit in der Literatur vorgenommenen Charakterisierungen (siehe Kapitel 6.1).

Die genannten Ergebnisse konnten in guter Übereinstimmung mittels direkter elektrischer Stimulation reproduziert werden, wobei gezeigt werden konnte, dass diese noch lokaler und zeitlich begrenzter wirkt.

Mithilfe dieser Technik wurde der intrazelluläre, apparente Diffusionskoeffizient in solchen Mikrodomänen zu rund 160 µm²/s bestimmt. Dies ist im Vergleich zu den in wesentlich größeren zellulären Strukturen gemessenen Werten deutlich langsamer als bis dato angenommen (siehe Kapitel 6.1) und stellt einen Sachverhalt dar, der einige potentielle funktionale Konsequenzen für die neuronale Funktion nach sich ziehen könnte (siehe Kapitel 6.3).

7.2 Natriumkompartimentierung

In dieser Arbeit wurde erstmals eine Charakterisierung von Natriumsignalen in Spines und Dendriten in Abhängigkeit von der morphologischen Beschaffenheit dieser Strukturen vorgenommen. Insbesondere wurde der Einfluss der Länge des Spine Necks untersucht. Dabei zeigte sich, dass im Falle eines kurzen Spine Necks Natriumsignale in Spine und Dendrit hinsichtlich ihrer Amplituden und Zeitverläufe nicht unterschieden werden konnten. In Spines mit einem langen Neck hingegen traten Natriumtransienten im Vergleich gedämpft und verzögert auf, sofern sie im Dendriten induziert wurden. Synaptisch induzierte und somit initial im Spine selbst auftretende Natriumsignale zeigten hingegen einen schnelleren Anstieg, größere Amplitude und andere Abfallkinetik als diejenigen im angrenzenden Dendriten. Dieses komplementäre Verhalten, das bei Einstrom entweder über den Dendriten oder direkt in den Spine Head sozusagen von beiden Seiten bestätigt werden konnte, ist ein deutlicher Hinweis auf eine Natriumkompartimentierung in Spines.

Anders als bei Dendriten und kurzen Spines ließ sich bei synaptischer Stimulation in langen Spines ein biexponentieller Abfall des Natriumlevels konstatieren, der auf das Vorhandensein von spannungsabhängigen Natriumkanälen im Spine Head auch bei CA1-Pyramidenzellen hindeutet (siehe Kapitel 6.3).

Die Ergebnisse für diese unterschiedlichen Szenarien konnten in ihrer Gesamtheit mittels einer numerischen Simulation umfassend bestätigt werden. Die durch den Spine Neck erzeugte Verzögerung und Abschwächung der von uns gemessenen Natriumsignale zeigt erstmalig, dass die biochemische Kompartimentierung auch für Natrium wahrscheinlich ist. Die fundamentalen Implikationen für die Funktion, Plastizität und Regulation einzelner Synapsen und deren Signalintegration stellen eine neue Erkenntnis dar, deren Vertiefung durch Anwendung weiterer Messmethoden vielversprechend erscheint.

8 Publikationen und Manuskripte

8.1 Diffusion and Compartmentalization of Sodium in Spiny Dendrites

Status: Wird in den nächsten 4 Wochen wiedereingereicht.

Experimenteller Beitrag (siehe auch 'Author Contributions'): 80%. Ich habe ca. 3/4 aller Experimente und die Analyse der Daten durchgeführt. Zudem war ich an der Erstellung des experimentellen Konzepts, der Interpretation der Daten, der Verfassung des Manuskripts sowie der Abbildungen maßgeblich beteiligt.

Diffusion and Compartmentalization

of Sodium in Spiny Dendrites

Christian Kleinhans[1], Niklas J. Gerkau[1], Hartmut Schmidt[2],

Karl W. Kafitz[1], and Christine R. Rose[1*]

[1] Institute of Neurobiology, Faculty of Mathematics and Natural Sciences, Heinrich Heine University Düsseldorf, Universitätsstrasse 1, D-40225 Düsseldorf, Germany

[2] Carl-Ludwig-Institute for Physiology, Medical Faculty, University of Leipzig, Liebigstr. 27, 04103 Leipzig, Germany

Short title: Sodium diffusion in spiny dendrites

[*] **Corresponding author:** Prof. Dr. Christine Rosemarie Rose, Institute of Neurobiology, Faculty of Mathematics and Natural Sciences, Heinrich Heine University Düsseldorf, Universitätsstrasse 1, D-40225 Düsseldorf, Germany. Phone: ++49 (211) 81 13416; Fax: ++49 (211) 81 13415; e-mail: rose@uni-duesseldorf.de

722 Number of pages: Figures: Tables:

723 Number of words in the Abstract: Introduction: Discussion:

724

725

726 **Acknowledgements:** This work was supported by the *Deutsche Forschungsgemeinschaft*

727 (German Research Foundation; Ro2327/6-1; SCHM1838). We thank Simone Durry and

728 Claudia Roderigo for excellent technical assistance.

Abstract

Influx of sodium ions through voltage- and ligand gated channels is the dominating mechanism of neuronal excitation. While diffusion and compartmentalization of second messengers like calcium were extensively explored in neurons, surprisingly little is known about these processes for sodium ions, representing the major charge carriers. Here, we addressed these questions in mouse CA1 pyramidal neurons *in situ* using whole-cell patch-clamp combined with multi-photon sodium imaging. Sodium transients were induced by extracellular glutamate uncaging, local electroporation or synaptic stimulation. Our data show that sodium ions diffuse with an apparent diffusion coefficient of 160 $\mu m^2/s$ along dendrites. Sodium signals are similar in amplitude and decay time course in dendrites and short-neck spines, indicating fast diffusional equilibration of sodium between these compartments. In long-neck spines, in contrast, sodium transients generated in the dendrite appear only delayed and dampened, while synaptically-induced sodium signals are faster, larger and display different decay kinetics as compared to parent dendrites. These results are replicated by a numerical simulation of diffusion between dendritic segments and spines of different neck lengths, which also predicts active extrusion of sodium from the necks. Taken together, our results provide the first direct experimental evidence that long spine necks serve as significant diffusional barriers for sodium ions. This results both in a substantial retention of sodium in spines that experience direct influx and in a protection of spines from dendritic sodium signals. The demonstrated compartmentalization of sodium supports the proposed electrical compartmentalization of long-neck spines, and may thus be an important mediator of synaptic weight.

Introduction

Sodium ions represent basic charge carriers for the generation of action potentials and excitatory postsynaptic currents in the brain. Influx of sodium accompanying neuronal activity can result in changes in the intracellular sodium concentration. Several studies have described that action potentials cause a transient increase in the sodium concentration of axons of central neurons (Lasser-Ross and Ross, 1992; Kole et al., 2008; Fleidervish et al., 2010). Activity-induced sodium transients can also arise in dendrites and spines in response to the opening of voltage-gated sodium channels during back-propagating action potentials, as shown e.g. for hippocampal CA1 pyramidal neurons (Jaffe et al., 1992; Rose et al., 1999). The amplitude of these sodium signals was larger in spines than in the directly adjacent dendrite, indicating the functional expression of voltage-gated sodium channels in spine heads (Rose et al., 1999), an assumption supported later by studies in neocortical neurons (Araya et al., 2007) and in olfactory bulb granule cells (Bywalez et al., 2015). Particularly prominent sodium transients are evoked in response to excitatory synaptic activity in postsynaptic elements. In hippocampal CA1 neurons, short-burst activation of Schaffer collaterals resulting in suprathreshold postsynaptic activity, was accompanied by a local sodium increase by about 10 mM in dendrites and by about 30 mM in so-called "active spines", which was mainly mediated by NMDA-receptors (Rose and Konnerth, 2001).

Despite the high functional relevance of changes in intracellular sodium for electrical and biophysical properties of neurons, knowledge about the spatio-temporal extent of activity-induced intracellular sodium signals is very limited. For example, fundamental parameters such as diffusion properties of sodium within neuronal microdomains are practically unknown. Early studies revealed a high mobility of sodium ions in the cytosol of muscle fibers (790 μm^2/sec; (Allbritton et al., 1992) and large-caliber axons (1,300 μm^2/s; (David et al., 1997). These values are close to those obtained in water (1,200 μm^2/sec

779 (Kushmerick and Podolsky, 1969), indicating fast and efficient intracellular diffusion of
780 sodium. Notably, and in contrast to this notion, differences in the sodium concentration are
781 apparently maintained for hundreds of milliseconds between spines and adjacent dendrites
782 following synaptic activation or back-propagation of action potentials (Rose et al., 1999;
783 Rose and Konnerth, 2001). Because no relevant endogenous buffer systems seem to exist for
784 sodium (Despa and Bers, 2003; Fleidervish et al., 2010), equilibration of sodium
785 concentrations between spines and dendrites should occur much more rapidly if its diffusion
786 coefficient was in the range of those reported above.

787 This disagreement between the expectation and existing experimental reports implies
788 that either buffer systems for sodium ions must exist and/or that the actual diffusion of
789 sodium in neuronal microdomains such as dendrites and spines is much slower. A related
790 and highly relevant question is if spines compartmentalize sodium signals, analogous to the
791 situation described for calcium ions (Yuste et al., 2000). Such compartmentalization of
792 sodium could be the consequence of hindered diffusion in the spine neck (Sabatini et al.,
793 2002) and/or to the „dilution" of sodium ions during their diffusion from the spine into the
794 much larger volume of the dendrite (Schmidt et al., 2007). Differences in morphology of
795 spines and/or their necks might then inherit different sodium compartmentalization
796 properties, an effect which could play an important role in the electrical isolation of a synapse
797 and hence in defining its strength (Korkotian et al., 2004; Grunditz et al., 2008; Harnett et
798 al., 2012; Araya et al., 2014; Sala and Segal, 2014; Tønnesen et al., 2014).

799 In the present study, we addressed these questions by performing high-resolution
800 sodium imaging in spiny dendrites of CA1 pyramidal neurons combined with whole-cell
801 patch-clamp to characterize the diffusional properties of sodium ions and the spread of
802 sodium signals along dendrites of principal neurons. Furthermore, we studied sodium
803 diffusion between dendrites and spine heads to reveal if spine necks serve as diffusional
804 filter for sodium ions. Our study demonstrates that sodium diffusion in neuronal dendrites

805 is slower than previously thought. In addition, it provides evidence for a
806 compartmentalization of sodium in dendritic spines that is governed by the geometry of
807 their spine neck.

Materials and methods

Tissue preparation and salines

This study was carried out in strict accordance with the institutional guidelines of the Heinrich Heine University Düsseldorf, as well as the European Community Council Directive (86/609/EEC). All experiments were communicated to and approved by the Animal Welfare Office at the Animal Care and Use Facility of the Heinrich Heine University Düsseldorf (institutional act number: O52/05), following the recommendation of the European Commission (published in: Euthanasia of experimental animals, Luxembourg: Office for Official Publications of the European Communities, 1997; ISBN 92–827–9694-9).

Balb/c mice on postnatal day 14-18 were used to prepare parasagittal hippocampal slices employing standard procedures (Edwards et al., 1989; Meier et al., 2006). In brief, mice were anesthetized by CO_2, decapitated and their brains rapidly removed and placed in ice-cold modified artificial cerebrospinal fluid (mACSF), containing (in mM): 125 NaCl, 2.5 KCl, 0.5 $CaCl_2$, 6 $MgCl_2$, 1.25 NaH_2PO_4, 26 $NaHCO_3$, and 20 glucose, bubbled with 95% O_2 and 5% CO_2, resulting in a pH of 7.4 and an osmolarity of 310±5 mOsm/l. After tissue trimming, hippocampi were cut into 250 µm thick slices using a vibratome (HM 650 V, Thermo Fisher Scientific, Waltham, MA). Slices were incubated at 34° C for 30 minutes and subsequently kept at room temperature (20-22°C) in standard ACSF (containing in mM: 125 NaCl, 2.5 KCl, 2 $CaCl_2$, 1 $MgCl_2$, 1.25 NaH_2PO_4, 26 $NaHCO_3$, and 20 glucose, bubbled with 95% O_2 and 5% CO_2, resulting in a pH of 7.4).

During experiments, which were also performed at room temperature, slices were perfused with ACSF. With the exception of synaptic stimulation experiments, all experiments were carried out in the presence of 500 nM tetrodotoxin (TTX) to block action

potential generation, unless stated otherwise. Chemicals were purchased from Sigma-Aldrich Chemicals (Munich, Germany), except for TTX (Biotrend, Cologne, Germany).

Electrophysiology and Sodium Imaging

Whole-cell patch-clamp recordings were performed using borosilicate glass micropipettes filled with intracellular solution containing (in mM): 120 K-$MeSO_3$, 10 HEPES (4-(2-hydroxyethyl)-1-piperazineethanesulfonic acid), 32 KCl, 4 NaCl, 1 EGTA (ethylene glycol tetraacetic acid), 4 Mg-ATP, 0.4 Na-GTP, titrated to a pH of 7.3 with KOH. Pipette resistance was 2.5-3 MΩ. For sodium imaging, the sodium-sensitive fluorescent dye SBFI (K^+ salt of sodium-binding benzofuran isophtalate; TEFLabs, Austin, TX) was added to a final concentration of 1.25 mM.

CA1 pyramidal cells were subjected to voltage-clamp at a holding potential of -60 mV using an EPC-10 patch-clamp amplifier and Patchmaster 2.32 software (HEKA Elektronik, Lambrecht, Germany). Liquid junction potential was not corrected. Experiments were discarded if access resistance exceeded 15 MΩ. Cells were held for at least 30 minutes to allow diffusion of SBFI into the fine processes before commencing imaging experiments. Data were sampled at 10 kHz and processed and analyzed employing Origin 9.0 software (Origin Lab, Northampton, MA). All imaging and stimulation devices were coupled to the patch-clamp amplifier and synchronized through the Patchmaster software.

Imaging was performed using a custom-built multiphoton laser-scanning microscope based on a Fluoview 300 system (Olympus Europe, Hamburg, Germany), equipped with a water immersion objective (NIR Apo 60x/NA 1.0, Nikon Instruments Europe, Düsseldorf, Germany). For excitation, a tunable femtosecond-pulsed IR laser (MaiTai; Spectra Physics, Darmstadt, Germany) was used. Excitation wavelength was 790 nm, fluorescence emission was collected below 700 nm. After completion of sodium

imaging experiments, cellular morphology was recorded by taking z-stacks of SBFI fluorescence (z-steps: 1 µm; x-y-resolution: 0.51 µm/pixel; 2x Kalman filter). Z-stacks of spiny dendrites were taken at an x-y-resolution of 0.2 µm/pixel and an optical section thickness of 0.2 µm. z-stacks were post processed employing deconvolution (Huygens Professional, SVI imaging, Hilversum, Netherlands).

SBFI imaging experiments were carried out on primary and secondary apical dendrites of pyramidal neurons at a distance of 60-100 µm from the soma. Clip box time-lapse recordings were performed at 5 or 10 Hz, line scans at 700 Hz. Data were corrected for bleaching and analyzed with FluoView software (time lapse analysis; FluoView 5.0, Olympus Europe), ImageJ (scale bars and z-stack projection; National Institutes of Health, Bethesda, MD), and Origin 9.0 (image and electrophysiology data processing). Changes in SBFI fluorescence were converted into changes in Na^+ concentration based on an *in situ* calibration performed as described earlier (Rose et al., 1999). To this end, a neuron was filled with SBFI, after which the patch-pipette was carefully retracted and the plasma membrane was allowed to re-seal. Slices were then superfused with calibration ACSF containing 10 mM sodium (KCl increased to 117.5 mM to maintain osmolarity) as well as the ionophores gramicidin (3 µM), monensin (10 µM) and ouabain (100 µM) to equilibrate intra- and extracellular [Na^+] for 20 minutes. After recording SBFI fluorescence from the soma and apical dendrite, the [Na^+] of the calibration ACSF was changed and resulting changes in fluorescence emission recorded (Fig. 1A). Data obtained from individual cells (n=5, N=5) were normalized to the fluorescence levels at 10 mM $[Na^+]_i$ and plotted versus the $[Na^+]_i$. A linear fit of the averaged data between 10 and 50 mM $[Na^+]_i$ revealed that a 10% change in fluorescence corresponded to a change in $[Na^+]_i$ by 13.4 mM in this concentration range (Fig. 1B).

Uncaging, electroporation and synaptic stimulation

For induction of intracellular sodium transients, focal uncaging of glutamate was carried out using a confocal UV laser scanning photolysis unit (UGA 40, including a 355 nm/10 mW UV laser; Rapp OptoElectronic, Hamburg, Germany). Simultaneous import of the multi-photon imaging feed into the uncaging software allowed for precise positioning of the uncaging beam (Kleinhans et al., 2014). The UV laser spot size in the focal plane (x/y dimension) was 1.5 µm. For application of caged glutamate, a glass micropipette (pulled with the same settings as for patch clamp pipettes) was filled with HEPES-buffered ACSF containing 10 mM MNI-caged glutamate (Tocris Bioscience, UK) and positioned close (~15 µm) to an SBFI-filled dendrite using a micromanipulator (Burleigh PCS5000, npi electronic, Tamm, Germany). The compound was focally ejected into the tissue for 5 seconds using a pressure application system at low pressure (<5 PSI; PDES nxh, npi electronic, Tamm, Germany). 3 seconds after stopping the injection, imaging was launched and an uncaging flash was applied centered at a distance of about 1 µm from a dendrite.

Alternative to UV-uncaging, direct electroporation of dendrites was performed to evoke local influx of sodium. To this end, glass pipettes with a tip diameter <1 µM were pulled (pipette puller PP-830; Narishige, Tokyo, Japan), filled with HEPES-buffered ACSF (resistance ~15 MΩ) and connected to a stimulus generator (Isolated Stimulus Generator Model 2100, A-M Systems, Carlsborg, WA). The electroporation pipette was positioned in the direct vicinity (1-2 µm) of an SBFI-filled dendrite (cf. Fig. 3A, B, C) and a rectangular stimulation pulse was applied (pulse duration: 5-8 ms, amplitude: 2-3.5 µA).

For induction of sodium influx upon synaptic release of glutamate, a glass micropipette filled with HEPES-buffered ACSF was lowered into the stratum radiatum and a train of stimuli (10 pulses at 200 µs delivered at 50 (frame recordings) or 100 Hz (line scans)) was delivered to evoke action potentials and release of glutamate from Schaffer Collaterals.

Statistics

Unless otherwise specified, data are presented as means ± S.E.M. and were statistically analyzed by two-tailed paired-sample Wilcoxon signed rank test; *p* represents error probability, n.s. = not significant, * $p < 0.05$, ** $p < 0.01$, *** $p < 0.001$; *n* represents the number of cells, *N* the number of slices studied. All experiments were repeated on at least 3 different animals.

Modeling

Simulations were performed with Mathematica 10.1 (Wolfram Research, Champaign, IL) by numerically solving a set of coupled ordinary differential reaction diffusion equations (Helmchen and Tank, 2005; Schmidt and Eilers, 2009). Spine head (volume of 0.036 μm^3 (Takasaki et al., 2013)) and dendritic segments (radius 0.6 µm (Araya et al., 2006b), length of each segment 1 µm (calculated according to the spine density of 1/µm (Santamaria et al., 2011; Gu et al., 2014)) were modeled as well mixed compartments, diffusionally coupled via a spine neck (radius r_{neck} of 0.1 µm) of variable length (l_{neck} of 0.1 or 1.4 µm, respectively (estimated from 3D stacks; cf. (Nagerl et al., 2008; Wijetunge et al., 2014) for similar values)). A Gaussian shaped Na^+ influx (width 0.3 s) was either placed into the spine head or a dendritic compartment. Resting concentration of Na^+ was set to 13 mM (Kelly and Rose, 2010). The diffusional flux (J_D) between spine and dendrite was simulated as

$$J_D = (D_{Na}\, \pi\, r_{neck}^2 / l_{neck})\, ([Na]_{spine}(t) - [Na]_{dendrite}(t))$$

where D_{Na} is the diffusion coefficient of Na^+ (160 $\mu m^2/s$ unless denoted otherwise, cf. Fig 4C). Na^+ dynamics were simulated as

$$(d[Na]/dt)_{spine} = (Influx - \gamma([Na]_{spine}(t) - [Na]_{rest}) - J_D/V_{head})/(1+\kappa_B)$$

$$(d[Na]/dt)_{dendrite} = (-\gamma([Na]_{dendrite}(t) - [Na]_{rest}) + J_D/V_{dendrite})/(1+\kappa_B)$$

where V denotes the volume of the respective compartment, γ the pump rate (0.25 s^{-1} for spine and dendrite, unless stated otherwise), and κ_B the buffer capacity added by the indicator dye (calculated from a K_D of 24 mM and the dye concentration of 1 mM). The amplitude (spine: 6.3 pC/s; dendrite 21 pC/s) of the sodium influx and γ (0.25 s^{-1}) were the free parameters of the simulation and adjusted to match the experimental data. Diffusion between dendritic segments and corresponding segment dynamics was simulated analogously.

Results

Sodium transients evoked by focal uncaging of MNI-glutamate

To evoke postsynaptic sodium transients in hippocampal neurons, we employed focal UV-uncaging of MNI-caged glutamate close to a chosen dendrite as described earlier (Kleinhans et al., 2014). Sodium imaging was performed along a 10-15 µm long dendritic region of interest including adjacent spines. Experiments were performed in the presence of TTX to prevent action potential generation.

Glutamate uncaging resulted in a somatic inward current as well as a transient sodium signal in the spiny dendrite close to the uncaging site (n=14, N=10; Fig. 2A). Both were reversibly blocked by combined application of CNQX and AP5, demonstrating their dependence on the opening of AMPA and NMDA receptors (n=4, N=4; Fig. 2B; (Kleinhans et al., 2014)). Total influx charge and peak amplitude of sodium transients increased with increasing duration of the uncaging flash, following a linear correlation of 1.7 ± 0.2 pC/mM Na^+ (n=14, N=10; Fig 2C, D). Detection threshold was a ~4-5% change in SBFI fluorescence, corresponding to a change in sodium by ~5-7 mM (cf. Fig. 1), and flash durations of ≥50 ms and currents with a total charge of ≥10 pC were required to induce such signals (Fig. 2C, D). Uncaging for 200 ms resulted in a current exhibiting a 10-90% rise time of 172 ± 24 ms, an average peak of 183 ± 26 pA and a charge of 61 ± 7 pC. It was accompanied by a dendritic sodium increase by 30 ± 4 mM which decayed monoexponentially (decay time constant τ: 3.7 ± 0.6 s; n=11, N=8; Fig. 2A). Sodium transients could also be detected in single spines in response to glutamate uncaging. Amplitude and time course of spine signals were not significantly different from those in adjacent dendrites (n=11, N=3; Fig. 2E). It is important to note, however, that the uncaging flash obscured the rising phase of sodium transients.

In addition, sodium signals were not limited to dendritic sections close to the uncaging site, but could usually be detected with similar amplitudes and time course in different regions of interest along a dendrite in the field of view including adjacent spines (n=14, N=10; Fig. 2E). Finally, sodium transients were usually not limited to dendrites (and spines) directly at the uncaging site, but could also be observed in close neighboring dendrites. In this case, the amplitude of sodium transients decreased with increasing distance from the uncaging site (n=5, N=3; Fig. 2F).

These data show that the opening of ionotropic glutamate receptors following focal UV-uncaging of glutamate induces sodium influx and sodium transients in dendrites and adjacent spines. Sodium signals were similar in spines and dendrites and not restricted to regions directly adjacent to the uncaging site. This indicates that the relatively long duration of uncaging, necessary to resolve sodium signals, allowed substantial diffusion of glutamate from its point of uncaging, resulting in the stimulation of receptors in a larger cellular area and, consequently, in non-focal sodium influx. Moreover, the data suggest that, in addition, fast intracellular diffusion might promote the efficient intracellular spread of sodium ions.

Sodium transients evoked by direct electroporation

In order to eliminate the contribution of glutamate diffusion, we next performed direct electrical stimulation, an approach established earlier for hippocampal astrocytes *in situ* to induce fast sodium influx (Langer et al., 2012). To this end, a fine-tipped glass pipette (tip diameter <1 µM) was positioned at a distance of 1-2 µm from a SBFI-filled dendrite, and a short rectangular stimulation pulse (5-8 ms, 2-3.5 µA) was delivered. Resulting changes in SBFI fluorescence were analyzed in a 10-15 µm long region of interest along the dendrite, centered at the pipette tip (Fig. 3A). The electrical stimulation induced in a transient inward current that exhibited a 10-90% rise time of 11 ± 2 ms, a peak amplitude

of 239 ± 30 pA and a total charge of 67 ± 8 pC. It was accompanied by a transient sodium increase of on average 23 ± 2 mM (n=27, N=18; Fig. 3A). The rise time of the sodium signal as recorded in the frame mode at 5-10 Hz was in the range of 200-400 ms and decay time was 6.0 ± 0.7 ms (n=27, N=18).

Peak amplitudes of inward currents and dendritic sodium signals caused by electroporation were dependent on the distance of the stimulation pipette from the dendrite. Slowly retracting the pipette from its original distance on the dendrite resulted in smaller peak currents and sodium transients and *vice versa* (n=4, N=4; Fig. 3B, 3C). As described above for glutamate uncaging, influx charge and respective sodium peak amplitude were linearly correlated (slope: 2.7 ± 0.3 pC/mM sodium; n=27, N=18; Fig. 3D). Compared to uncaging, the slope of this relationship was 1.6-fold larger (2.7 vs. 1.7 pC/mM, see above), a difference most likely due to the fact that ionotropic glutamate receptor currents represent mixed cation currents with sodium influx counteracted by efflux of potassium. Taken together, direct electroporation of a dendrite thus resulted in membrane currents as well as dendritic sodium transients with similar characteristics as those obtained with application of the natural ligand glutamate.

This stimulation paradigm was then employed to analyze sodium signals at dendritic regions further away from the stimulation pipette. To this end, electrical stimulation was performed repeatedly at the same site and the resulting sodium transients recorded sequentially in regions of interest placed along the dendrite at various distances from the site of stimulation (Fig. 4A). In contrast to what was observed with glutamate uncaging, sodium signals detected in regions along a dendrite showed a clear dependence on their distance from the stimulation site concerning amplitude and time course (Fig. 4B). Thus, in dendritic regions located further away from the stimulation pipette, peak amplitudes decreased while the delay between the stimulation event and peak increased

(Fig. 4 A, B), indicating that sodium entered locally at the stimulation site and then diffused along the dendrite.

Based on these experiments, we estimated the apparent diffusion coefficient for sodium. To determine the distance between two regions of interest, the intensity center of mass for each region of interest was computed and used as anchor point. For each measurement, the delay between stimulation and sodium signal peak was determined. If sodium signals lacked a clear peak, the data traces were fitted polynomially and the maximum was calculated by curve tracing (Fig. 4B). Molecular displacement x and propagation time t were entered in the one dimensional diffusion equation ($D \sim x^2/2t$) as described in previous studies (Popov and Poo, 1992; Zhai et al., 2013) to obtain a first-order estimate of the apparent diffusion coefficient D_{Na+}. The resulting value was 165 $\mu m^2/s$ ± 23 $\mu m^2/s$ (n=19, N=7; Fig. 4C).

These results demonstrate that direct electrical stimulation of a dendrite results in dendritic sodium transients at the stimulation site that are comparable in amplitude and decay time course to those obtained upon with prolonged glutamate uncaging. In contrast to what was observed with glutamate uncaging, however, sodium influx induced by direct electroporation is fast and rather local. Upon its entry, sodium diffuses along dendrites from the site of stimulation with an apparent diffusion coefficient of about 165 $\mu m^2/s$, resulting in well detectable sodium signals also in distant regions.

Sodium diffusion between dendrites and spines

In a next set of experiments, we analyzed the characteristics of sodium diffusion from dendrites into spines. To this end, we performed a direct electrical stimulation of a spiny dendrite using the approach established above. Sodium transients were recorded in a 2-3 µm long dendritic section and in spines emerging from this section at a distance of ~5 µm from the stimulation site (Fig. 5A, 5C). Average influx charge and dendritic sodium

elevation for this set of experiments were in the same range as before (79 pC ± 18 pC, 30 ± 5 mM; n=22, N=14; cf. Fig. 5E). After each experiment, high resolution z-stacks of the spiny dendrite were taken, allowing offline assessment of spine morphology after image deconvolution (Fig. 5A, C: insets). All analyzed spines exhibited a sodium increase in response to the stimulation, indicating efficient diffusion of sodium from dendrites. Interestingly, however, the properties of spine signals appeared to substantially dependent on the length of the spine necks.

In order to substantiate this observation we distinguished between long-necked spines (>1 µm; average apparent length 1.4 µm, n=14, N=9; Fig. 5A, B) and short-necked spines (<0.5 µm; with ~0.4 µm representing the maximal optical resolution in our system; n=8, N=5; Fig. 5 C, D). Sodium signals in individual long-neck spines exhibited an apparent slower rise and a blunted as well as slightly smaller peak as compared to their parent dendrite (Fig. 5A). Averaging the data traces obtained from 14 individual spine-dendrite pairs allowed a more detailed analysis (Fig. 5B). A linear fit of the 10–90% interval of the rising phase of sodium signals revealed a slope of 20 mM/s in long-neck spines and of 78 mM/s in adjacent dendrites. Between 200 and 500 ms after stimulation, the sodium concentration in long-neck spines was significantly lower than in dendrites. Furthermore the peak of the spine sodium signal (27 ± 5 mM) was delayed by about 0.5 s as compared to the dendrite (peak: 30 ± 4 mM). Monoexponential fitting revealed a decay time constant of τ=6.0 s (R^2=0.86) for spines and τ=4.2 s (R^2=0.92) for dendrites.

In contrast to this, no significant difference in amplitudes or time courses was detected between sodium signals of short-neck spines and their parent dendrites (Fig. 5C, D). The slope of the rising phase of short spines was 82.5 mM/s as compared to 87.4 mM/s in the dendrite. Peak amplitudes (short spines: 34 ± 3 mM; dendrites: 35 ± 5 mM) and decay

time constants (short spines: τ=5.5 s, R^2=0.92; dendrites: τ=5.4 s, R^2=0.96) were similar as well.

In summary, these data show that although sodium diffuses from dendrites into adjacent spine, the details of the spine signal are strongly influenced by the morphology of the spine neck: For short-neck spines, we found that sodium signals are virtually identical in time course and amplitude in the parent dendrite and spine head. In spine heads of long-neck spines, in contrast, the increase in sodium concentration is delayed and its slope less steep than in the parent dendrite, indicating that long spine necks represent significant filters for sodium diffusion.

Sodium signals induced by synaptic activity in dendrites and spines

In order to probe whether our above observations hold for more natural stimuli, we used a synaptic stimulation protocol to trigger release of glutamate and transient sodium influx into spines through postsynaptic AMPA and NMDA receptors (Rose & Konnerth, 2001). To this end, a saline-filled glass pipette was positioned in the *stratum radiatum* near the CA3 region for Schaffer Collateral stimulation. A spiny apical dendrite at a distance of 50-100 µm from the cell body of an SBFI-filled cell was chosen and regions of interest were set around spines as well as adjacent dendritic sections of 2-3 µm in length (Fig. 6A).

Schaffer Collateral stimulation (10 pulses at 50 Hz) reliably induced inward currents at the soma with peak amplitudes of around 500-1000 pA (n=17; Fig. 6B). Fast-rising sodium transients were observed in ~25% of spiny dendrites chosen. Inward currents and sodium transients were blocked by TTX, indicating that they depended on the generation of neuronal action potentials (n=4, N=4; not shown). Because sodium signals were not seen throughout the entire apical dendritic tree, several dendritic regions of a given cell were usually imaged sequentially and data analyzed off-line. Single spine signals could be retrieved from a total of 38 spines. From these, only two spines exhibited necks

with an apparent length of >1 µm. Thus, for this set of experiments, spines were separated into a group in which the spine head was clearly separated from the dendrite ("long spines", exhibiting apparent neck lengths of >0.7 µm; number of analyzed spines: 16), and a second group with heads directly adjacent to the dendrite ("short spines" with apparent neck lengths of <0.7 µm; number of analyzed spines: 22).

Long spines exhibited a rapid rise in sodium to a maximum of 40 ± 4 mM, which was reached between 400 and 600 ms after the onset of stimulation (n=16, N=9; Fig. 6B, C). In their parent dendrites, sodium rose to 30 ± 2 mM only, a value significantly lower than that of the spines (Fig. B, C). This phenomenon was already detectable in individual recordings (Fig. 6 B), but clearly evident in averaged traces (Fig. 6 C). The decay of spine sodium signals was fitted best using a biexponential function (decay times τ_1=0.7 and τ_2=10.8 s, R^2=0.84), whereas signals in their parent dendrites decayed monoexponentially (τ=10.7 s, R^2=0.93; Fig. 6B, C). In contrast to this, sodium transients in short spines were not significantly different from the signal in their parent dendrites both in terms of peak amplitude (spines: 35 ± 4 mM, dendrites: 30 ± 3 mM; n=22, N=8) as well as decay time course (both were best fit with a monoexponential function: spines: τ=9.8 s, R^2=0.91; dendrites: τ=10.0 s, R^2=0.97; Fig. 6B, C).

To study the rising phase of synaptically-induced sodium signals, line-scan recordings were performed (stimulation: 20 pulses @ 50 Hz; N=10). Because success rate was 25% for dendritic regions chosen (see above), the presence of a fast sodium signal was first ensured by frame recordings from the dendrite. Subsequently, a line was set perpendicular to the parent dendrite through the center of a spine and SBFI fluorescence emission along this line was sampled at 700 Hz (Fig. 7A, B). As observed for frame recordings, synaptically-evoked changes in SBFI fluorescence exhibited a steeper slope in long spines as compared to their parent dendrite and displayed a larger amplitude (n=12;

Fig. 7D). In short spines, both slope and amplitude of changes in SBFI fluorescence were similar than in adjacent dendrites (n=12; Fig. 7D).

These data indicate that the spine neck morphology influences sodium signals in spine heads as induced by synaptic release of glutamate. Spine heads that are clearly separated from the dendrite, thus apparently exhibiting a long spine neck, undergo sodium transients that are faster and larger than their parent dendrite upon synaptic stimulation. In spine heads with a seemingly short neck, no difference in synaptically-induced sodium signaling can be detected as compared to their parent dendrite.

Numerical modeling of Na^+ dynamics in spines and dendrites

The D-value estimated here is substantially smaller than previous estimates. In order to test its plausibility and for a better understanding of the cellular factors that govern sodium diffusion between dendrites and spines and *vice versa*, we applied a numerical simulation (see methods). First, sodium influx, was placed onto either a long-neck or a short-neck spine and sodium extrusion by the sodium extrusion was introduced in the spine head and the dendrite (Fig. 8A). We then varied the sodium diffusion coefficient D_{Na+} between 600 µm²/s, a value reported earlier (Kushmerick and Podolsky, 1969), and 160 µm²/s as determined in the present study (cf. Fig. 4).

For long-neck spines, the simulations revealed a strong impact of the chosen diffusion coefficient on the amplitude of the sodium elevation. In all cases, long-neck spines experienced a faster and higher increase in sodium than their adjacent dendrite. This effect was largest at a D_{Na+} of 160 µm²/s, but still visible at 600 µm²/s. Lowering D_{Na+} from 600 to 160 µm²/s also resulted in a change in the decay time course of long-neck spines (Fig. 8A). In stark contrast, for short-neck spines, rise times, amplitudes and decay of sodium signals were essentially indistinguishable from those of neighboring dendrites. The model, however, predicts that the rise in spine sodium slightly precedes that of dendrites

(Fig. 8 A). Thus, with a smaller D-value of ~160 $\mu m^2/s$ we obtained a much better reproduction of our experimental data than with a high D-value.

We next tested if the model reproduced our experimental data also for sodium influx into the dendrite and subsequent diffusion into a spine head, mimicking our experimental approach of direct electrical stimulation of dendrites. Here, we found, that sodium transients were virtually similar in both compartments, independent from the neck length (Fig. 8B). Thus, diffusion from dendrites into spines seems to be much more efficient than the other way around. This is in agreement with an earlier study which showed that the neck radius, but not its length, determine longitudinal diffusion (Santamaria et al., 2011).

To address this apparent inconsistency of the model with our experimental data, we repeated the above simulations with D_{Na+} set at 160 $\mu m^2/s$ and with the additional presence of NKA along the necks (Fig. 8C). In long-neck spines, this parameter did not influence the rise time nor peak amplitude of the sodium signal, but promoted its recovery by slightly accelerating the first recovery phase. In addition, sodium accumulation in dendrites was decreased slightly. As expected, no influence was seen for short-neck spines.

Sodium influx was then placed onto the neighboring dendritic segment. With NKA present in all three compartments (spine head, neck and dendrite), dendritic sodium increased faster and to higher levels than sodium in adjacent long-neck spines. Spine sodium never fully equilibrated with that of the dendrite, but was slightly lower during the entire simulation period (3 s). Again, sodium signals were essentially undistinguishable in dendrite and adjacent short-neck spines (Fig. 8D).

Taken together, our model predicts that sodium diffuses rapidly between dendrites and adjacent short-neck spines, resulting in a rapid equilibration of sodium concentrations between those two compartments and essentially identical sodium signals for diffusion from dendrites into spines. If sodium enters spine heads, sodium signals precede those in the dendrite by 20-30 ms, but otherwise curves are essentially identical in terms of time

course and amplitude. For long-neck spines, the outcome is dramatically different. In this case, the simulations reveal a significant diversion of sodium signals in spine heads as compared to adjacent dendrite sections. This phenomenon is most distinct when using the low D_{Na+} as determined experimentally in our study and especially prominent with direct sodium influx into the spine head, in which sodium is significantly higher than in the parent dendrite for hundreds of ms after the stimulation. Finally, our model predicts the existence of NKA and direct sodium extrusion from the spine necks.

Discussion

Here we show that sodium ions spread with an apparent diffusion coefficient of 160 µm²/s along spiny dendrites. Diffusion of sodium between dendrites and spines (and *vice versa*) is strongly dependent on the length of spine necks. With short spine necks, sodium signals are similar in amplitude and decay time course in dendrites and spines. In long-neck spines, however, sodium transients generated in the dendrite, appear only delayed and dampened. On the other hand side, synaptically-induced sodium signals are faster, larger and display different decay kinetics in long-neck spines as compared to parent dendrites. These results are replicated in a modeling approach, in which diffusion between dendritic segments and spines was simulated numerically. Taken together, our study indicates that long spine necks serve as significant diffusional barriers for sodium ions, resulting in a substantial retention of sodium in spines that experience direct sodium influx. The demonstrated compartmentalization of sodium supports the proposed electrical compartmentalization of long-neck spines and may thus be an important mediator of synaptic weight.

Activity-related sodium signals and diffusion of sodium along dendrites

Influx of sodium through voltage- and ligand gated channels is a major mechanism for the generation of plasma membrane depolarization. Recent work has established that excitatory activity induces significant sodium transients in central neurons. For example, strong recurrent network activity is accompanied by global and synchronous neuronal sodium oscillations in the hippocampus (Karus et al., 2015b; Karus et al., 2015a). Sodium signals are generated upon the opening of voltage-gated sodium channels in both axons (Kole et al., 2008; Fleidervish et al., 2010; Baranauskas et al., 2013) and -with back-propagating action potentials present- in dendrites and spines (Jaffe et al., 1992; Rose et al., 1999). In addition, synaptic stimulation of glutamatergic afferents or exogenous

application of glutamate induce sodium transients that are largely restricted to dendrites and spines close to activated synapses (Lasser-Ross and Ross, 1992; Knopfel et al., 2000; Rose and Konnerth, 2001; Meier et al., 2006; Bennay et al., 2008; Kleinhans et al., 2014). Our data confirm these observations by showing that uncaging of extracellular glutamate as well as short-burst stimulation of Schaffer Collaterals results in opening of ionotropic glutamate receptors and sodium transients in dendrites and spines of CA1 pyramidal neurons.

The detection threshold for postsynaptic sodium signals was ~5 mM, that is an increase above baseline by about 50%, and required the generation of long-lasting somatic inward currents and long periods of UV uncaging or burst-stimulation (5-10 pulses) of afferent fibers, which is in line with our earlier study (Rose and Konnerth, 2001). Postsynaptic calcium signals in spines, in contrast, can be detected already with single, subthreshold stimulation (Denk et al., 1995; Eilers et al., 1995; Yuste and Denk, 1995; Koester and Sakmann, 1998; Schiller et al., 1998). Interestingly, synaptically-induced sodium signals described earlier were only observed with suprathreshold stimulation and opening of NMDA receptors (Rose and Konnerth, 2001). This implies that sodium signals are especially prominent during the coincident occurrence of synaptic potentials and back-propagating action potentials, conditions which foster synaptic plasticity at CA3-CA1 synapses.

Local sodium influx induced by direct electroporation enabled an experimental estimate of the apparent diffusion coefficient D_{Na+} along apical dendrites. The obtained value of 160 µm²/s is significantly smaller as those determined for free diffusion in aqueous solution (~1500 µm²/s, (Lobo, 1993), in the cytosol of muscle cells (600 µm²/s; (Kushmerick and Podolsky, 1969), oocytes (790 µm²/s; (Allbritton et al., 1992) or along large lizard axons (1300 µm²/s; (Kushmerick and Podolsky, 1969; Allbritton et al., 1992; David et al., 1997). Importantly, the low D_{Na+} as determined in the present study (160

μm²/s) replicated kinetics and amplitudes of sodium transients in the numerical simulations much better than the previously published higher values. This suggests that diffusion of sodium is considerably hindered in spiny dendrites as compared to the cell types and compartments mentioned above. Notwithstanding, the obtained value for sodium diffusion is about 10 times higher than that for (buffered) diffusion of calcium (~13 μm²/s; (Yuste et al., 2000), suggesting that sodium ions still move far more readily than the latter.

Sodium diffusion between dendrites and spines

Employing a D_{Na+} of 160 μm²/s for simulation of sodium diffusion also mimicked the experimentally obtained divergence of spine and dendrite sodium signals in dependence on the length of the spine neck. In both the simulation and the experimental setting, sodium signals that were generated in the dendrite were seen with virtually identical amplitude and time course also in short-neck spines. Sodium signals in spines with long necks, in contrast, were clearly delayed and were smaller in amplitude than those in the dendrite. An equivalent result was obtained when sodium influx was put onto spines only in the simulation and with synaptic stimulation of Schaffer Collaterals. In this case, sodium signals in spines with long necks were faster and larger than in adjacent dendrites, whereas for short-neck spines, no significant difference in rise time or amplitude was seen.

Interestingly, the recovery phase of long-neck spines after synaptic stimulation was best fitted with a biexponential function, a result which was mirrored in the simulation with spine sodium influx only. A biexponential decay of sodium signals in a subset of spines was already reported earlier (Rose and Konnerth, 2001). While in the latter study, no distinction of spine neck morphology was made, it was concluded that biphasic spines represent active spines, i.e. those which received direct synaptic input and sodium influx. The experimental data presented here together with the numerical simulation now extend

this observation by suggesting that biphasic spine responses will be seen in active spines with long-necks only.

Large gradients between spines and their parent dendrites have been reported for calcium ions (Yuste et al., 2000), suggesting that spines may be chemically isolated from dendrites. Our experimental and numerical results now clearly indicate a biochemical, diffusion-mediated sodium compartmentalization in spines which display a long neck. In our modeling approach, this compartmentalization was reproduced in the absence of additional, diffusion-limiting structures such as a spine apparatus (Spacek and Harris, 1997; Segal et al., 2010). In addition to diffusion, extrusion of sodium via the sodium/potassium ATPase (NKA) will shape sodium transients (Rose and Ransom, 1997; Azarias et al., 2012) and was thus included in our model on both spines heads and dendrites. Recent studies using super-resolution microscopy have provided evidence for a compartmentalized distribution of the α3 isoform of the NKA on spine heads, whereas spine necks were shown to partially lack NKA (Blom et al., 2011; Liebmann et al., 2013). While the authors of the latter studies speculated that this promotes the compartmentalization of sodium signals in spines, our modeling approach predicts that the presence of NKA along spine necks does not significantly influence spine sodium signaling for synaptically-induced influx directly into spines. Our experimental data and simulation, on the contrary, indicate that spine heads are somewhat "protected" from dendritic sodium signals due to the extrusion of sodium from the neck.

Consequences of sodium compartmentalization in spines

Spines are the smallest unit of neuronal integration and it is widely established that this phenomenon includes the property to undergo calcium signaling independent from their parent dendrite (Denk et al., 1995; Yuste and Denk, 1995; Sabatini et al., 2002). This compartmentalization mainly results from the presence of immobile buffers and dilution

effects, while calcium bound to mobile buffers can break the spine limit (Sabatini et al., 2002; Schmidt et al., 2007; Schmidt and Eilers, 2009). For the latter process, the neck radius plays an important role. For stubby spines with a large-diameter neck, recovery from calcium transients has been proposed to be governed mainly by diffusion and based on this, such spines have been termed "diffusers". Recovery in spines with longer necks, in contrast was largely mediated by extrusion, and spines were termed "pumpers", respectively (Hayashi and Majewska, 2005; Noguchi et al., 2005).

In contrast to this, sodium is essentially non-buffered and its movement will be largely governed by concentration gradients and free diffusion as described for sodium signals along axons (Fleidervish et al., 2010). Due to the high K_d of SBFI (~25 mM; (Rose et al., 1999; Meier et al., 2006), buffering of sodium by the dye will be negligible as well. In fact, efficient and fast diffusional equilibration of sodium was observed between dendrites and short-neck spines. In this case, our model predicts only a short delay in dendrite signaling after sodium influx into spines, while amplitude and kinetics of spines and dendrite signals are essentially similar.

The situation is, however, quite different for sodium influx into long-neck spines. These show a clear compartmentalization of sodium signals, with significantly faster rise time, larger amplitude and biphasic instead of monoexponential decay kinetics as compared to adjacent dendrites. Since sodium is a major charge carrier in the generation of postsynaptic potentials, a retention of sodium in long-neck spines indicates that these undergo a stronger depolarization than their parent dendrite, a phenomenon which would support an electrical compartmentalization of spines as proposed earlier (Araya et al., 2006a; Araya et al., 2006b; Araya et al., 2007; Grunditz et al., 2008; Bloodgood et al., 2009; Harnett et al., 2012; Araya et al., 2014; Takasaki and Sabatini, 2014; Bywalez et al., 2015). An important morphological determinant for electrical compartmentalization is the length of the spine neck and several papers have indeed provided evidence that spine

depolarization during synaptic input can scale with their neck length and neck resistance (R_{neck}), respectively (Araya et al., 2006b; Arellano et al., 2007; Harnett et al., 2012; Araya et al., 2014; Tønnesen et al., 2014).

In case of an electric decoupling, spine EPSPs will be amplified due to a disparity in input resistance between spine and parent dendrite and a local change in the electric field (Koch and Zador, 1993; Tsay and Yuste, 2004; Holcman and Yuste, 2015). Hence, the opening probability of voltage-dependent ionotropic receptors such as NMDARs or voltage-gated ion channels in the spine head will increase, further enhancing the EPSP and promoting calcium signaling and calcium-mediated downstream mechanisms. Our results support the idea that such processes will specifically be fostered in long-neck spines because these experience sodium compartmentalization. Interestingly, and in line with this notion, synaptically-induced large, biphasic spine sodium signals were dependent on coincident pre- and postsynaptic activity, that is on activation of NMDA receptors in conjunction with back-propagating action potentials (Rose and Konnerth, 2001), and it is exactly these conditions which induce synaptic plasticity at CA3-CA1 pyramidal cell synapses. Our study also suggests that the activity-dependent shortening and widening of spine necks after induction of LTP, proposed to reduce electrical compartmentalization and to increase synaptic efficacy (Araya et al., 2014; Tønnesen et al., 2014), will be accompanied by a breakdown of sodium compartmentalization and a rapid equilibration of spine and dendrite sodium signals, supporting the rapid charge transfer between those two compartments and increase the synaptic weigh of the given spine.

Taken together, our results provide the first direct experimental evidence that long-spine necks serve as significant diffusional barriers for sodium ions, resulting in a substantial retention of sodium in those spines that experience direct sodium influx. The demonstrated compartmentalization of sodium supports the proposed electrical

compartmentalization of long-neck spines, and may thus be an important mediator of synaptic weight.

Figure Legends

Fig. 1: *In situ* calibration of SBFI fluorescence. **A**, Changes in the SBFI fluorescence of the soma and proximal primary dendrite of a CA1 pyramidal neuron in response to changes in the intracellular sodium concentration ($[Na^+]_i$). The experiment was performed in the presence of the ionophores gramicidin and monensin as well as the sodium pump blocker ouabain to equilibrate intra- and extracellular $[Na^+]$. **B**, Relation between $[Na^+]_i$ and relative changes in SBFI fluorescence, normalized to values at 10 mM $[Na^+]_i$. Shown are mean values ± S.E.M obtained from 5 cells. The black line is a linear plot of the data between 10 and 30 mM $[Na^+]_i$, indicating that within this concentration range, a 10% change in fluorescence corresponds to a change in $[Na^+]_i$ by 13.4 mM.

Fig. 2: $[Na^+]_i$ signals evoked by UV photolysis of caged glutamate. **A**, Top: maximal intensity projection image of a neuron loaded with SBFI via the patch pipette (PP). The box indicates the area shown enlarged in the inset. "LP" indicates the position of the pipette for local perfusion of caged glutamate. Inset: maximum intensity projection of the spiny dendrite after z-alignment and deconvolution. The region of interest from which fluorescence was recorded is indicated by the line. The white cross shows the position of the uncaging laser beam. Scale bars: 20 µm (left) and 5 µm (right). Bottom: inward current (upper trace) and $[Na^+]_i$ signal (lower trace) induced by an uncaging flash for 200 ms (indicated by the grey bars). The grey line represents a monoexponential fit of the data trace. **B**, $[Na^+]_i$ signals in a spiny dendrite (recorded from the dashed area "B" in image in (**F**)) induced by glutamate uncaging (grey bars) in the control, during application of the glutamate receptors blockers AP5 and CNQX, and upon their washout. Accompanying inward currents are shown on the left. **C**, $[Na^+]_i$ signals in a spiny dendrite induced by uncaging for 200, 100 and 50 ms (grey bars). **D**, correlation between total charge of inward

currents and resulting change in $[Na^+]_i$. Data points represent single measurements taken from 14 experiments. Grey line represents a linear fit. **E**, Top: image of a dendrite with different regions of interest from which $[Na^+]_i$ signals shown below were recorded. The white cross shows the position of the uncaging laser beam. Scale bar: 5 µm. Bottom: $[Na^+]_i$ signals in 6 regions of interest induced by glutamate uncaging for 200 ms (grey bar). "s" indicates a single spine, "d" an adjacent dendrite. **F**, Top: image of several close dendrites. Lines indicate different regions of interest from which $[Na^+]_i$ signals shown below were recorded. Dashed line indicates the region on interest from which measurements depicted in **B** were taken. The white cross shows the position of the uncaging laser beam. Scale bar: 5 µm. Bottom: $[Na^+]_i$ signals in 3 dendritic sections induced by glutamate uncaging for 200 ms (grey bar).

Fig. 3: $[Na^+]_i$ signals evoked by local electroporation. **A**, Top: maximum intensity projection of a spiny dendrite after z-alignment and deconvolution. The dotted line illustrates the region of interest from which the measurement shown below was recorded. „EP" schematically indicates the position of the pipette for local electroporation. Scale bar: 5 µm. Bottom: inward current (upper trace, stimulus artifact partially blanked) and $[Na^+]_i$ signal (center and bottom trace) induced by local electroporation (indicated by black triangle). The grey line represents a monoexponential fit of the recovery phase. The box indicates the section shown at enlarged time scale underneath. **B,** Top: maximum intensity projection of a spiny dendrite after z-alignment and deconvolution. The dotted line illustrates the region of interest from which the measurements shown below were recorded. „EP" shows the position of the pipette for local electroporation with d1-d3 indicating different distances of its tip from the dendrite. Scale bar: 5 µm. Bottom: $[Na^+]_i$ signals induced by three subsequent electroporation pulses of 5 ms, delivered at increasing distance of the pipette tip to the dendrite as indicated. Grey lines represent monoexponential fits of

1390 the recovery phases. Inward currents in response to the stimulation are shown on the left
1391 (stimulus artifact partially blanked). **C**, Top: Relationship between the total charge of
1392 somatic inward current and the distance of the electroporation pipette from the dendrite
1393 retrieved from four different experiments. Bottom: Relationship between change in $[Na^+]_i$
1394 and pipette distance. Data points obtained in one experiment are connected, arrowheads
1395 indicate the direction of pipette movement. **D**, correlation between total charge of somatic
1396 inward current and change in $[Na^+]_i$. Data taken from 27 experiments, grey line represents
1397 a linear fit.
1398
1399 **Fig. 4:** Diffusion of sodium along dendrites. **A**, maximal intensity projection of a spiny
1400 dendrite after z-alignment and deconvolution. The dotted lines illustrate the regions of
1401 interest from which the measurements shown in B were recorded, crosses mark their center
1402 of mass taken as anchor point to measure distances. „EP“ schematically indicates the
1403 position of the pipette for local electroporation. Scale bar: 5 µm. **B**, $[Na^+]_i$ signals recorded
1404 in regions 1-3 in response to three consecutive electroporation stimuli. Black triangles and
1405 vertical dotted line indicate time point of electroporation, grey triangles indicate
1406 fluorescence maximum according to distinct peak or, if necessary, curve tracing of
1407 polynomial fits. Respective inward currents are depicted on the right (stimulation artifacts
1408 blanked). **C**, diffusion constant calculated from one dimensional diffusion equation. Black
1409 squares represent single data points; grey box shows average values, whiskers represent
1410 S.E.M. (n=19).
1411
1412 **Fig. 5:** Diffusion of sodium from dendrites into spines. **A**, Top: deconvolved maximum
1413 intensity z-projection of a spiny dendrite. “EP” indicates the position of the electroporation
1414 pipette. Grey lines indicate the regions of interest from which fluorescence measurements
1415 shown below were taken. The box indicates the area shown enlarged in the inset.

Arrowhead points to a long-neck spine ("1"). Scale bars: 5 μm, 2 μm (inset). Bottom: $[Na^+]_i$ signals recorded in regions 1 and 2 in response to an electroporation (indicated by black triangle and vertical dotted line). Single spine trace was low-pass filtered at 2 Hz. **C**, Averaged sodium signals in response to electroporation (black triangle) taken from 14 long-neck spines (grey trace) and adjacent dendrites (black trace). Lines represent monoexponential fits of the recovery phases, box delineates the phase shown at enlarged time scale below. Bottom: Rising phase of averaged $[Na^+]_i$ signals in dendrites (black) and spines (grey), depicted as means ± S.E.M. Lines represent linear fits of the 10-90% rising phase. **C** and **D**: same illustration as in (A) and (B) for short-neck spines and adjacent dendrites.

Fig. 6: Synaptically induced $[Na^+]_i$ signals in dendrites and spines. **A**, Top: maximal intensity projection image of a CA1 pyramidal cell filled with SBFI through a patch pipette (PP). The box indicates the area shown enlarged in the inset. Inset: spiny dendrite with regions of interest from which fluorescence measurements shown in B were taken. Scale bars: 40 μm, 2 μm (inset). **B,** $[Na^+]_i$ signals recorded in two single spines (s1, s3) and adjacent regions (d2, d4) in response to synaptic stimulation (50 Hz/200 ms, indicated by open triangle and vertical dotted line). **C**, Left: Averaged sodium signals in response to synaptic stimulation (open triangle) taken from 16 long spines (grey trace) and their adjacent dendrites (black trace). Lines represent best fits for the recovery phases, box delineates the phase shown at enlarged time scale below. Bottom: Rising phase of averaged $[Na^+]_i$ signals in dendrites (black) and long spines (grey), depicted as means ± S.E.M. Bar indicates the stimulation period. Right: same illustration as depicted on the left for short spines (average of 22) and adjacent dendrites.

Fig. 7: Rise time of synaptically-induced $[Na^+]_i$ signals. **A**, maximal intensity projection image of a CA1 pyramidal cell filled with SBFI through a patch pipette (PP). Scale bar: 40 µm. **B**, magnified high power maximum intensity projection image of the dashed box depicted in **A**. Green line indicates position of the line of interest chosen for line scan measurements shown in (**C**) and (**D**), with the green cross indicating its starting point. Scale bar: 2 µm. **C**, Color-coded image of synaptically-induced changes in SBFI fluorescence in the dendrite and spine, recorded at 700 Hz. The black line underneath shows the stimulation period (50 Hz/200 ms). Traces below depict the changes in SBFI fluorescence relative to baseline (both after a 50 Hz FFT). **D**, Top: Averaged changes in SBFI fluorescence in response to synaptic stimulation (indicated by the bars) taken from 12 long spines (grey trace) and their adjacent dendrites (black trace). Lines represent linear fits of the rising phase (10-90% interval). Bottom traces show the same for short spines (average of 12) and adjacent dendrites.

Fig. 8: Numerical modeling of Na^+ dynamics in spines and dendrites. **A**, Left: sodium signals in a long-neck spine (l_{neck}=1.4 µm) and its adjacent dendritic segment upon a Gaussian influx (dashed line, normalized) into the spine head, mimicking synaptic input onto this spine. NKA is present in dendrite and spine. Simulation of the sodium signal in the spine is shown for four different values of D_{Na}. The drawing depicts the experimental situation schematically. Left: Sodium signals in a short-neck spine (l_{neck}=0.1 µm) and parent dendrite (same influx, D_{Na}=160 µm²/s). **B,** Left: sodium signals in a long-neck (left) and a short-neck spine (right) as well as their adjacent dendritic segments upon a Gaussian influx placed in the dendritic segment, mimicking local electroporation. Drawing indicates electroporation site and simulated spino-dendritic segment (grey area). **C** and **D,** Same as in (A) and (B), but with NKA pumps additionally present in the spine neck.

Author contributions

C. Kleinhans: design of experiments, combined patch-clamp/imaging experiments, data analysis and interpretation, writing of the manuscript.

N. Gerkau: synaptic stimulation: combined patch-clamp/imaging, data analysis and interpretation, writing of the manuscript.

H. Schmidt: Modeling.

W. Karl Kafitz: design of experiments, data analysis and interpretation.

C. R. Rose: general design, analysis and interpretation of the study, writing of the paper.

All authors contributed to critical revision of the manuscript for intellectual content and final approval of version to be published.

References

Allbritton NL, Meyer T, Stryer L (1992) Range of messenger action of calcium ion and inositol 1,4,5-trisphosphate. Science 258:1812-1815.

Araya R, Eisenthal KB, Yuste R (2006a) Dendritic spines linearize the summation of excitatory potentials. Proc Natl Acad Sci U S A 103:18799-18804.

Araya R, Vogels TP, Yuste R (2014) Activity-dependent dendritic spine neck changes are correlated with synaptic strength. Proc Natl Acad Sci U S A 111:E2895-2904.

Araya R, Jiang J, Eisenthal KB, Yuste R (2006b) The spine neck filters membrane potentials. Proc Natl Acad Sci U S A 103:17961-17966.

Araya R, Nikolenko V, Eisenthal KB, Yuste R (2007) Sodium channels amplify spine potentials. Proc Natl Acad Sci U S A 104:12347-12352.

Arellano JI, Benavides-Piccione R, Defelipe J, Yuste R (2007) Ultrastructure of dendritic spines: correlation between synaptic and spine morphologies. Frontiers in neuroscience 1:131-143.

Azarias G, Kruusmagi M, Connor S, Akkuratov EE, Liu XL, Lyons D, Brismar H, Broberger C, Aperia A (2012) A specific and essential role for Na,K-ATPase alpha3 in neurons co-expressing alpha1 and alpha3. The Journal of biological chemistry.

Baranauskas G, David Y, Fleidervish IA (2013) Spatial mismatch between the Na+ flux and spike initiation in axon initial segment. Proc Natl Acad Sci U S A 110:4051-4056.

Bennay M, Langer J, Meier SD, Kafitz KW, Rose CR (2008) Sodium signals in cerebellar Purkinje neurons and Bergmann glial cells evoked by glutamatergic synaptic transmission. Glia 56:1138-1149.

Blom H, Ronnlund D, Scott L, Spicarova Z, Widengren J, Bondar A, Aperia A, Brismar H (2011) Spatial distribution of Na+-K+-ATPase in dendritic spines dissected by nanoscale superresolution STED microscopy. BMC neuroscience 12:16.

Bloodgood BL, Giessel AJ, Sabatini BL (2009) Biphasic synaptic Ca influx arising from compartmentalized electrical signals in dendritic spines. PLoS biology 7:e1000190.

Bywalez WG, Patirniche D, Rupprecht V, Stemmler M, Herz AV, Palfi D, Rozsa B, Egger V (2015) Local postsynaptic voltage-gated sodium channel activation in dendritic spines of olfactory bulb granule cells. Neuron 85:590-601.

David G, Barrett JN, Barrett EF (1997) Spatiotemporal gradients of intra-axonal [Na+] after transection and resealing in lizard peripheral myelinated axons. J Physiol 498 (Pt 2):295-307.

Denk W, Sugimori M, Llinas R (1995) Two types of calcium response limited to single spines in cerebellar Purkinje cells. Proc Natl Acad Sci U S A 92:8279-8282.

Despa S, Bers DM (2003) Na/K pump current and [na](I) in rabbit ventricular myocytes: local [na](I) depletion and na buffering. Biophys J 84:4157-4166.

Edwards FA, Konnerth A, Sakmann B, Takahashi T (1989) A thin slice preparation for patch clamp recordings from neurones of the mammalian central nervous system. Pflugers Arch 414:600-612.

Eilers J, Augustine GJ, Konnerth A (1995) Subthreshold synaptic Ca2+ signalling in fine dendrites and spines of cerebellar Purkinje neurons. Nature 373:155-158.
Fleidervish IA, Lasser-Ross N, Gutnick MJ, Ross WN (2010) Na+ imaging reveals little difference in action potential-evoked Na+ influx between axon and soma. Nat Neurosci 13:852-860.
Grunditz A, Holbro N, Tian L, Zuo Y, Oertner TG (2008) Spine neck plasticity controls postsynaptic calcium signals through electrical compartmentalization. J Neurosci 28:13457-13466.
Gu L, Kleiber S, Schmid L, Nebeling F, Chamoun M, Steffen J, Wagner J, Fuhrmann M (2014) Long-term in vivo imaging of dendritic spines in the hippocampus reveals structural plasticity. J Neurosci 34:13948-13953.
Harnett MT, Makara JK, Spruston N, Kath WL, Magee JC (2012) Synaptic amplification by dendritic spines enhances input cooperativity. Nature 491:599-602.
Hayashi Y, Majewska AK (2005) Dendritic spine geometry: functional implication and regulation. Neuron 46:529-532.
Helmchen F, Tank DW (2005) A single-compartment model of calcium dynamics in nerve terminals and dendrites. In: Imaging neurons: A laboratory manual (Yuste R KA, ed), pp 265-275. New York: Cold Spring Harbor Laboratory Press.
Holcman D, Yuste R (2015) The new nanophysiology: regulation of ionic flow in neuronal subcompartments. Nature reviews Neuroscience 16:685-692.
Jaffe DB, Johnston D, Lasser-Ross N, Lisman JE, Miyakawa H, Ross WN (1992) The spread of Na+ spikes determines the pattern of dendritic Ca2+ entry into hippocampal neurons. Nature 357:244-246.
Karus C, Ziemens D, Rose CR (2015a) Lactate rescues neuronal sodium homeostasis during impaired energy metabolism. Channels (Austin) 9:200-208.
Karus C, Mondragao MA, Ziemens D, Rose CR (2015b) Astrocytes restrict discharge duration and neuronal sodium loads during recurrent network activity. Glia 63:936-957.
Kelly T, Rose CR (2010) Ammonium influx pathways into astrocytes and neurones of hippocampal slices. J Neurochem 115:1123-1136.
Kleinhans C, Kafitz KW, Rose CR (2014) Multi-photon intracellular sodium imaging combined with UV-mediated focal uncaging of glutamate in CA1 pyramidal neurons. Journal of visualized experiments : JoVE:e52038.
Knopfel T, Anchisi D, Alojado ME, Tempia F, Strata P (2000) Elevation of intradendritic sodium concentration mediated by synaptic activation of metabotropic glutamate receptors in cerebellar Purkinje cells. Eur J Neurosci 12:2199-2204.
Koch C, Zador A (1993) The function of dendritic spines: devices subserving biochemical rather than electrical compartmentalization. J Neurosci 13:413-422.
Koester HJ, Sakmann B (1998) Calcium dynamics in single spines during coincident pre- and postsynaptic activity depend on relative timing of back-propagating action potentials and subthreshold excitatory postsynaptic potentials. Proc Natl Acad Sci U S A 95:9596-9601.
Kole MH, Ilschner SU, Kampa BM, Williams SR, Ruben PC, Stuart GJ (2008) Action potential generation requires a high sodium channel density in the axon initial segment. Nat Neurosci 11:178-186.
Korkotian E, Holcman D, Segal M (2004) Dynamic regulation of spine-dendrite coupling in cultured hippocampal neurons. Eur J Neurosci 20:2649-2663.
Kushmerick MJ, Podolsky RJ (1969) Ionic mobility in muscle cells. Science 166:1297-1298.
Langer J, Stephan J, Theis M, Rose CR (2012) Gap junctions mediate intercellular spread of sodium between hippocampal astrocytes in situ. Glia 60:239-252.
Lasser-Ross N, Ross WN (1992) Imaging voltage and synaptically activated sodium transients in cerebellar Purkinje cells. Proc Biol Sci 247:35-39.
Liebmann T, Blom H, Aperia A, Brismar H (2013) Nanoscale elucidation of Na,K-ATPase isoforms in dendritic spines. Optical Nanoscopy 2:6.
Lobo VM (1993) Mutual diffusion coefficients in aqueous electrolyte solutions. Pure & Appl Chem 65:2613-2640.
Meier SD, Kovalchuk Y, Rose CR (2006) Properties of the new fluorescent Na+ indicator CoroNa Green: comparison with SBFI and confocal Na+ imaging. J Neurosci Methods 155:251-259.
Nagerl UV, Willig KI, Hein B, Hell SW, Bonhoeffer T (2008) Live-cell imaging of dendritic spines by STED microscopy. Proc Natl Acad Sci U S A 105:18982-18987.
Noguchi J, Matsuzaki M, Ellis-Davies GC, Kasai H (2005) Spine-neck geometry determines NMDA receptor-dependent Ca2+ signaling in dendrites. Neuron 46:609-622.
Popov S, Poo MM (1992) Diffusional transport of macromolecules in developing nerve processes. J Neurosci 12:77-85.
Rose CR, Ransom BR (1997) Regulation of intracellular sodium in cultured rat hippocampal neurones. J Physiol 499 (Pt 3):573-587.
Rose CR, Konnerth A (2001) NMDA receptor-mediated Na+ signals in spines and dendrites. J Neurosci 21:4207-4214.
Rose CR, Kovalchuk Y, Eilers J, Konnerth A (1999) Two-photon Na+ imaging in spines and fine dendrites of central neurons. Pflugers Arch 439:201-207.
Sabatini BL, Oertner TG, Svoboda K (2002) The life cycle of Ca(2+) ions in dendritic spines. Neuron 33:439-452.
Sala C, Segal M (2014) Dendritic spines: the locus of structural and functional plasticity. Physiological reviews 94:141-188.
Santamaria F, Wils S, De Schutter E, Augustine GJ (2011) The diffusional properties of dendrites depend on the density of dendritic spines. Eur J Neurosci 34:561-568.
Schiller J, Schiller Y, Clapham DE (1998) NMDA receptors amplify calcium influx into dendritic spines during associative pre- and postsynaptic activation. Nat Neurosci 1:114-118.
Schmidt H, Eilers J (2009) Spine neck geometry determines spino-dendritic cross-talk in the presence of mobile endogenous calcium binding proteins. J Comput Neurosci 27:229-243.
Schmidt H, Kunerth S, Wilms C, Strotmann R, Eilers J (2007) Spino-dendritic cross-talk in rodent Purkinje neurons mediated by endogenous Ca2+-binding proteins. J Physiol 581:619-629.
Segal M, Vlachos A, Korkotian E (2010) The spine apparatus, synaptopodin, and dendritic spine plasticity. The Neuroscientist : a review journal bringing neurobiology, neurology and psychiatry 16:125-131.
Spacek J, Harris KM (1997) Three-dimensional organization of smooth endoplasmic reticulum in hippocampal CA1 dendrites and dendritic spines of the immature and mature rat. J Neurosci 17:190-203.
Takasaki K, Sabatini BL (2014) Super-resolution 2-photon microscopy reveals that the morphology of each dendritic spine correlates with diffusive but not synaptic properties. Frontiers in neuroanatomy 8:29.

Takasaki KT, Ding JB, Sabatini BL (2013) Live-cell superresolution imaging by pulsed STED two-photon excitation microscopy. Biophys J 104:770-777.

Tønnesen J, Katona G, Rozsa B, Nagerl UV (2014) Spine neck plasticity regulates compartmentalization of synapses. Nat Neurosci 17:678-685.

Tsay D, Yuste R (2004) On the electrical function of dendritic spines. Trends in neurosciences 27:77-83.

Wijetunge LS, Angibaud J, Frick A, Kind PC, Nagerl UV (2014) Stimulated emission depletion (STED) microscopy reveals nanoscale defects in the developmental trajectory of dendritic spine morphogenesis in a mouse model of fragile X syndrome. J Neurosci 34:6405-6412.

Yuste R, Denk W (1995) Dendritic spines as basic functional units of neuronal integration. Nature 375:682-684.

Yuste R, Majewska A, Holthoff K (2000) From form to function: calcium compartmentalization in dendritic spines. Nat Neurosci 3:653-659.

Zhai S, Ark ED, Parra-Bueno P, Yasuda R (2013) Long-distance integration of nuclear ERK signaling triggered by activation of a few dendritic spines. Science 342:1107-1111.

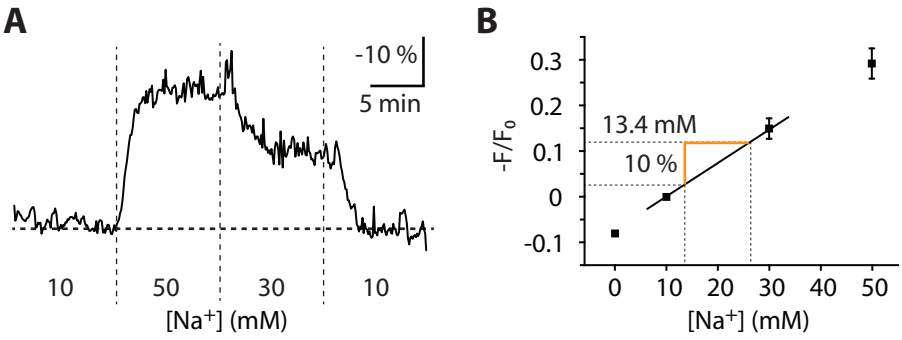

Fig. 1: Kleinhans et al.

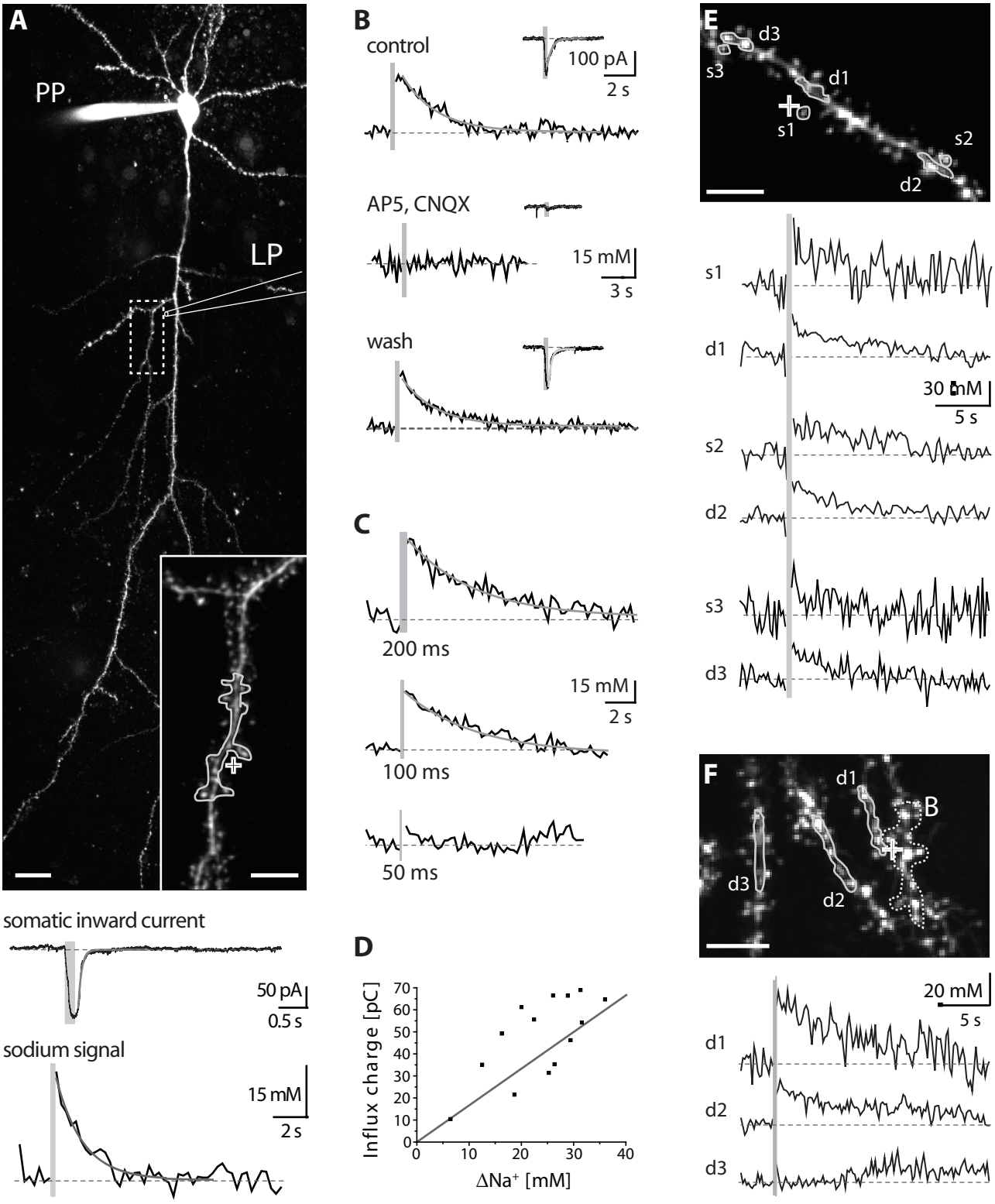

Fig. 2: Kleinhans et al.

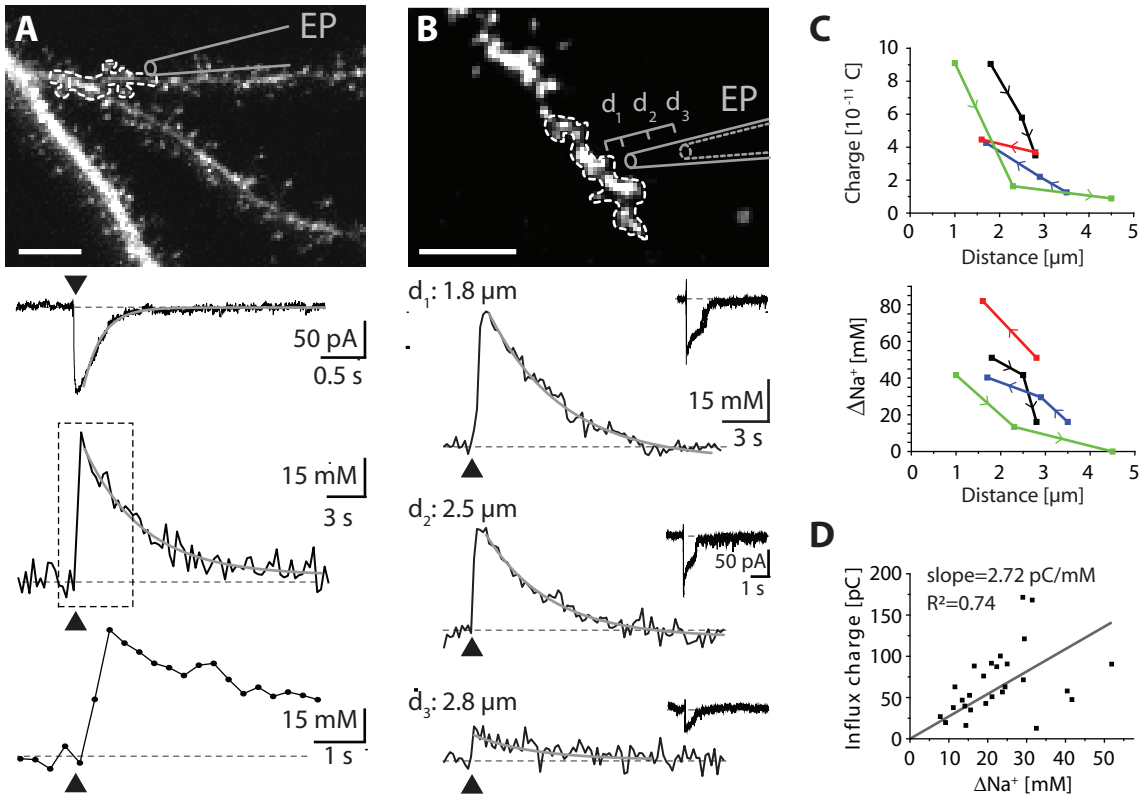

Fig. 3: Kleinhans et al.

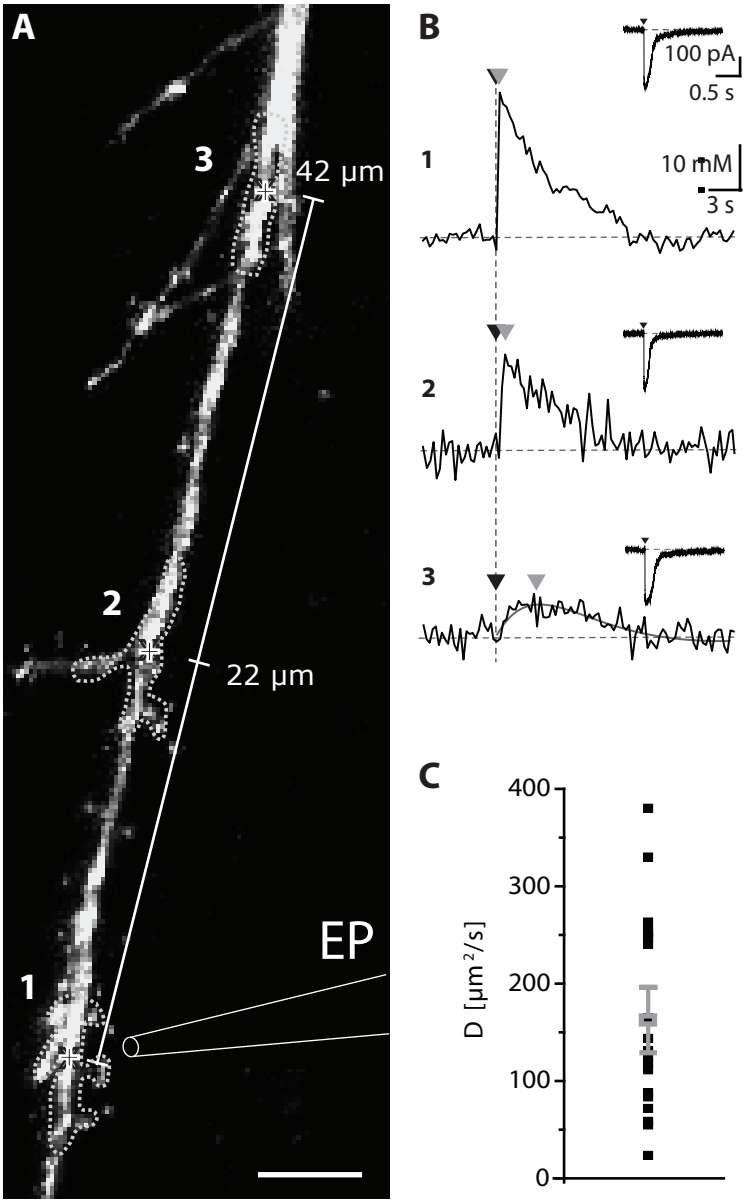

Fig. 4: Kleinhans et al.

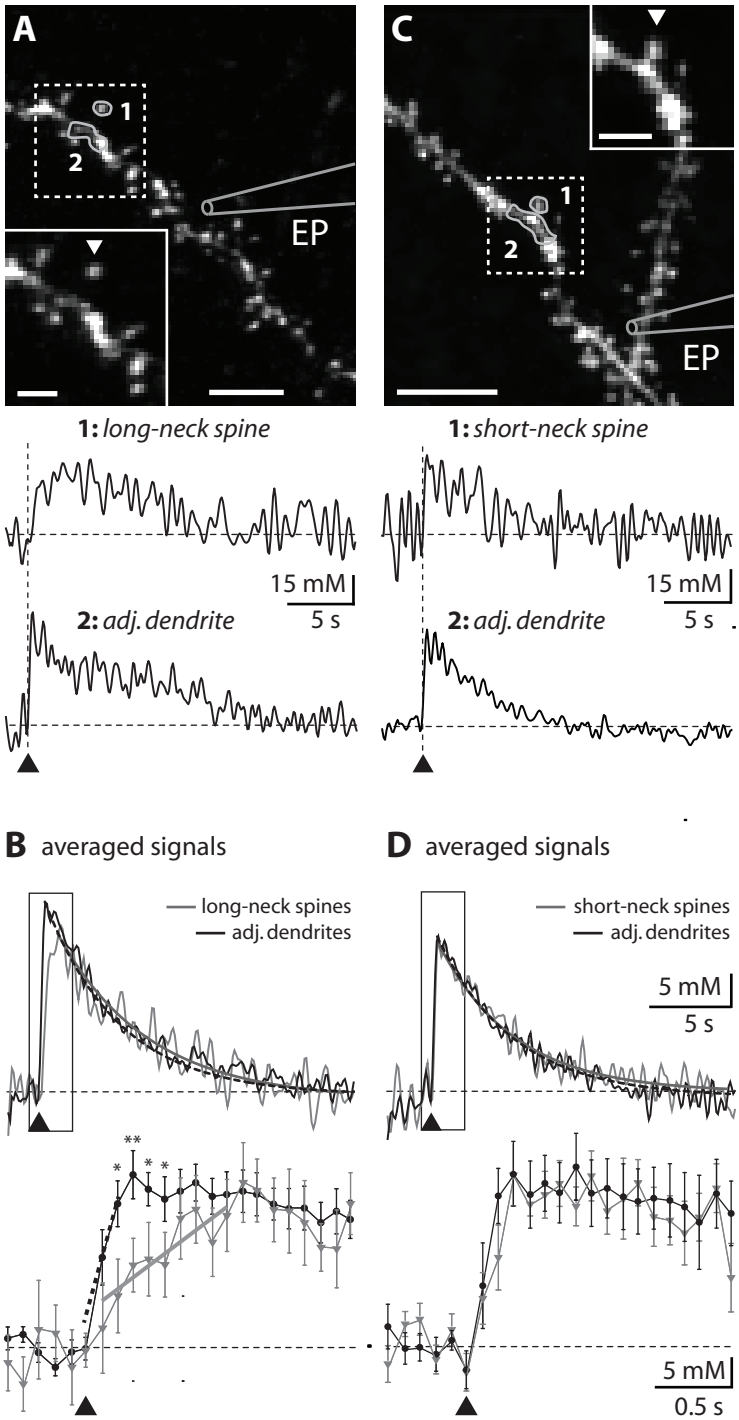

Fig. 5: Kleinhans et al.

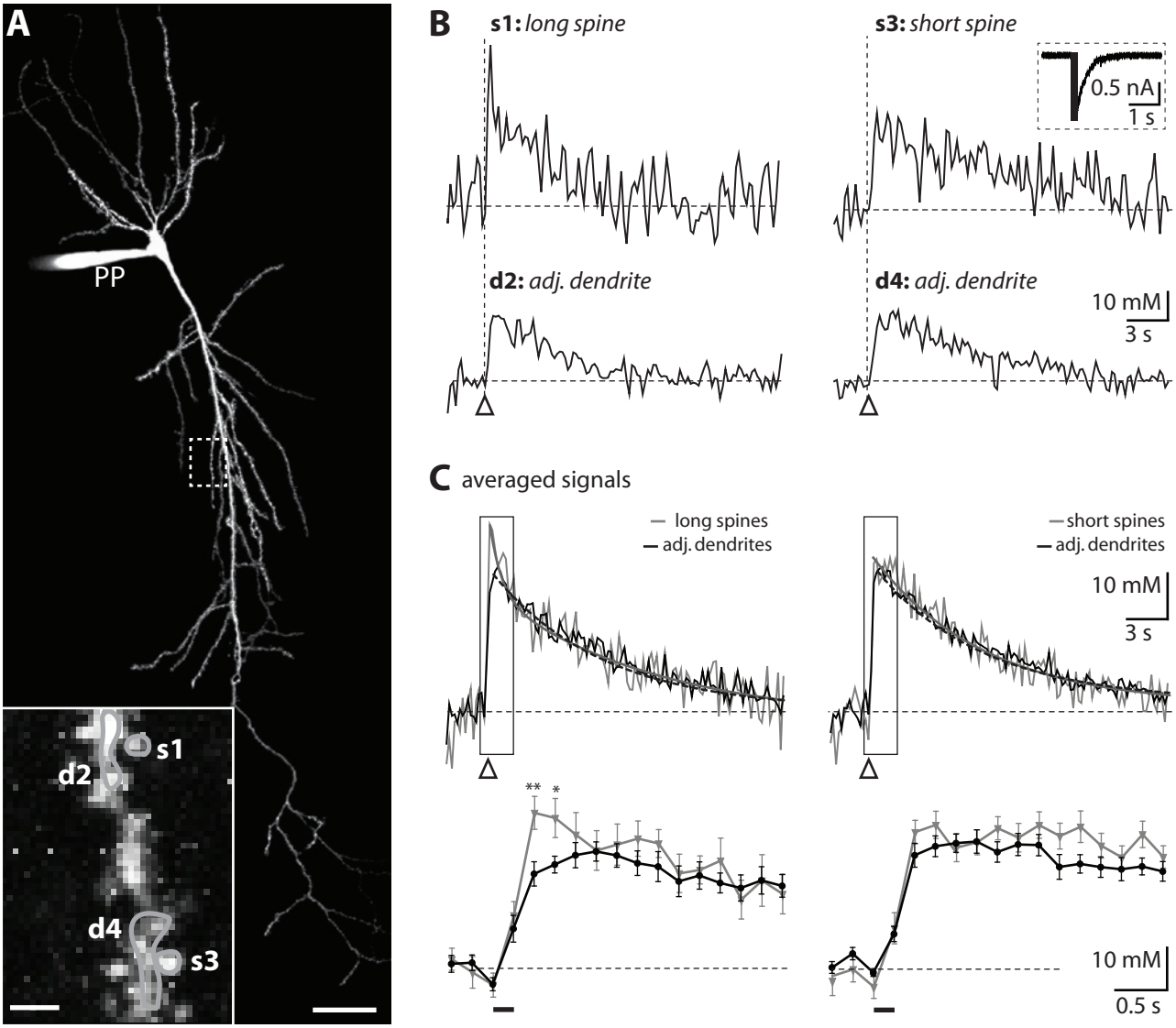

Fig. 6: Kleinhans et al.

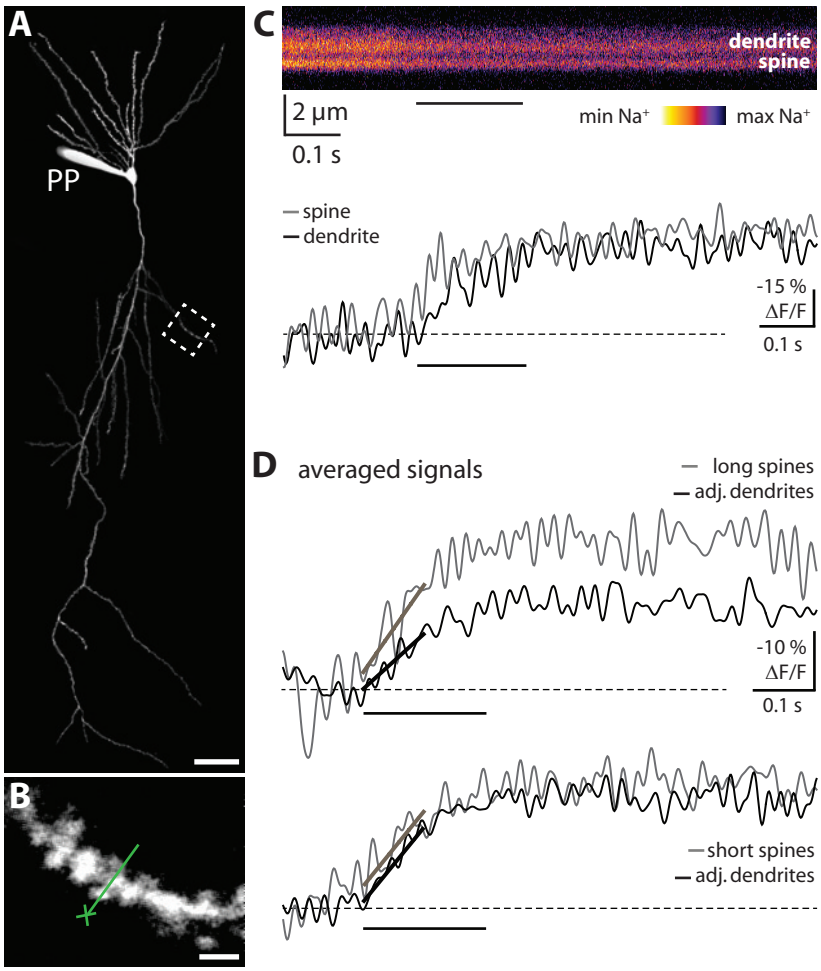

Fig. 7: Kleinhans et al.

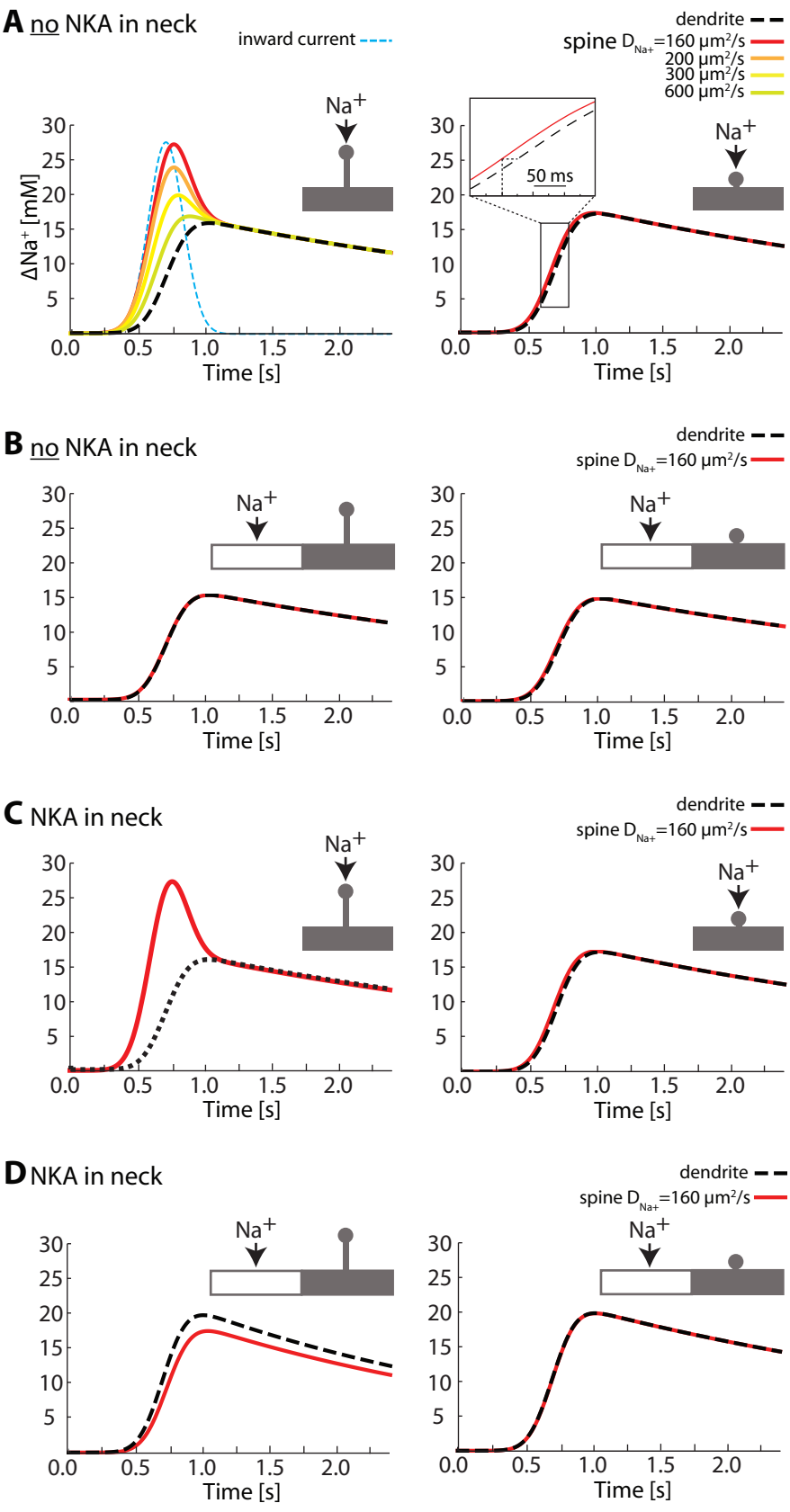

Fig. 8: Kleinhans et al.

8.2 Multi-photon Intracellular Sodium Imaging Combined with UV-mediated Focal Uncaging of Glutamate in CA1 Pyramidal Neurons

Status: Veröffentlicht am 8.10.2014 im „Journal of Visualized Experiments“ (freier Zugriff/open access).

Persönlicher Beitrag: 70%. Ich habe alle Experimente sowie die Analyse der Daten durchgeführt. Zudem war ich an der Erstellung des experimentellen Konzepts und der technischen Umsetzung, der Interpretation der Daten, der Verfassung des Manuskripts sowie der Abbildungen beteiligt.

Video Article

Multi-photon Intracellular Sodium Imaging Combined with UV-mediated Focal Uncaging of Glutamate in CA1 Pyramidal Neurons

Christian Kleinhans*[1], Karl W. Kafitz*[1], Christine R. Rose[1]

[1]Institute of Neurobiology, Heinrich Heine University Düsseldorf

*These authors contributed equally

Correspondence to: Christine R. Rose at rose@uni-duesseldorf.de

URL: http://www.jove.com/video/52038
DOI: doi:10.3791/52038

Keywords: Neuroscience, Issue 92, Neurosciences, two-photon microscopy, patch-clamp, UV-flash photolysis, mouse, hippocampus, caged compounds, glutamate, brain slice, dendrite, sodium signals

Date Published: 10/8/2014

Citation: Kleinhans, C., Kafitz, K.W., Rose, C.R. Multi-photon Intracellular Sodium Imaging Combined with UV-mediated Focal Uncaging of Glutamate in CA1 Pyramidal Neurons. *J. Vis. Exp.* (92), e52038, doi:10.3791/52038 (2014).

Abstract

Multi-photon fluorescence microscopy has enabled the analysis of morphological and physiological parameters of brain cells in the intact tissue with high spatial and temporal resolution. Combined with electrophysiology, it is widely used to study activity-related calcium signals in small subcellular compartments such as dendrites and dendritic spines. In addition to calcium transients, synaptic activity also induces postsynaptic sodium signals, the properties of which are only marginally understood. Here, we describe a method for combined whole-cell patch-clamp and multi-photon sodium imaging in cellular micro domains of central neurons. Furthermore, we introduce a modified procedure for ultra-violet (UV)-light-induced uncaging of glutamate, which allows reliable and focal activation of glutamate receptors in the tissue. To this end, whole-cell recordings were performed on *Cornu Ammonis* subdivision 1 (CA1) pyramidal neurons in acute tissue slices of the mouse hippocampus. Neurons were filled with the sodium-sensitive fluorescent dye SBFI through the patch-pipette, and multi-photon excitation of SBFI enabled the visualization of dendrites and adjacent spines. To establish UV-induced focal uncaging, several parameters including light intensity, volume affected by the UV uncaging beam, positioning of the beam as well as concentration of the caged compound were tested and optimized. Our results show that local perfusion with caged glutamate (MNI-Glutamate) and its focal UV-uncaging result in inward currents and sodium transients in dendrites and spines. Time course and amplitude of both inward currents and sodium signals correlate with the duration of the uncaging pulse. Furthermore, our results show that intracellular sodium signals are blocked in the presence of blockers for ionotropic glutamate receptors, demonstrating that they are mediated by sodium influx though this pathway. In summary, our method provides a reliable tool for the investigation of intracellular sodium signals induced by focal receptor activation in intact brain tissue.

Video Link

The video component of this article can be found at http://www.jove.com/video/52038/

Introduction

Recent improvements in light microscopic techniques such as multi-photon microscopy have enabled the study of morphological and physiological parameters of brain cells in the intact tissue with high spatial and temporal resolution. Combined with electrophysiology, these techniques are now widely used to analyze activity-related electrical signals on neurons as well as concomitant calcium signals in small subcellular compartments, namely in fine dendrites and dendritic spines. In addition to calcium transients, synaptic activity also induces sodium signals in dendrites and spines, the properties of which are largely unexplored. Such signals can be analyzed by two-photon imaging of intracellular sodium ($[Na^+]_i$) which enables the on-line measurement of $[Na^+]_i$ transients for prolonged periods without significant dye bleaching or photo-damage[1,2].

For imaging of $[Na^+]_i$, only a few chemical indicator dyes are available, *e.g.* CoroNa Green or Asante Natrium Green[3,4]. The most commonly used fluorescent probe for Na^+ imaging is sodium-binding benzofuran isophthalate (SBFI). It is a ratiometric, UV-excited dye similar to the well-known calcium-sensitive dye fura-2 and has been employed for conventional Na^+ imaging in many cell types (*e.g.*[5,6]). There are different possibilities of exciting the dye and collecting its fluorescence. If high temporal resolution (*i.e.* a high imaging frame rate) is required in combination with spatial information, SBFI can be excited with a xenon arc lamp or a high power light-emitting diode (LED) device and its emission detected with a high speed charge-coupled device (CCD) camera[7,8]. For maximal spatial resolution deep in the tissue, multi-photon laser scanning microscopy is the method of choice[9]. The relatively low quantum efficiency of SBFI necessitates relatively high dye concentrations (0.5 - 2 mM), and direct loading of the membrane-impermeable form of SBFI via a sharp microelectrode[10] or patch pipette[1].

Using SBFI, earlier work performed in acute tissue slices of the rodent hippocampus demonstrated activity-related sodium transients in dendrites and spines of CA1 pyramidal neurons which are mainly caused by influx of sodium through ionotropic NMDA receptors[1,2]. For the study of the properties of such local sodium signals in more detail, specific activation of postsynaptic receptors by application of receptor agonists is a well-suited method of choice. To mimic presynaptic activity and transmitter release, application should be relatively brief and focused to enable local stimulation. This, however, proves to be quite challenging in the intact tissue. Local pressure application of receptor agonists using a fine-tipped

pipette enables very focal application, but hosts the potential risk for producing movement of the structure of interest (*e.g.* such as a dendrite or dendritic spines), and thus hinders high-resolution imaging. The suitability of iontophoresis of neuro-active substances depends on their electrical properties and high current amplitudes may produce cellular artifacts as well.

One way to circumvent these obstacles is the employment of photo-activated compounds and their flash photolysis. Basically, two different principles are used for photo-activation of caged substances: I) Wide-field flash photolysis[11] and II) focal uncaging employing scanning modules in combination with lasers[12]. While wide-field flash photolysis is used to activate larger regions of interest, *e.g.* an entire cell, focal uncaging is employed to specifically stimulate small cellular compartments. In the present study we demonstrate a procedure for whole-cell patch-clamp and multi-photon sodium imaging in dendrites and spines of central neurons, combined with a modified procedure for UV-light-induced uncaging of glutamate, which allows reliable and focal activation of glutamate receptors in the tissue.

Protocol

This study was carried out in strict accordance with the institutional guidelines of the Heinrich Heine University Düsseldorf, Germany, as well as the European Community Council Directive (86/609/EEC). All experiments were communicated to and approved by the Animal Welfare Office at the Animal Care and Use Facility of the Heinrich Heine University Düsseldorf, Germany (institutional act number: O52/05). In accordance with the German Animal Welfare Act (Tierschutzgesetz, Articles 4 and 7), no formal additional approval for the postmortem removal of brain tissue was necessary.

For generation of acute slices, mice were anaesthetized with CO_2 and quickly decapitated (following the recommendation of the European Commission published in: Euthanasia of experimental animals, Luxembourg: Office for Official Publications of the European Communities, 1997; ISBN 92–827-9694-9).

1. Preparation of Solutions

1. Prepare artificial cerebrospinal fluid (ACSF) for dissection containing (in mM): 125 NaCl, 2.5 KCl, 0.5 $CaCl_2$, 6 $MgCl_2$, 1.25 NaH_2PO_4, 26 $NaHCO_3$, and 20 glucose, bubbled with 95% O_2 and 5% CO_2, resulting in a pH of 7.4.
2. Prepare ACSF for experiments containing (in mM): 125 NaCl, 2.5 KCl, 2 $CaCl_2$, 1 $MgCl_2$, 1.25 NaH_2PO_4, 26 $NaHCO_3$, and 20 glucose, bubbled with 95% O_2 and 5% CO2, resulting in a pH of 7.4.
3. Prepare intracellular solution (ICS) containing (in mM): 150 $KMeSO_3$, 12.5 hydroxy ethyl piperazine ethane sulfonic acid (HEPES), 40 KCl, 5 NaCl, 1.25 ethylene glycol tetraacetic acid (EGTA), 5 Mg-ATP, 0.5 Na-GTP. Adjust pH to 7.3. Store aliquots of 1 ml at -20 °C.
4. Dilute sodium-binding benzofuran isophthalate (SBFI)-salt in double-distilled water and prepare aliquots of 5 µl of a 10 mM stock solution.
5. Thaw ICS and add SBFI stock solution at a final concentration of 1 mM. Vortex and micro-filtrate (0.22 µm). Keep at 4 °C until used in experiment. Do not refreeze and only use for one day.
6. Prepare MNI glutamate stock solution of 50 mM by dissolving the compound in double-distilled water. Dilute MNI glutamate stock solution to a final concentration of 5 mM in normal ACSF. Keep at 4 °C until used in experiment. Do not refreeze and only use for one day. Store aliquots, which are not immediately used in the experiment, at -20 °C.

2. Dissection of Tissue

NOTE: The preparation of acute hippocampal slices of the rodent brain was described in detail earlier[13,14]. In brief, the following protocol was employed in the present study.

1. After decapitation, rapidly remove the brain from the skull.
2. Immediately place the brain in a petri dish with ice-cold dissection ACSF and dissect a hemisphere by performing a sagittal cut along the midline.
3. Perform a second cut in the desired orientation as a blocking surface and attach this to the cutting stage of a vibratome with superglue.
4. Take cutting chamber and cooling element (both kept at -20 °C) of the vibratome out of the freezer and place cutting stage with brain section in the chamber. Then put cooling element in the chamber and submerge tissue in ice-cold dissection ACSF. To stabilize the preparation, one may want to counter the tissue block with agar gel.
5. Cut 250 µm thick, parasagittal slices of the hippocampus with the vibratome. Ensure that all ACS fluids are bubbled at all times.
6. After slicing, keep tissue on a mesh in a beaker with the normal ACSF and incubate at 34 °C for 30 min. Then keep at room temperature.

3. Preparation of Hardware

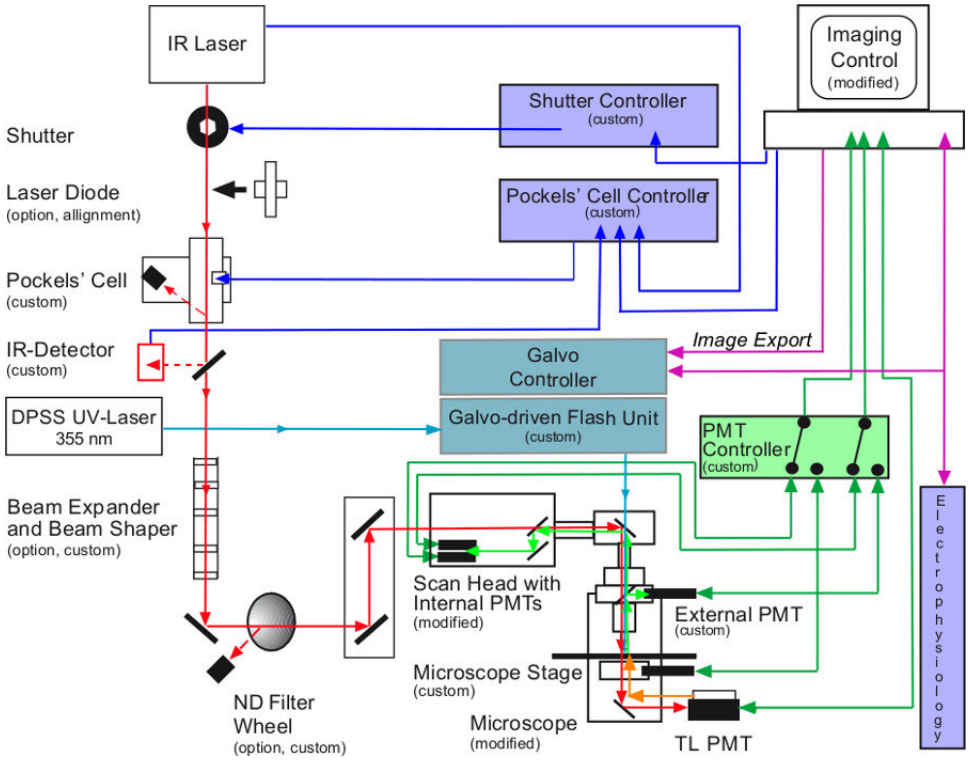

Figure 1. Scheme showing light paths and experimental control of the rig consisting of multi-photon imaging, laser-scanning UV flash photolysis, and electrophysiology. The multi-photon beam (red) is produced by a pulsed, tunable infrared (IR) laser (TiSa). It passes a mechanical shutter, a Pockels' cell, and the IR detector (detection of beam intensity), all of which enable control of the laser power and its administration duration. The flip-in/flip-out optional laser diode is employed for basic alignment of the laser beam. The beam expander may be used in combination with objectives with an extremely wide back-focal plane. The remote-controlled ND filter wheel may be used in addition or instead of the Pockels' cell to control laser beam power. After passing the scan head, the pulsed IR-light is guided to the specimen. Emitted fluorescence light (light green) is collected either by the external or the internal photomultiplier detectors (PMTs). The external detectors are fully synchronized with the internal PMTs via a high frequency switch (PMT controller). The uncaging beam (light blue) is produced by a UV solid-state laser (DPSS UV-Laser). It is then directed to the galvo-driven scanning unit at the top-back of the epi-fluorescence condenser by a light guide. The precise positioning (chromatic aberration between imaging and uncaging beam) of the uncaging spot or area is enabled by the image export from the imaging software. The timing management for synchronizing the imaging, the electrophysiology, and the flash photolysis is electronically controlled. The transillumination detector (TL-PMT) is of need for documentation of the positioning of the pipettes within the tissue. The control units and software of the imaging system, which has been modified, is used to control and synchronize all other devices needed to run the system. System components labeled as "custom" were designed and build/adapted by the authors. Some components were adapted to meet the requirements of the custom-build multi-photon system and are labeled as "modified". Please click here to view a larger version of this figure.

1. Switch on components of the multi-photon system. Test and adjust infrared laser beam alignment.
    1. Control beam positioning by flipping in the centering prism instead of an objective. If the beam is dislocated, re-adjust it by the mirrors in the periscope. Note that the centering plane of the prism must be at the same level as the back focal plane of the objective while imaging.
    2. Switch on the spectrometer and check for the multi-photon characteristics of the beam.
    3. Set parameters of the imaging software to the following values: Choose a frame size of 512 x 512 pixels for overview images of the cell (smaller clip boxes with a zoom factor of 2.5 for high frame rate and high spatial resolution, respectively). Set imaging speed to fast mode and scan mode to XYT. Z-stepping should be 1 µm for overview stacks and 0.2 µm for detailed stacks to match spatial sampling requirements for deconvolution performed later.

2. Adjust multi-photon laser beam (790 nm) intensity by altering settings of the Pockels' cell (final power under the objective: ≈ 14 - 16 µW) and the photo-multipliers (PMTs).
3. Switch on and calibrate uncaging system by placing a fluorescent sample slide under the objective lens.
    1. Using the binoculars, adjust the focus of the UV optics and spatially limit the UV laser spot to a size of 2 µm in diameter at maximum by employing the focusing unit at the UGA scan head.
    2. Start the calibration routine of the uncaging unit control software.

1. Set the UV laser to several points within its scan range, while the fluorescence is captured with a CCD camera. By clicking on the UV laser spot at each point, adjust the positioning of the galvanic scan mirrors to correspond to a certain coordinate in the software.

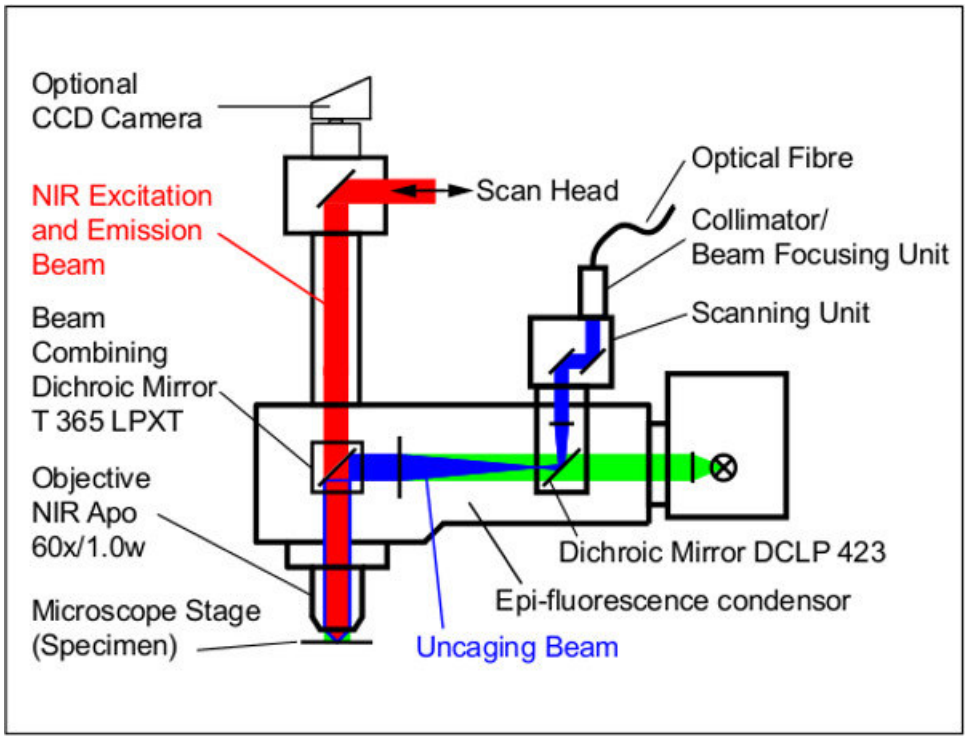

Figure 2. Detailed scheme illustrating the characteristics ofexcitation, emission and uncaging beam paths. The IR excitation beam (red) passes the beam combining dichroic mirror at the level to the filer turret in the epi-fluorescence condenser of the microscope and the objective to reach the specimen. The uncaging beam (blue) is delivered via a quartz optical light fiber to the collimation and beam focusing unit and then subsequently guided to the scanning mirrors in the scanning unit, passes a dichroic mirror to the beam combining dichroic mirror. Here it is combined with the excitation scanning beam. The emitted light from the specimen follows the path of the excitation scanning beam path in the opposite orientation towards the imaging scan head. The camera is used for visual control of the patch pipette and for positioning of the uncaging beam in combination with the confocal laser scanning microscope (not shown). The green light path represents an optional epi-fluorescence illumination which may be of use with other applications.

3. 2. 2. Use the flash photolysis system in the spot mode to gain focal applications. Ensure that the focal adjustment of the uncaging beam (average power underneath the objective: 0.55 mW) results in a spot size of 1.5 µm in diameter (xy extension) as revealed at a fluorescent slide positioned at a z-level that corresponds to that of a tissue slice (not shown).

3. The accurate positioning of the uncaging spot is achieved by the import of an image of the imaging system via a network connection between uncaging- and imaging-computers.
   1. Using a screen grabber software, continuously read out the frames of the imaging software (instead of the camera feed) and adjust the imaging and uncaging frames congruently. Export every 10^{th} frame from the imaging software as a reference image into the flash unit to ensure proper adjustment during the entire experiment.

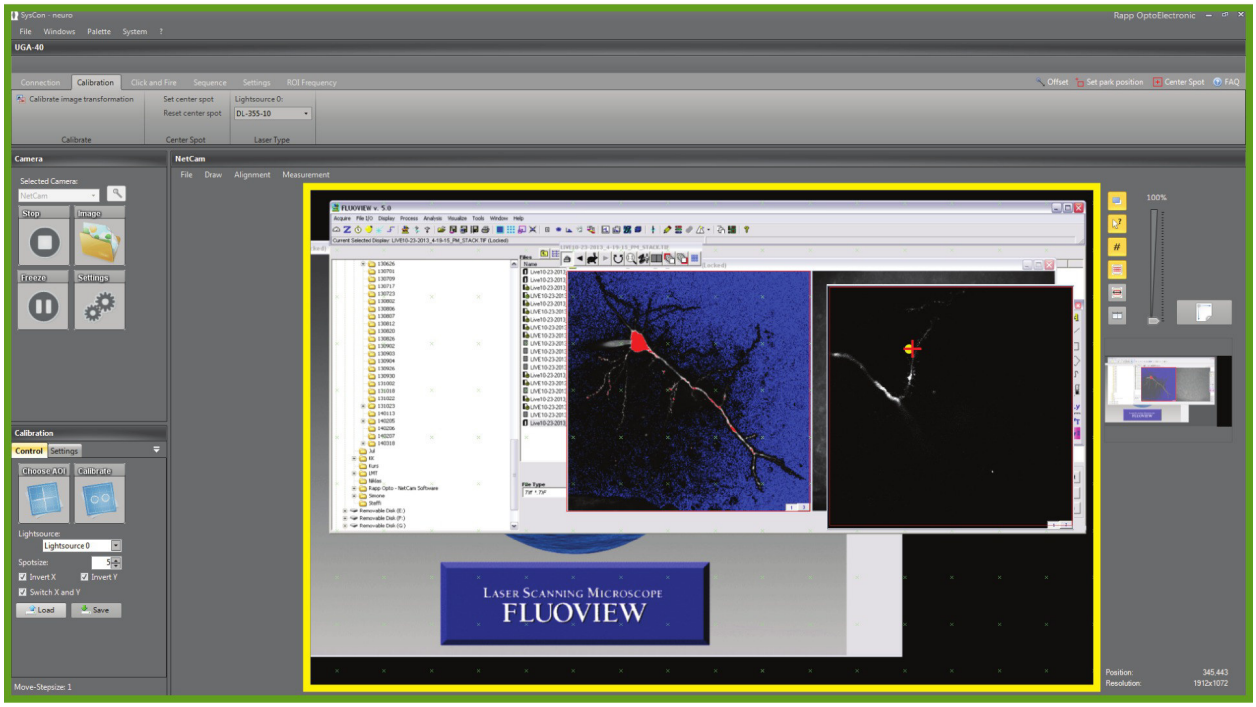

Figure 3. Adjustment of the uncaging spot: To precisely position the uncaging spot, a screen shot of the imaging software (yellow frame) is imported into the uncaging software (green frame). The left image within the yellow frame represents a Hi-Lo coded image (blue: black pixels, red: saturated pixels) of the entire CA1 pyramidal cell. The image is overlaid by the calibration grid of the uncaging software (green "X"s). To the right, a magnified part of the cell is shown with the overlaid uncaging spot (red cross). The yellow spot is the automatically overlaid image of the uncaging beam. Please click here to view a larger version of this figure.

4. Turn on micromanipulators, electrophysiology components, and pressure application device for delivery of the caged compound to the target region.
5. Install a focal pressure application device for local perfusion of caged compounds. This will reduce costs enormously as compared to bath perfusion of these substances. Adjust the holding pressure to the given atmospheric pressure to prevent a drag of ACSF into or a leakage of caged substances from the application pipette.
   NOTE: The pressure application device hosts a highly precise and ultrafast micro-valve in the pipette holder. This enables to employ minimal application pressures and therefore reduces movement artifacts to a minimum during the local perfusion with the caged compound.
6. Pull pipettes for whole-cell patch-clamp and local perfusion using fire-polished borosilicate glass capillaries. Pipettes should have a tip diameter of ~1 µm and a resistance of R ≈ 3 MΩ (values determined with K-$MeSO_3$-based ICS).
7. Place slice in the experimental bath and affix it with a grid (platinum frame 250 µM thick, spanned with surgical filaments, o.d. 40 µm) (**Figure 4A, B**). Use an inverted, tip-broken, and fire-polished Pasteur pipette (suction ball at the side of the broken tip) for slice transfer. Avoid bending and any other harsh handling of the slice.

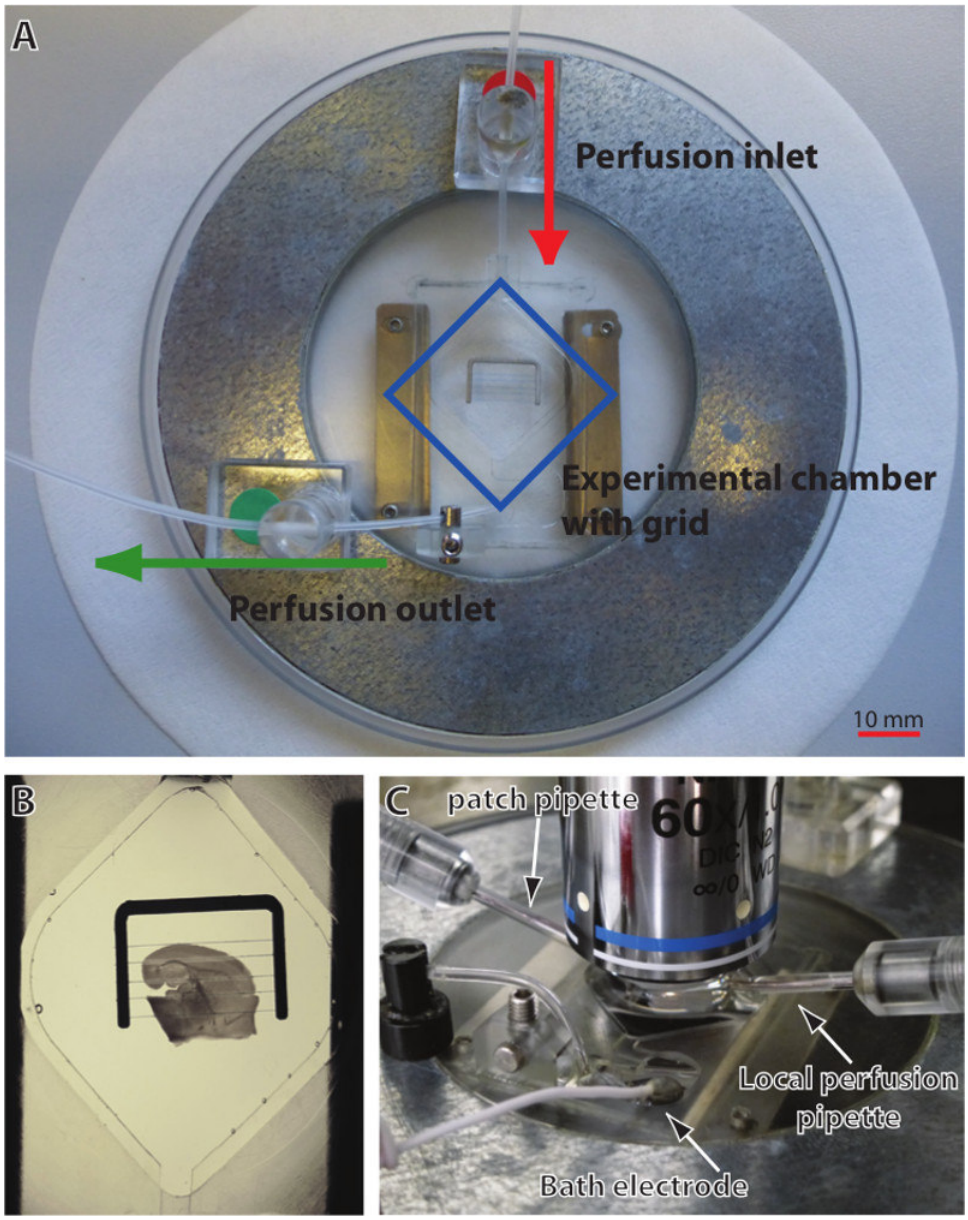

Figure 4. Components of the experimental bath and positioning of the bath at the microscope stage. (A) The experimental bath consists of the bath chamber itself (blue square), which is surrounded by a magnetic metal ring. The tubing ensures continuous perfusion of the bath with saline (ACSF). The grid to hold down and fix the slice is put into the bath chamber. **(B)** Acute slice preparation positioned within the bath chamber. The slice is fixed by the threads of the grid. **(C)** Positioning and geometry of the experimental bath at the microscope stage during the experiments.

8. Place bath at the microscope stage and permanently perfuse slice with ACSF.

4. Whole-cell Patch-clamping

1. Load patch pipette with ICS containing SBFI and load local perfusion pipette with caged compound. Attach pipettes to corresponding micromanipulators. Place reference electrode in bath. Make sure that you are grounded permanently to avoid damage to the head stage (c.f. **Figure 4C**).
2. Lower both pipettes into bath and place them above the hippocampal CA1 region. Apply gentle pressure to patch pipette (+40 mbar) to avoid dilution of the ICS with ACSF.
3. Compensate the offset potential of the patch pipette using the electrophysiology software.
4. Approach a CA1 pyramidal cell with patch pipette employing IR-DIC video microscopy. Apply gentle suction until a Giga-seal is obtained. Choose a cell the soma of which is located 30 -70 µm below the surface of the slice to ensure intact cell morphology on the one hand side and low scattering and attenuation of the uncaging beam on the other hand side.
5. Compensate for fast capacity. Break membrane and open cell to gain whole-cell configuration.
6. Compensate for slow capacity and series resistance.

7. Allow the cell to be dialyzed with the SBFI-ICS for at least 30 min before starting the imaging experiments.

5. Multi-photon imaging and stimulation

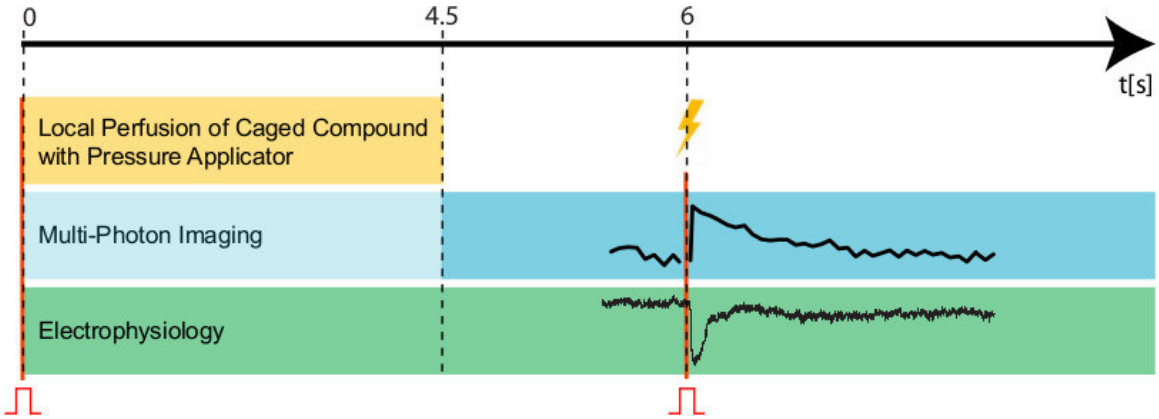

Figure 5. Experimental protocol. To initialize an experiment, a trigger pulse (indicated by red sign (ɲ)and the red line) is set to simultaneously start the imaging (blue), the electrophysiology (green), and the administration of the caged compound (yellow) at time point 0 sec. During this first period, the imaging beam should be entirely dimmed (light blue). After 4.5 sec (dashed line), the local perfusion of the caged compound is terminated and the imaging beam should be set to its working intensity for data acquisition (blue). 1.5 sec afterwards (time point 6 sec), a second trigger pulse is given (indicated by red sign (ɲ) and the red line), which initializes the UV flash unit (duration of the flash: 300 msec; indicated by the yellow flash) and sets markers in the electrophysiology and the imaging protocol.

1. Add tetrodotoxin (TTX, 500 nM) to ACSF to prevent activation of voltage-gated sodium channels and generation of action potentials.
2. Visualize cellular morphology using multi-photon excitation and resulting SBFI fluorescence and choose a spiny dendrite for experiment. Zoom in for images at a higher resolution and place a clip box around the dendrite.
3. Fill a standard patch pipette with 10 µl ACSF containing caged glutamate. Connect the pipette to the pressure application system and attach it to the micromanipulator.
4. Place pipette with caged compound near the dendrite (~30 µm). Position the pipette to allow efficient local perfusion of the dendrite of choice. Adjust the uncaging laser: position the uncaging spot close (~1 - 2 µm) to the structure of interest.
5. Set regions of interest on the chosen dendrite and adjacent spines using imaging software.
6. Approach the region of interest and focally inject the caged compound for several sec with low pressure (<3 PSI). Start patch clamp and fluorescence recordings (at 790 nm multi-photon excitation) via trigger signal.
   NOTE: During the local perfusion of the caged compound, the excitation beam is completely dimmed to prevent bleaching.
7. Stop local perfusion of the caged compound. Increase intensity of the two-photon laser to enable efficient excitation of SBFI and apply a UV flash to initialize uncaging (uncaging duration 300 msec).
8. Monitor changes in SBFI fluorescence. Stop recording after SBFI fluorescence has recovered back to baseline.

6. Pharmacology

1. To test the involvement of ionotropic glutamate receptors in the generation of the currents and/or sodium signals evoked by UV flash photolysis of caged glutamate, employ receptor blockers.
   1. Switch to ACSF containing the AMPA-receptor blocker cyano-nitroquinoxaline-dione (CNQX, 10 µM) and the NMDA-receptor blocker amino-phosphonopentanoate (APV, 50 µM) in addition to TTX (see above) and perfuse slice for at least 10 min.
   2. Repeat stimulation procedure (see **5.4** and **5.5**.)

2. Reversibility of the inhibitors' effects
   1. Switch back to normal ACSF containing only TTX.
   2. Perfuse slice for 20 min.
   3. Repeat stimulation procedure (see **5.4** and **5.5**.).

7. Morphology

1. Record a XYZ-stack of the clip box-region set for the performed measurements. Ensure that this stack is oversampled spatially (at least 0.2 µm per pixel) to enable optimal image deconvolution and to increase image quality and resolution.
2. Record a XYZ-stack of the entire cell to assess cell morphology.
3. Run deconvolution algorithm.

Representative Results

In the present study, we demonstrate a procedure for multi-photon microscopy of cellular sodium dynamics with the sodium-dependent fluorescent dye SBFI in CA1 pyramidal neurons of acute mouse hippocampal tissue slices. Moreover, we show how to combine this imaging

technique with laser-scanning-based uncaging of neuro-active compounds (*e.g.* caged glutamate) and its precise targeting to cellular micro-domains.

Loading neurons with SBFI through the patch-pipette enabled the visualization of the entire cell including fine dendrites and adjacent spines by employing multi-photon excitation (**Figure 6A, B, D** and **Figure 7A**).

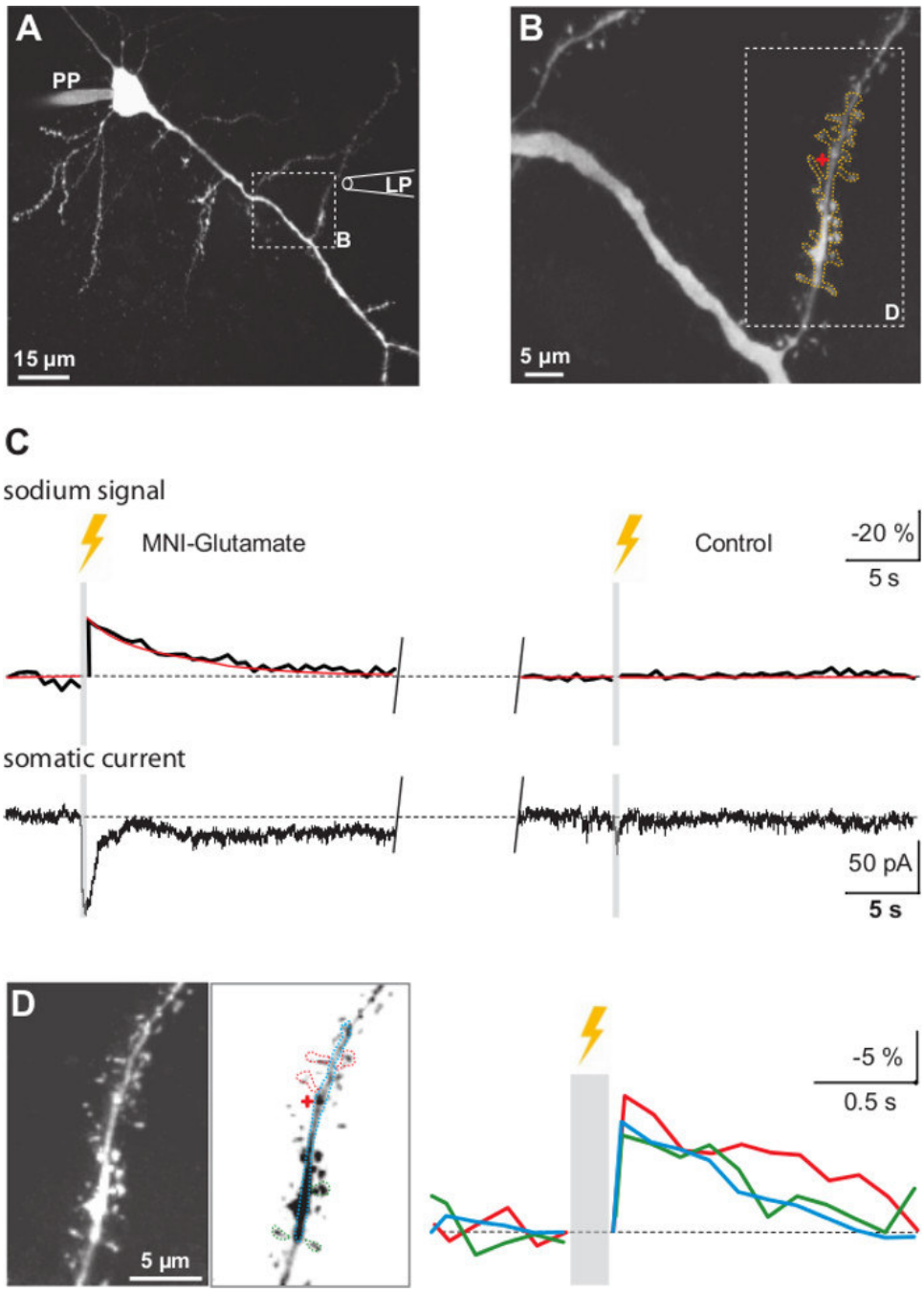

Figure 6. Sodium signals and synaptic currents induced by flash photolysis of caged glutamate. (A) Maximal projection image of a CA1 pyramidal neuron loaded with SBFI via the patch pipette (PP). The box indicates the area shown enlarged in B. LP indicates the position and orientation of the pipette for local perfusion of caged glutamate. **(B)** High power maximum projection of a stack of optical sections of a dendrite with adjacent dendritic spines. The stacks of optical sections underwent z-alignment and deconvolution. The red cross indicates the target region of the uncaging beam. The orange dotted line delineates the region of interest from which the fluorescence emission was recorded. The box indicates the area shown enlarged in D. **(C) Left:** Sodium signal (**upper row**) and somatic inward current (**lower row**) induced by flash photolysis of caged glutamate (indicated by yellow flash). The red line represents a fit of the experimental data. The grey area represents the period in which the uncaging flash (300 msec) obstructed the imaging of SBFI fluorescence. **Right:** Without pre-perfusion with caged glutamate, the same UV-flash neither evoked a change in SBFI emission, nor an inward current. **(D) Left**: High power image of the dendrite and adjacent spines as delineated in B. Alongside, the same image with inverted grey values. The dotted lines indicate the regions of interest in which the fluorescence emission was recorded. The red cross indicates the localization of the uncaging beam. **Right:** Sodium transients induced by UV-

flash photolysis of caged glutamate. Blue trace: sodium signals in the dendrite; red trace: averaged response from three spines adjacent to the uncaging spot; green trace: averaged response from three distant spines. Please click here for a larger version of this figure.

After local perfusion with caged glutamate, applying a UV-flash close to a dendrite resulted in a transient decrease in fluorescence emission of SBFI, reflecting an increase in the intracellular sodium concentration (**Figure 6C, D and Figure 7B**). At the same time, an inward current was recorded at the soma (**Figure 6C and Figure 7B**). Increasing the duration of the UV flash resulted in increasing amplitudes of both the elicited inward currents and the sodium signals (data not shown), indicating that the system was well within its dynamic range and that neither uncaging nor cellular responses were saturated. Application of a UV-flash of identical or longer duration to slices which had not been pre-perfused with caged glutamate, never elicited changes in SBFI fluorescence nor inward currents, indicating that these signals are due to the uncaging of glutamate (**Figure 6C**). Moreover, these results show that no interdependency of imaging- and uncaging components is observed under our experimental conditions. Sodium signals could also be detected in dendritic spines (**Figure 6D**). While we did not attempt to achieve stimulation of a single spine only with glutamate uncaging, peak amplitudes tended to be slightly higher in spines close to the uncaging spot, whereas spines further away showed virtually identical fluorescence changes as the parent dendrite (**Figure 6D**).

Finally, we studied the pathway for sodium influx into dendrites and spines in response to uncaging of glutamate. To this end, we employed CNQX and APV, which are selective blockers for the sodium-permeable, ionotropic glutamate receptors of the AMPA- and NMDA-subtype, respectively. Our results show that glutamate-induced intracellular sodium signals and the elicited somatic currents were omitted in the presence of these blockers (**Figure 7B**). Upon wash-out of the blockers, the signals are regained. This demonstrates that uncaging of glutamate activates ionotropic glutamate receptors on CA1 pyramidal neurons, which mediate the influx of sodium into dendrites and spines, resulting in intracellular sodium transients and inward currents.

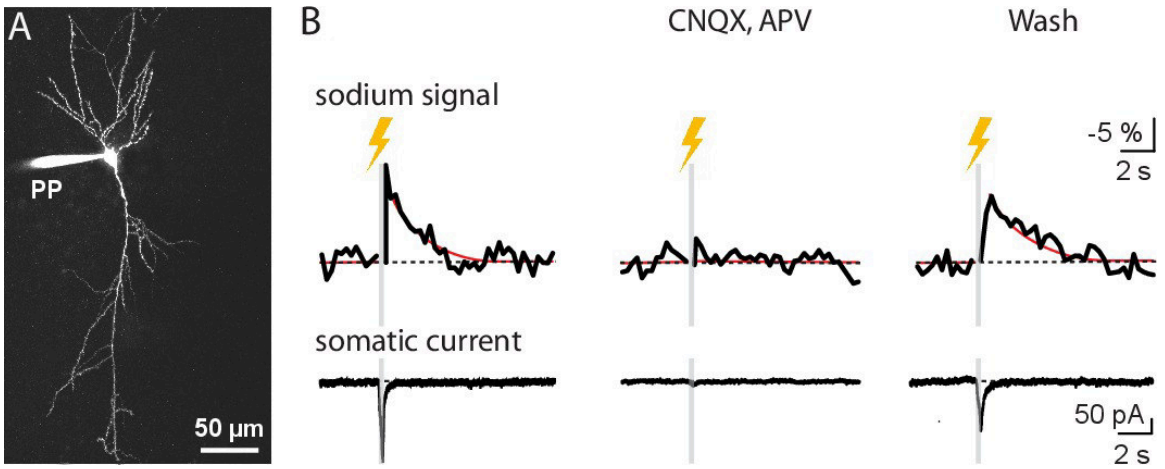

Figure 7. Pharmacological profile of evoked sodium signals and inward currents. (A) SBFI-filled CA1 pyramidal neuron with patch pipette (PP) attached to the soma. **(B) Left:** Sodium transient and somatic current induced by photo-activation of caged glutamate in a dendrite and attached spines. **Center:** Perfusion with the ionotropic glutamate receptor blockers CNQX and APV inhibits both the sodium signal and the inward current induced by uncaging. **Right:** Upon wash-out of the blockers, the signals are restored. The red line represents a fit of the experimental data. The grey area represents the period in which the uncaging flash (300 msec) obstructed the imaging of SBFI fluorescence. Please click here for a larger version of this figure.

Discussion

The present study shows that SBFI is well suited for two-photon imaging of intracellular sodium transients in small cellular compartments. It has to be kept in mind, however, that the quantum efficiency of SBFI is rather low[15] and relative changes in the sodium concentration are quite small with physiological activity. Thus, high-resolution measurement of Na^+ transients in fine processes is a relatively tedious task, and binning or averaging of several trials may be necessary to obtain satisfactory signals. In addition, the kinetics of sodium transients are surprisingly slow, making it obligatory to record for extended time periods. This observation corresponds to those in earlier studies, where monoexponential decay of sodium transients in neuronal dendrites and in astrocytes was characterized by large decay time constants in the range of 10 sec at room temperature[1,2,6]. Sodium transients thus seem to exert a much slower time course and much larger decay time constants as compared to calcium transients[16].

Set aside these drawbacks, sodium imaging proves to be a valuable tool for the investigation of physiological properties of neuronal subdomains. For example, sodium imaging can serve to monitor excitatory synaptic activity at or close to active synapses. Because sodium is essentially not buffered[8,17], activity-induced sodium transients are linearly related to a wide range of synaptic glutamate release or exogenously applied glutamate. They hence represent direct and unbiased indicators of neuronal glutamatergic activity. Moreover, sodium indicator dyes exhibit high K_d's (SBFI's K_d is in the range of 25 mM[1]). Even at the relatively high intracellular dye concentrations used to achieve sufficient brightness (usually 0.5 - 1 mM), the high K_d's imply that the dyes themselves do not act as buffers for sodium. Consequently, they do not distort the amplitude nor time course of sodium transients, which is always a concern when calcium-sensitive dyes are introduced into the cells[18]. It can thus be assumed that the detected signals represent a good measure of the "real" changes in intracellular sodium. Their slow time course then implies that the velocity for intracellular diffusion for sodium in neurons is much smaller than previously assumed[19].

A critical requirement for the successful execution of experiments addressing the properties of excitatory synaptic transmission and sodium influx pathways into spines and dendrites is the induction of a fast and highly localized activation of postsynaptic structures. This can be obtained

by fast and local application of glutamate or glutamate agonists in the direct vicinity of a spine or a dendrite by the flash photolysis of caged compounds. Flash photolysis does not mechanically damage the tissue, is free of movement artifacts and is well established for the investigation of related questions (*e.g.* local calcium signaling). The diameter of the uncaging spot was 1.5 µm in the xy-plane. Uncaging close to a spiny dendrite induced sodium signals in both spines and the parent dendrite. Whereas the signals tended to be largest in spines closest to the uncaging spot, the amplitudes in the parent dendrite and spines further away were still rather similar to those in direct vicinity of the uncaging spot. Uncaging was performed for 300 msec during which inward currents increased in amplitude. Uncaged glutamate might have diffused in the tissue during the same time period, activating ionotropic glutamate receptors and sodium influx on dendritic regions and spines further away from the uncaging spot.

An intrinsic problem that occurs when using a UV laser for photolysis of caged compounds administered through the cell bathing solution is 'inner filtering'. Because of the high absorption rate of the cage, UV light is attenuated strongly along the way from the objective to the stimulation site[20,21]. A feasible way to avoid this is local perfusion with the cage that is restricted only to the stimulation site, which furthermore decreases the amount of caged compound needed to a minimum. As compared to UV laser-scanning-mediated uncaging, near-infra-red two-photon uncaging[22] is spatially more precise, mainly because the accuracy of the stimulation is increased in the z-axis. On the other hand, due to the small cross-section of commonly used cages for longer wavelengths as employed with two-photon excitation, either a high concentration of the caged compound or very high, potentially phototoxic light intensities are needed. Also, two-photon uncaging necessitates a much higher investment in the equipment; among others, an additional IR laser plus the required optical components, are needed.

Both SBFI and MNI-glutamate are excitable in the identical wavelength range. This may lead to an unintended interdependency of UV uncaging laser and SBFI or IR imaging laser and MNI-glutamate, resulting in bleaching of SBFI by the uncaging flash and /or a continuous uncaging of glutamate by the IR beam. However, as shown in **Figure 6C**, neither a UV flash by itself nor the multi photon imaging caused such reciprocal effects under our experimental conditions.

UV-flash systems similar to the one described here are used routinely in many other laboratories and can relatively easily be incorporated into any existing multi-photon imaging microscope. It offers the advantage that the laser beam for photolysis can be positioned freely in the field of view. In addition, the system enables a fast and automated repositioning of the laser beam and the release volume, respectively, in the field of view during an experiment. Our modification simplifies and improves the accurate positioning of the uncaging spot, so that the frames of the imaging software can serve to adjust imaging and uncaging frames congruently.

Taken together, whole-cell patch-clamp and multi-photon sodium imaging in dendrites and spines of central neurons, combined with a modified procedure for UV-light-induced uncaging of glutamate, allows reliable and focal activation of glutamate receptors in the tissue. It can thus serve to analyze the properties of excitatory synaptic transmission and of postsynaptic sodium signals in neurons in the intact tissue.

Disclosures

The authors declare no competing interests. The authors received financial support enabling Open Access Publication by Rapp OptoElectronic (Wedel, Germany), which produces an instrument used in the video article. The company was neither involved in the experiments nor in the data handling nor in the manuscript writing.

Acknowledgements

This study was supported by a grant of the German Science Foundation (DFG, Ro2327/6-1) to C.R.R. The authors wish to thank S. Durry and C. Roderigo for expert technical assistance, and M. Dübbert (Electronics Laboratory, Zoological Institute, University of Cologne, Germany) for help in implementing the Pockels cell controller and the HF switch.

References

1. Rose, C. R., Kovalchuk, Y., Eilers, J., & Konnerth, A. Two-photon Na^+ imaging in spines and fine dendrites of central neurons. *Pflueg. Arch., Eur. J. Phy.***439**, 201 - 207, doi:10.1007/s004249900123, (1999).
2. Rose, C. R., & Konnerth, A. NMDA receptor-mediated Na^+ signals in spines and dendrites. *J. Neurosci.***21**, 4207 - 4214, (2001).
3. Meier, S. D., Kovalchuk, Y., & Rose, C. R. Properties of the new fluorescent Na^+ indicator CoroNa Green: comparison with SBFI and confocal Na^+ imaging. *J. Neurosci. Meth.***155**, 251 - 259, doi:10.1016/J. Neumeth. 2006.01.009, (2006).
4. Lamy, C., & Chatton, J.-Y. Optical probing of sodium dynamics in neurons and astrocytes. *NeuroImage.***58**, 572 - 578, doi:10.1016/j. neuroimage.2011.06.074, (2011).
5. Lasser-Ross, N., & Ross, W. Imaging voltage and synaptically activated sodium transients in cerebellar Purkinje cells. *Proc. Roy. Soc. B-Biol. Sci.***247**, 35 - 39, doi:10.1098/rspb.1992.0006, (1992).
6. Bennay, M., Langer, J., Meier, S. D., Kafitz, K. W., & Rose, C. R. Sodium signals in cerebellar Purkinje neurons and Bergmann glial cells evoked by glutamatergic synaptic transmission. *Glia.***56**, 1138-1149, doi:10.1002/glia.20685, (2008).
7. Baranauskas, G., David, Y., & Fleidervish, I. Spatial mismatch between the Na^+ flux and spike initiation in axon initial segment. *Proc. Natl. Acad. Sci. USA.***110**, 4051-4056, doi:10.1073/pnas.1215125110, (2013).
8. Fleidervish, I., Lasser-Ross, N., Gutnick, M., & Ross, W. Na^+ imaging reveals little difference in action potential-evoked Na+ influx between axon and soma. *Nat. Neurosci.***13**, 852-860, doi:10.1038/nn.2574, (2010).
9. Denk, W., Piston, D., & Webb, W. in *Handbook of Biological Confocal Microscopy.*(ed Pawley JB) 445-458 Plenum Press, (1995).
10. Jaffe, D., *et al.*The spread of Na^+ spikes determines the pattern of dendritic Ca^{2+} entry into hippocampal neurons. *Nature.***357**, 244-246, doi:10.1038/357244a0, (1992).
11. Boccaccio, A., Sagheddu, C., & Menini, A. Flash photolysis of caged compounds in the cilia of olfactory sensory neurons. *J. Vis. Exp.*doi:10.3791/3195, (2011).

12. Ikrar, T., Olivas, N., Shi, Y., & Xu, X. Mapping inhibitory neuronal circuits by laser scanning photostimulation. *J. Vis. Exp.*doi:10.3791/3109, (2011).
13. Mathis, D. M., Furman, J. L., & Norris, C. M. Preparation of acute hippocampal slices from rats and transgenic mice for the study of synaptic alterations during aging and amyloid pathology. *J. Vis. Exp.*doi:10.3791/2330, (2011).
14. Pannasch, U., Sibille, J., & Rouach, N. Dual electrophysiological recordings of synaptically-evoked astroglial and neuronal responses in acute hippocampal slices. *J. Vis. Exp.* doi:10.3791/4418, (2012).
15. Minta, A., & Tsien, R. Fluorescent indicators for cytosolic sodium. *J. Biol. Chem.***264**, 19449 - 19457, (1989).
16. Kuruma, A., Inoue, T., & Mikoshiba, K. Dynamics of Ca(2+) and Na(+) in the dendrites of mouse cerebellar Purkinje cells evoked by parallel fibre stimulation. *Eur. J. Neurosci.***18**, 2677-2689, (2003).
17. Despa, S., & Bers, D. M. Na/K pump current and [Na](i) in rabbit ventricular myocytes: Local [Na](i) depletion and Na buffering. *Biophys. J.***84**, 4157-4166, doi:10.1016/S0006-3495(03)75140-6, (2003).
18. Regehr, W., & Tank, D. Calcium concentration dynamics produced by synaptic activation of CA1 hippocampal pyramidal cells. *J. Neurosci.***12**, 4202 - 4223, (1992).
19. Kushmerick, M. J., & Podolsky, R. J. Ionic mobility in muscle cells. *Science.***166**, 1297-1298, (1969).
20. Palma-Cerda, F., *et al.*New caged neurotransmitter analogs selective for glutamate receptor sub-types based on methoxynitroindoline and nitrophenylethoxycarbonyl caging groups. *Neuropharmacology.***63**, 624 - 634, doi:10.1016/j.neuropharm.2012.05.010, (2012).
21. Trigo, F., Corrie, J., & Ogden, D. Laser photolysis of caged compounds at 405 nm: photochemical advantages, localisation, phototoxicity and methods for calibration. *J. Neurosci. Meth.***180**, 9 - 21, doi:10.1016/j.jneumeth.2009.01.032, (2009).
22. Nikolenko, V., Peterka, D., Araya, R., Woodruff, A., & Yuste, R. Spatial light modulator microscopy. *Cold Spring Harbor protocols.***2013**, 1132 - 1141, doi:10.1101/pdb.top079517, (2013).

8.3 Extrusion versus diffusion: mechanisms for recovery from sodium loads in mouse CA1 pyramidal neurons

Status: Veröffentlicht am 15.04.2015 im „Journal of Physiology“.

Persönlicher Beitrag: 15%. Ich war an der Erstellung des experimentellen Konzepts zur Bestimmung des Diffusionskoeffizienten beteiligt. Die Analyse der zugehörigen Experimente und Interpretation der betreffenden Daten wurde von mir durchgeführt. Ebenso wurden die Experimente zur Diffusion in Dendriten bei verschiedenen Temperaturen von mir durchgeführt und analysiert.

JPn
Neuroscience
The Journal of Physiology

Extrusion versus diffusion: mechanisms for recovery from sodium loads in mouse CA1 pyramidal neurons

Miguel A. Mondragão[1], Hartmut Schmidt[2], Christian Kleinhans[1], Julia Langer[1], Karl W. Kafitz[1] and Christine R. Rose[1]

[1] *Institute of Neurobiology, Faculty of Mathematics and Natural Sciences, Heinrich Heine University Düsseldorf, Düsseldorf, Germany*
[2] *Carl-Ludwig-Institute for Physiology, Medical Faculty, University of Leipzig, Leipzig, Germany*

Key points

- Neuronal activity causes local or global sodium signalling in neurons, depending on the pattern of synaptic activity.
- Recovery from global sodium loads critically relies on Na^+/K^+-ATPase and an intact energy metabolism in both somata and dendrites.
- For recovery from local sodium loads in dendrites, Na^+/K^+-ATPase activity is not required *per se*. Instead, recovery is predominately mediated by lateral diffusion, exhibiting rates that are 10-fold higher than for global sodium signals.
- Recovery from local dendritic sodium increases is still efficient during short periods of energy deprivation, indicating that fast diffusion of sodium to non-stimulated regions strongly reduces local energy requirements.

Abstract Excitatory activity is accompanied by sodium influx into neurones as a result of the opening of voltage- and ligand-activated channels. Recovery from resulting sodium transients has mainly been attributed to Na^+/K^+-ATPase (NKA). Because sodium ions are highly mobile, diffusion could provide an additional pathway. We tested this in hippocampal neurones using whole-cell patch-clamp recordings and sodium imaging. Somatic sodium transients induced by local glutamate application recovered at a maximum rate of 8 mM min^{-1} (~0.03 mM min^{-1} μm^{-2}). Somatic sodium extrusion was accelerated at higher temperature and blocked by ouabain, emphasizing its dependence on NKA. Moreover, it was slowed down during inhibition of glycolysis by sodium fluoride (NaF). Local glutamate application to dendrites revealed a 10-fold higher apparent dendritic sodium extrusion rate compared to somata. Recovery was almost unaltered by increased temperature, ouabain or NaF. We found that sodium diffused along primary dendrites with a diffusion coefficient of ~330 $\mu m^2/s$. During global glutamate application, impeding substantial net diffusion, apparent dendritic extrusion rates were reduced to somatic rates and also affected by NaF. Numerical simulations confirmed the essential role of NKA for the recovery of somatic, but not dendritic sodium loads. Our data show that sodium export upon global sodium increases is largely mediated by NKA and depends on an intact energy metabolism. For recovery from local dendritic sodium increases, diffusion dominates over extrusion, operating efficiently even during short periods of energy deprivation. Although sodium will eventually be extruded by the NKA, its diffusion-based fast dissemination to non-stimulated regions might reduce local energy requirements.

(Resubmitted 14 March 2016; accepted after revision 7 April 2016; first published online 15 April 2016)
Corresponding author C. R. Rose: Institute of Neurobiology, Heinrich Heine University Duesseldorf, Universitaetsstrasse 1, Building 26.02.00, 40225 Duesseldorf, Germany. E-mail: rose@uni-duesseldorf.de

DOI: 10.1113/JP272431

Abbreviations K_M, Michaelis–Menten constant; LTP, long term potentiation; MgG-AM, magnesium-green-acetoxymethyl ester; mACSF, modified artificial cerebrospinal fluid; NaF, sodium fluoride; NKA, sodium-potassium ATPase; ROI, region of interest; SBFI, sodium-binding benzofuran isophthalate; SBFI-AM, sodium-binding benzofuran isophthalate-acetoxymethyl ester; τ, time constant; V_{max}, maximum rate for recovery from sodium loads.

Introduction

The balance of extra- and intracellular ion concentrations is of upmost functional importance for the brain and requires constant cellular transport activity and energy supply (Erecinska & Silver, 1994; Somjen, 2002). Most energy is used for the export of sodium, a task which is mediated by the plasma membrane Na^+/K^+-ATPase (NKA) (Sweadner, 1989; Kaplan, 2002). Estimates indicate that this pump alone requires ∼50% of all ATP used by the brain (Whittam, 1962; Astrup *et al.* 1981; Ames, 2000). Mutations in NKA are known to be the origin of many neurological problems such as cognitive deficits (Moseley *et al.* 2007), parkinsonism (De Carvalho Aguiar *et al.* 2004) or hemiplegic migraine (Capendeguy & Horisberger, 2004).

Inhibition of NKA results in an immediate increase in intracellular sodium of central neurons even at rest, emphasizing the need for constant pump activity as a result of constitutive sodium influx (e.g. through secondary active transporters such as sodium-calcium exchange or sodium-proton exchange) (Rose & Ransom, 1997; Kelly & Rose, 2010*a*; Kelly & Rose, 2010*b*). Additional sodium loads are imposed onto active neurons. Here, an influx of sodium through voltage- and ligand-gated channels represents a major metabolic challenge. In fact, sodium influx following action potentials requires 22–39% of cellular ATP generation, whereas 34–52% is allocated for postsynaptic ion fluxes following synaptic transmission (Lennie, 2003; Hallermann *et al.* 2012; Harris *et al.* 2012).

Former studies have firmly established that action potentials and the opening of voltage-gated sodium channels cause an influx of sodium into axons (Kole *et al.* 2008; Fleidervish *et al.* 2010) and, with back-propagating action potentials present, also into dendrites and spines of central neurons (Jaffe *et al.* 1992; Rose *et al.* 1999), resulting in significant sodium transients in these cellular compartments. Especially prominent activity-related sodium transients occur in postsynaptic dendrites in response to excitatory synaptic activity and the influx of sodium through glutamate-gated ionotropic receptors (Lasser-Ross & Ross, 1992; Rose & Konnerth, 2001; Bennay *et al.* 2008). In dendrites of hippocampal CA1 pyramidal neurons, short-burst synaptic stimulation of glutamatergic fibres (Schaffer collaterals) induced local sodium transients that amounted to 10 mM, whereas, with a typical LTP induction protocol, dendritic sodium rose by even 45 mM (Rose & Konnerth, 2001). In addition to these local sodium signals, arising close to activated synapses, highly synchronized global sodium signalling was reported from the somata of the CA1 pyramidal cell population under epileptiform conditions (Karus *et al.* 2015*a*). Because NKA is the only relevant transporter for the export of sodium under physiological conditions, it was hypothesized that recovery from both local and global activity-related sodium transients was mainly mediated by activity of the pump (Rose & Konnerth, 2001; Karus *et al.* 2015*a*).

Sodium, however, is an essentially non-buffered, highly mobile ion for which intracellular diffusion coefficients of ∼600 $\mu m^2/s$ have been reported (Kushmerick & Podolsky, 1969), which considerably exceed those of calcium (Allbritton *et al.* 1992). Thus, another mechanism that could contribute to efficient recovery from local dendritic sodium increases in addition to NKA is the fast diffusion of sodium ions into non-activated regions. Indeed, recent work on axon initial segments has provided evidence that fast sodium transients induced by the opening of voltage-gated sodium channels during action potential generation are not altered upon inhibition of the NKA by ouabain, indicating that diffusion was responsible for their fast decay (Fleidervish *et al.* 2010).

In the present study, we have addressed this question by studying the properties of recovery from glutamate-induced sodium transients in cell bodies and dendrites of CA1 pyramidal neurons, employing quantitative, ratiometric imaging with the sodium-sensitive fluorescent dye sodium-binding benzofuran isophthalate (SBFI). Our results show that NKA governs recovery from global sodium increases in both cell bodies and dendrites. Recovery from local dendritic sodium loads, however, is predominately mediated by diffusion, exhibiting recovery rates that are more than one order of magnitude higher.

Methods

Ethical approval

The present study was carried out in strict accordance with *The Journal of Physiology*'s policy (Grundy, 2015), as well as with the institutional guidelines of the Heinrich Heine University Düsseldorf and the European Community Council Directive (86/609/EEC). All experiments were communicated to and approved by the Animal Welfare Office at the Animal Care and Use Facility of the Heinrich Heine University Düsseldorf (institutional act number:

O52/05) in accordance with the recommendations of the European Commission (Close, 1997).

Tissue dissection and saline composition

Experiments were performed on acute tissue slices (250 μm) of mouse hippocampus (Mus musculus, Balb/C; postnatal days 14–20, both sexes). Animals were anaesthetized with CO_2 and immediately decapitated. The brain was then removed and parasagittal hippocampal slices prepared using standard techniques (Meier *et al.*, 2006) in cold (2–4ºC) modified artificial cerebrospinal fluid (mACSF). mACSF contained (in mM): 125 NaCl, 2.5 KCl, 0.5 $CaCl_2$, 6 $MgCl_2$, 1.25 NaH_2PO_4, 26 $NaHCO_3$ and 20 glucose and was bubbled with 95% O_2 and 5% CO_2, pH 7.4; osmolarity was 310 mosmol l^{-1}. Slices were cut using a vibratome (Microm HM 650 V; Thermo Scientific, Waltham, MA, USA) and subsequently incubated at 34ºC for 30 min.

After the incubation period, slices were kept at room temperature (20–22ºC) in standard artificial cerebrospinal fluid (ACSF) until they were used for experiments, which were also performed at room temperature. The composition of the ACSF was (in mM): 125 NaCl, 2.5 KCl, 2 $CaCl_2$, 1 $MgCl_2$, 1.25 NaH_2PO_4, 26 $NaHCO_3$ and 20 glucose, bubbled with 95% O_2 and 5% CO_2, pH 7.4. During the experiments, slices were constantly perfused with ACSF to which TTX (0.5 μM), a blocker of voltage-gated ion channels, was routinely added to prevent action potential generation.

All substances, except glutamate, were applied via bath perfusion. Chemicals were purchased from Sigma-Aldrich (Munich, Germany), except for tetrodotoxin (Abcam, Cambridge, UK) and ouabain (Calbiochem, Darmstadt, Germany). Glutamate (0.5 mM) was dissolved in Hepes-buffered saline composed of (in mM): 125 NaCl, 25 Hepes, 3 KCl, 2 $MgSO_4$, 2 $CaCl_2$ and 1.25 NaH_2PO_4. Glutamate was applied for 100 ms by a pressure application device (PDES-02D; NPI Electronic GmbH, Tamm, Germany) coupled to borosilicate glass micropipettes (Hilgenberg, Waldkappel, Germany) placed either 5–10 μm from the cell body or the primary apical dendrite of a selected cell (see Fig. 3*A* and 3*C*).

Whole-cell patch-clamp

Somatic whole-cell patch-clamp recordings were performed from CA1 hippocampal neurons using an upright microscope (BX51WI; Olympus Europe, Hamburg, Germany), equipped with an Achroplan 40× objective (water immersion, NA 0.8; Zeiss, Göttingen, Germany), using an EPC10 amplifier and PatchMaster software (HEKA Elektronik, Lambrecht, Germany). Patch pipettes were pulled from borosilicate glass capillaries (Hilgenberg) using a vertical puller (PP-830; Narishige, Tokyo, Japan). Pipettes were filled with intracellular saline containing (in mM): 120 K-$MeSO_3$, 10 Hepes (*N*-(2-hydroxymethyl) piperazine-*N*′-2-ethanesulphonic acid) 32 KCl, 4 NaCl, 1 EGTA (ethylene glycol tetracetic acid), 4 Mg-ATP and 0.4 Na_3-GTP, as well as the K^+ salt of SBFI (0.1–2 mM; TEFLabs Inc., Austin, TX, USA), titrated with KOH to pH 7.3. Pipette resistance was 2.3–3.0 MΩ when filled with this saline. Liquid junction potential was not corrected. Cells were routinely held in the voltage clamp mode at a holding potential of –60 mV. Data were sampled at 1 kHz and processed and analysed employing IGOR Pro (WaveMetrics, Lake Oswego, OR, USA).

Wide-field imaging

For sodium imaging, individual neurons were loaded with the sodium-selective fluorescent dye SBFI (0.1–2 mM) via a patch pipette. Alternatively, cells were loaded by bolus injection of SBFI-AM (sodium-binding benzofuran isophthalate-acetoxymethyl ester; Invitrogen, Karlsruhe, Germany) into the CA1 region as described previously (Meier *et al.* 2006; Langer & Rose, 2009). De-esterification was allowed for 1 h before commencing the imaging experiments.

Wide-field fluorescence imaging was performed using a variable scan digital imaging system (TILL Photonics, Martinsried, Germany) attached to a microscope (see above) and a CCD camera (Imago VGA; TILL Photonics). SBFI was alternately excited at 340 nm (sodium-insensitive wavelength) and at 380 nm (sodium-sensitive wavelength) (cf. Fig. 2*A* and *B*). Images were captured at a frequency of 1 or 4 Hz. SBFI emission was collected above 440 nm from defined regions of interest (ROIs), representing either the soma or the primary apical dendrite. After standard dynamic background correction (Langer & Rose, 2009), the fluorescence ratio ($R_{340/380}$) was calculated for each ROI and analysed off-line using OriginPro, version 8.5G (Origin Lab Corporation, Northampton, MA, USA). Fluorescence ratios were converted into absolute changes in sodium concentration based on *in situ* calibrations as described in the results (Fig. 1).

To study the effects of metabolic inhibition, slices were bolus-loaded with the magnesium-sensitive fluorescent dye magnesium-green-acetoxymethyl ester (MgG-AM; Life Technologies, Eugene, OR, USA). Changes in the emission of this dye, indicating changes in the intracellular free Mg^{2+} concentration, were used as indication for changes in the intracellular ATP concentration as reported previously (Magistretti & Chatton, 2005).

Data analysis and statistical analysis

To obtain the rate of recovery from intracellular sodium loads, the rate of decline in $[Na^+]_i$ ($-d[Na^+]_i/dt$) from a glutamate-induced sodium load was determined from a

linear fit of the data obtained during 1–2 s after the peak sodium concentration had been reached ($d[Na^+]_i/dt = 0$). This rate of decline ($-d[Na^+]_i/dt$), from now on termed recovery rate V, was plotted *vs.* $[Na^+]_i$ and fitted with a Hill equation $V = V_{max}\,[Na^+]_i^{nHill}/(K_M^{nHill} + [Na^+]_i^{nHill})$ using OriginPro software to derive the maximum sodium recovery rate (V_{max}).

Data are presented as the mean ± SD and the results for the parameters obtained from fitting functions are shown as mean [l.l., u.l.], where l.l. and u.l. represent the lower

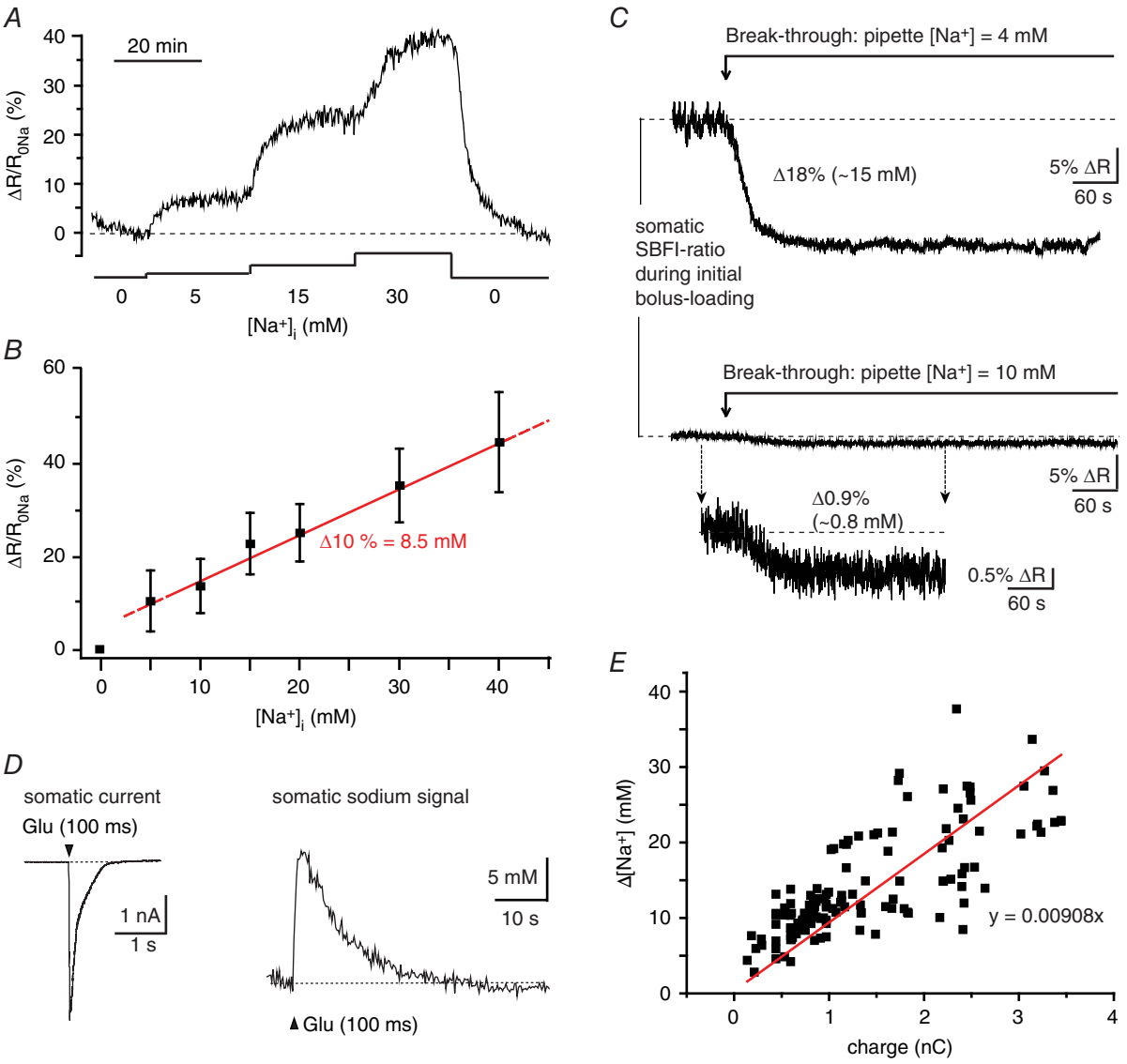

Figure 1. *In situ* calibration of SBFI fluorescence and glutamate-induced sodium signals
A, normalized changes in the fluorescence ratio of SBFI ($\Delta R/R_{0Na}$) in response to changes in the sodium concentration in SBFI-AM loaded cell bodies of CA1 pyramidal neurons ($\Delta R/R_{0Na}$: ratio R at a given $[Na^+]$ minus ratio R at $[Na^+]_i$ = 0 mM (R_{0Na}), divided by R_{0Na} and presented as the percentage change relative to R_{0Na}). Cells were perfused with calibration solutions containing different concentrations of sodium as indicated in addition to gramicidin (3 μM), monensin (10 μM) and ouabain (100 μM). *B*, relationship between normalized changes in SBFI fluorescence ratio ($\Delta R/R_{0Na}$) and $[Na^+]_i$. Data are shown as the mean ± SD. A fit of the data between $[Na^+]_i$ = 10 mM and $[Na^+]_i$ = 40 mM (red line) reveals an almost linear relationship within this range, with a 10% change in ratio corresponding to a change in sodium concentration of ~8.5 mM. *C*, change in the SBFI ratio of a bolus-loaded neuron after obtaining the whole-cell mode with a patch-pipette containing 4 mM Na^+ (upper trace) or 10 mM Na^+ (lower traces). *D*, somatic inward current and sodium transient in a CA1 pyramidal neuron upon pressure application of glutamate (0.5 mM, 100 ms). *E*, relationship between glutamate-induced peak changes in sodium concentration and the charge of the accompanying inward currents as well as a linear fit of the data (red line).

limit and the upper limit of the 95% confidence intervals, respectively. All hypotheses were tested statistically with 95% confidence by one-way ANOVA followed by Tukey's test for multiple comparisons (P represents error probability, n.s., not significant, $^{*}0.01 \leq P < 0.05$, $^{**}0.001 \leq P < 0.01$, $^{***}P < 0.001$). The statistical analysis was performed using Prism, version 6 (GraphPad Software Inc., San Diego, CA, USA).

Experiments were repeated on at least three different slice preparations obtained from at least three different mice; n represents the number of individual sodium signals evaluated; N represents the number of different cells analysed.

Modelling

Simulations were performed with Mathematica, version 10.3 (Wolfram Research; http://www.wolfram.com) by numerically solving a set of coupled ordinary differential reaction diffusion equations (Helmchen & Tank, 2000; Schmidt & Eilers, 2009). The cell soma was represented by a sphere ($r_s = 5\ \mu$m), as calculated for a somatic surface of 300 μm^2, taken from http://neuromorpho.org (Ascoli *et al.* 2007; Beguin *et al.* 2013), which was coupled via diffusion to a cylindrical dendrite ($r_{de} = 0.4\ \mu$m) (Araya *et al.* 2006), divided into three diffusionally coupled compartments with length (l_{de}) of 50 (de1), 20 (de2) and 500 (de3) μm (cf. Fig. 7). All compartments were modelled as well mixed. A Gaussian shaped sodium influx (width 0.5 s) was placed either at the soma or at dendritic compartment de2. The resting concentration of sodium ($[Na]_{rest}$) was set to 13 mM. The diffusional flux (J) between compartments i and j was simulated as:

$$J_{i,j} = (D_{Na}\pi {r_{de}}^2/l_{de})([Na]_i(t) - [Na]_j(t))$$

where D_{Na} is the diffusion coefficient of Na^+ (320 μm^2 s^{-1}).

Sodium dynamics for somatic influx were simulated as:

$$(d[Na]/dt)_s = (\text{Influx} - \text{Pump} - J_{s,de1}/V_s)/(1 + k_B)$$

$$(d[Na]/dt)_{de1} = (-\text{Pump} + J_{s,de1}/V_{de1} - J_{de1,de2}/V_{de1})/(1 + k_B)$$

$$(d[Na]/dt)_{de2} = (-\text{Pump} + J_{de1,de2}/V_{de2} - J_{de2,de3}/V_{de2})/(1 + k_B)$$

$$(d[Na]/dt)_{de3} = (-\text{Pump} + J_{de2,de3}/V_{de3}/V_{de3})/(1 + k_B)$$

where V denotes the volume of the respective compartment and κ_B the buffer capacitance added by the indicator dye (calculated from a K_D of 24 mM and the dye concentration of 1 mM). Sodium dynamics with dendritic influx was simulated correspondingly but with the influx being moved from the soma to de2.

The pump is a sodium clearance mechanism obeying Michaelis–Menten kinetics and is balanced by a 'leak' that keeps the sodium concentration at 13 mM under resting conditions:

$$\text{Pump} = {V_{max}}^* {A_i}/{V_i}^*(([Na]_{rest}/([Na]_{rest} + K_M) - ([Na]_i(t)/[Na]_i(t) + K_M)))$$

where K_M is the Michaelis–Menten constant of 19 mM, A/V is the surface to volume ratio of the ith compartment and V_{max} is the maximum pump velocity of 0.03 mM μm^{-2} s^{-1}. The parameters of the pump were set according to the experimentally obtained values (see Results and Fig. 3), leaving the amplitude of the sodium influx as the only free parameter of the simulation. It was adjusted to match the experimental increases in free sodium concentration of 18– 20 mM.

Results

Quantitative sodium imaging and glutamate-induced sodium signals in CA1 neurons

The goal of the present study was to analyse the mechanisms for recovery from intracellular sodium loads in hippocampal principal neurons *in situ*. To this end, quantitative ratiometric wide-field imaging with the sodium-sensitive fluorescent dye SBFI was performed in somata and apical dendrites of CA1 pyramidal neurons of acute mouse hippocampal tissue slices. SBFI changes its fluorescence properties between a cell-free aqueous solution and intracellular environments (Harootunian *et al.* 1989; Minta & Tsien, 1989), an effect mainly caused by differences in viscosity of the medium (Harootunian *et al.* 1989). For reliable determination of intracellular sodium concentrations ($[Na^+]_i$), we therefore performed *in situ* calibrations of SBFI fluorescence. These essentially consist of recording the changes in the SBFI fluorescence ratio in response to known changes in $[Na^+]_i$.

For calibration, CA1 pyramidal neurons were bolus loaded with SBFI-AM and then subjected to calibration solutions containing different concentrations of sodium, as well as gramicidin (3 μM), monensin (10 μM) and ouabain (100 μM), to enable equilibration of external and internal $[Na^+]$ (Rose & Ransom, 1997; Meier *et al.* 2008). When perfused with these calibration solutions, SBFI fluorescence emission changed in response to changes in sodium concentration when excited at 380 nm (F_{380}; sodium-sensitive wavelength) but remained largely unaltered when excited at 340 nm (F_{340}; sodium-insensitive wavelength; not shown) (see also Fig. 2*A* and *B*) (Langer & Rose, 2009). Changes in the fluorescence ratio of SBFI were normalized to the ratio at $[Na^+]_i = 0$ mM and plotted against the respective sodium concentration ($\Delta R/R_{0Na}$: ratio R at a given $[Na^+]$ minus

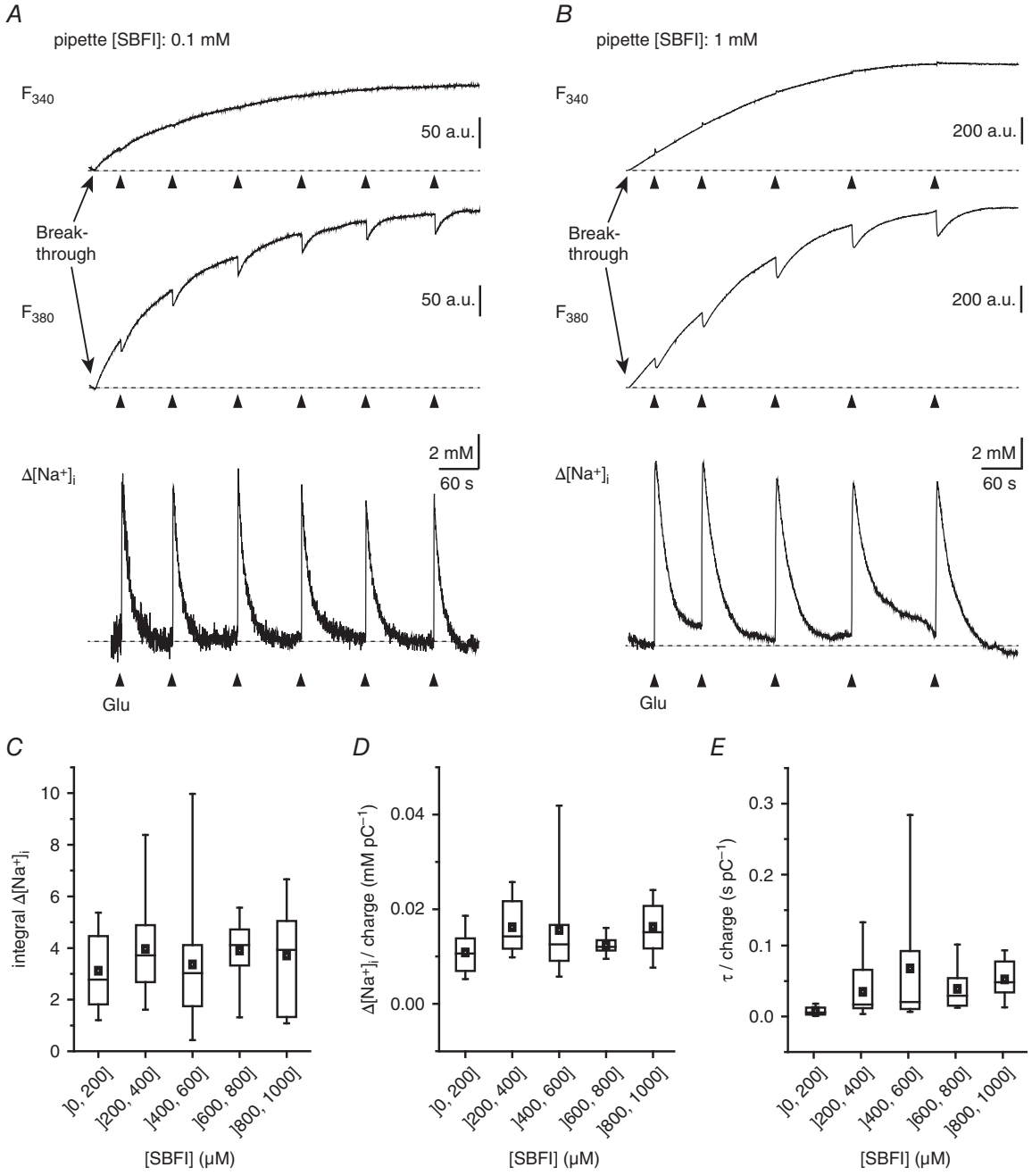

Figure 2. Influence of dye concentration on SBFI signals
A, change in the SBFI fluorescence at 340 nm (F_{340}, top trace) and at 380 nm (F_{380}, centre trace) excitation, as well as the resulting ratio, converted into sodium changes ($\Delta[Na]_i$, lower trace) during dye-loading after obtaining the whole-cell mode with a pipette containing 0.1 mM SBFI. During this phase, glutamate (0.5 mM, 100 ms) was applied repetitively as indicated by the arrowheads. Note that glutamate application does not evoke changes in F_{340}, whereas signals at F_{380} increase in amplitude and the ratio signals remain almost unaltered with increasing dye concentrations. *B*, as described in (*A*) with a pipette containing 1 mM SBFI. Again, glutamate-induced changes in the SBFI ratio are virtually independent from the SBFI concentration. *C*, integrals of the changes in sodium induced by glutamate application as determined at different concentrations of SBFI. Data were pooled for concentrations between 1–200, 201–400, 401–600, 601–800 and 801–1000 μM SBFI as indicated. There is no significant difference between means. *D*, changes in peak sodium concentration ($\Delta[Na^+]_i$) induced by glutamate application, normalized to the charge of the respective inward currents, at different SBFI concentrations as indicated. There is no significant difference between means. *E*, decay time constants (τ) of the recovery phase of glutamate-induced sodium transients, normalized to the charge of the corresponding currents. There is no significant difference between the means. *C*–*E*, boxes represent quartiles; whiskers correspond to 95% confidence interval. Middle lines show the median; squares indicate the mean value.

ratio R at $[Na^+]_i = 0$ mM (R_{0Na}), divided by R_{0Na} and presented as the percentage change relative to R_{0Na}; eight experiments, $N = 54$) (Fig. 1*A*). A linear fit of the data for Na^+ concentrations between 10 and 40 mM ($R^2 = 0.99$) revealed that a change in the ratio by 10% corresponded to change in $[Na^+]_i$ by 8.5 mM (Fig. 1*B*).

During the first 10–15 min after starting perfusion with calibration saline, the tissue experienced swelling. The resulting changes in focus precluded a direct comparison of fluorescence ratio values between physiological and calibration solutions and therefore a proper determination of physiological baseline $[Na^+]_i$ of neurons before switching to calibration salines from these experiments. To determine baseline $[Na^+]_i$, we thus followed an alternative strategy. This approach based on (1) the known linear relationship between changes in SBFI fluorescence ratio and sodium concentration determined by the full calibration in bolus-loaded slices (Figs 1*A* and *B*) and (2) on the assumption that whole-cell patch-clamping a neuron causes equilibration of somatic sodium with the sodium concentration of the patch-pipette.

To this end, neurons were first bolus-loaded with SBFI-AM and the fluorescence ratio was determined in physiological saline. Subsequently, an individual neuron was subjected to whole-cell patch-clamp with an intracellular saline containing 0.1 mM SBFI and either 4 or 10 mM Na^+. This resulted in a change in the SBFI ratio because of equalization of the somatic sodium with that of the pipette saline. Based on the performed *in situ* calibrations (see above), the change in fluorescence ratio after obtaining the whole-cell mode and dilution of the cell with the known pipette $[Na^+]$ was then used to deduce baseline $[Na^+]_i$ in this cell before breakthrough (Fig. 1*C*). These measurements revealed a mean value of 13.4 ± 4.7 mM $[Na^+]_i$ in hippocampal CA1 pyramidal neurons ($n = 6$).

To study intracellular sodium signals and their recovery, CA1 neurons were subjected to whole-cell patch-clamp and loaded with SBFI (0.1–1 mM). Focal pressure application of glutamate (0.5 mM, 100 ms) to the soma resulted in an inward current accompanied by a transient increase in the sodium concentration. The amplitude of sodium transients was linearly correlated ($R^2 = 0.94$) with the total charge of the evoked somatic current ($n = 136$, $N = 33$) (Fig. 1*D* and *E*). Taken together, these results demonstrate that glutamate application reliably evokes sodium transients in somata of CA1 pyramidal neurons, the amplitude of which depends on the induced inward current.

Influence of dye concentration

Compared to other ion-selective fluorescent dyes (e.g. Fura-2), SBFI exhibits a minor quantum efficiency and a low signal-to-noise ratio, necessitating the use of rather high dye concentrations (between 0.5 and 1 mM) when loaded through a patch-pipette (Schreiner & Rose, 2012). To determine whether the addition of such SBFI concentrations induces any detectable buffering and distortion of intracellular sodium signals, we employed the 'added buffer approach' (Neher, 1995; Helmchen *et al.* 1996). To this end, neurons were subjected to whole-cell patch-clamp with intracellular salines containing SBFI concentrations ranging from 0.1 (Fig. 2*A*) to 1 mM (Fig. 2*B*).

After rupturing the patch, SBFI diffused from the pipette into the soma and the resulting increase in fluorescence emission from the soma was monitored at both excitation wavelengths (F_{340}, F_{380}) until a stable maximum was reached, indicating full equilibration with the pipette saline (Fig. 2*A* and *B*). During this loading phase, which took ~10 min, glutamate (0.5 mM, 100 ms) was repetitively applied to the soma, resulting in transient changes in the F_{380}, the amplitude of which increased with increasing dye concentration (Fig. 2*A* and *B*) ($N = 33$). By contrast, the signals as depicted in fluorescence ratio R ($F_{340/380}$) were unaltered in amplitude and time course during the loading phase (Fig. 2*A* and *B*). The SBFI concentration did not significantly influence the integral of the sodium signals (Fig. 2*C*) and, after normalization of the signals to the charge of the accompanying inward currents, no difference was seen in their peak amplitudes (Fig. 2*D*), nor decay time constants (Fig. 2*E*) with SBFI concentrations of up to 1 mM.

In summary, these results establish that the presence of the sodium indicator SBFI in concentrations of up to 1 mM does not visibly distort sodium signals as reported by its fluorescence ratio. Furthermore, glutamate-induced sodium signals can be evoked reliably and repetitively in a given cell without significant alteration in their amplitude or time course.

Sodium extrusion from somata

To study the properties of sodium extrusion from cell bodies, CA1 pyramidal neurons were subjected to whole-cell patch-clamp and loaded with SBFI though the patch-pipette. Sodium signals were induced by focal pressure application of glutamate (0.5 mM, 100 ms) close (5–10 μm) to the soma (Fig. 3*A*). The rate of recovery from intracellular sodium loads V (mM min^{-1}) was determined by a linear plot of the data points between 1 and 2 s after the peak sodium concentration had been reached, representing the phase of the steepest decline of the recovery from a glutamate-induced sodium increase (Fig. 3*A*).

When glutamate was applied to the soma in the whole-cell mode, which is with the patch-pipette still attached (Fig. 3*A*), the recovery from somatic sodium loads followed a mono-exponential decay as described before (Fig. 1*D*), exhibiting decay time constants of

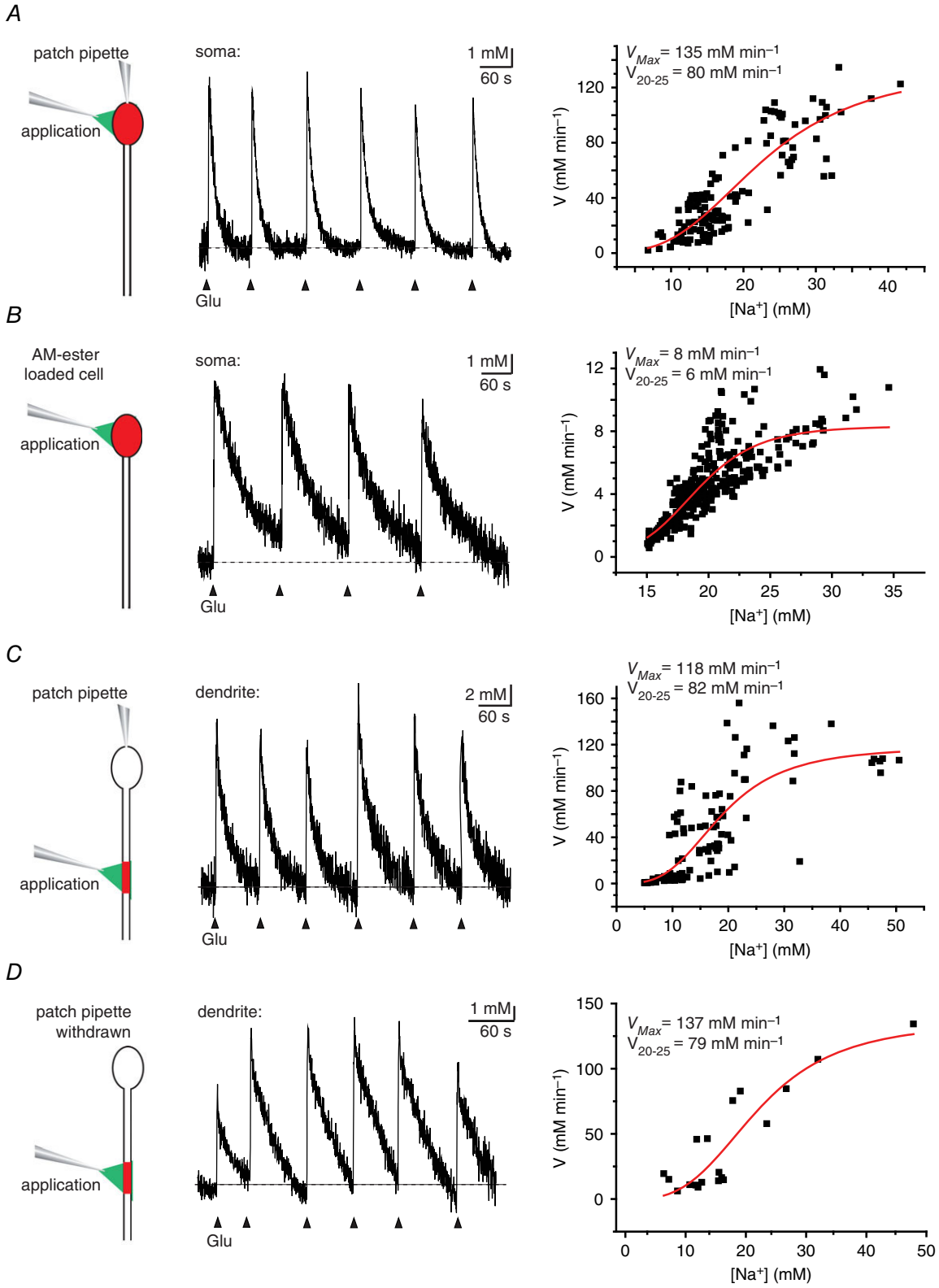

Figure 3. Recovery from sodium loads in cell bodies and dendrites
A, left: scheme of the experimental design: a neuron was held in the whole-cell patch-clamp mode, glutamate was focally applied to the soma (as indicated by the green area) and sodium signals were measured from the soma (as indicated by the red area). Centre: somatic sodium signals evoked by repetitive glutamate application to the soma as indicated by the arrowheads. Right: relationship between sodium concentration and decay velocity

τ ~20 s. Because cellular sodium export is expected to be mediated by the NKA, which follows a Michaelis–Menten relationship (Munzer *et al.* 1994; Zahler *et al.* 1997), rates of V were plotted against the respective peak sodium concentrations and fitted using a Hill equation to derive V_{max}, representing the maximum rate for recovery from sodium loads. Under this condition, V_{max} was 134.8 (93.8, 175.7) mM min^{-1} (Fig. 3*A*).

To evaluate the influence of sodium diffusion into the patch pipette on recovery characteristics, we next loaded cells by bolus injection of SBFI-AM and again applied glutamate to the soma (Fig. 3*B*). Somatic sodium signals now exhibited a strikingly slower decay ($\tau = 63.5 \pm 48.7$ s) and V_{max} was only 8.3 (7.7, 9.0) mM min^{-1} ($n = 297$, $N = 61$) (Fig. 3*B*). Assuming that this recovery is solely mediated by sodium transport across the membrane, this represents a sodium efflux of 0.028 ± 0.001 mM min^{-1} μm^{-2} (average somatic surface area 300 μm^2; data taken from http://neuromorpho.org) (Ascoli *et al.* 2007; Beguin *et al.* 2013), The apparent K_M as retrieved from the Hill plot was 19.0 (18.4, 19.5) mM. This latter value denotes that the pump is half-maximally activated at an intracellular sodium concentration of 19 mM, and thus (at an intracellular baseline sodium concentration of ~13 mM) by sodium increases of ~6 mM. Saturation was reached at ~ 30 mM, suggesting that the pump rate is no longer dependent on the amplitude of sodium increases if these exceed ~17 mM.

The large difference in V_{max} between cells held in the whole-cell mode and bolus-loaded cells strongly indicated that the recovery from sodium loads was dominated by sodium diffusion from the cell body into the pipette in patch-clamped cells. In the latter, determination of V_{max}, which should describe enzymatic NKA activity, was therefore meaningless. We thus additionally calculated the average sodium recovery rate for concentrations between 20 and 25 mM, $V_{20–25}$, to enable meaningful comparison between the different conditions. In whole-cell patch-clamped cells, $V_{20–25}$ was 79.9 ± 30.5 mM min^{-1} ($n = 12$, $N = 5$) (Fig. 3*A*), whereas it amounted to 6.1 ± 1.7 mM min^{-1} in bolus-loaded neurons ($n = 108$, $N = 32$) (Fig. 3*B*), again emphasizing the strong influence of sodium diffusion into the pipette.

Taken together, these results suggest that the recovery from somatic sodium transients in whole-cell patch-clamped cells is largely governed by fast diffusion of sodium into the patch-pipette that, if it contains a saline with a low sodium concentration, serves as an infinite sink for sodium. In the undisturbed situation, recovery from somatic sodium transients is considerably slower and the maximum sodium recovery rate more than 15-fold lower, reaching ~8 mM min^{-1}. Under this assumption that recovery is solely mediated by NKA activity under the latter condition, this corresponds to a maximum sodium extrusion rate of ~0.03 mM min^{-1} μm^{-2}.

Sodium extrusion from dendrites

To determine the sodium recovery rates from dendrites, cells were loaded with SBFI through a patch pipette. For stimulation of dendrites, application pipettes were positioned such that their tip pointed towards a spot on the dendrite which was ~50 μm away from the soma. With given settings for pressure application, a dendritic section of ~20 μm in length was directly exposed to the ejection stream and ROIs were accordingly placed (representing a dendritic segment of ~20 μm in length) (Fig. 3*C*). Focal application of glutamate (0.5 mM, 100 ms) close (~5–10 μm) to the dendrite resulted in sodium transients that decayed with a time constant of $\tau = 21.5 \pm 14.4$ s. V_{max} was 118.4 (92.9, 143.9) mM min^{-1} ($n = 110$, $N = 10$) and $V_{20–25}$ was 81.5 ± 45 mM min^{-1} ($n = 12$, $N = 5$) (Fig. 3*C*).

Loading with SBFI-AM does not result in sufficiently high dye concentrations and tolerable signal-to-noise ratio in dendrites, and such measurements were thus not feasible. Instead, we therefore filled a neuron through a patch-pipette, which was then withdrawn carefully. After resealing of the cell, we applied glutamate to the dendrite as described before. Under this condition, the decay time constant was $\tau = 20.3 \pm 17.8$ s; V_{max} was 137.1 (115.1, 159.3) mM min^{-1} ($n = 20$, $N = 4$ cells) and $V_{20–25}$ amounted to 79.1 ± 19.2 mM min^{-1} ($n = 3$ signals from three cells). The apparent K_M under this condition was 18.5 (15.8, 21.2) mM ($n = 20$, $N = 4$ cells) (Fig. 3*D*), a value close to the one obtained in the soma (see above). Thus, in

(*V*) as obtained during the first few seconds after the sodium peak. The data were fitted with a Hill equation, the results for V_{max} and $V_{20–25}$ are indicated. *B*, as described in (*A*) but with AM-ester loaded neurons (no patch-pipette attached). V_{max} and $V_{20–25}$ were strongly reduced under this condition. *C*, left: scheme of the experimental design: a neuron was held in the whole-cell patch-clamp mode, glutamate was focally applied to the dendrite (as indicated by the green area) and sodium signals were measured from a section of the dendrite (as indicated by the red area). Centre: dendritic sodium signals evoked by repetitive glutamate application as indicated by the arrowheads. Right: relationship between sodium concentration and decay velocity (*V*) as obtained during the first few seconds after the sodium peak. The data were fitted with a Hill equation, the results for V_{max} and $V_{20–25}$ are indicated. *D*, as described in (*C*) but, in this case, the patch pipette was carefully retracted after loading with SBFI and the cell was allowed to reseal. Values obtained for V_{max} and $V_{20–25}$ were similar to those acquired under the same conditions but with the pipette attached.

the dendrite, recovery was not significantly influenced by the presence of the whole-cell patch-pipette in the soma.

These data thus reveal that recovery from local sodium transients in dendrites is much faster compared to the soma and V_{max} is more than 10-fold higher. The apparent K_M was similar in both compartments, indicating that the sensitivity of the NKA to sodium increases is similar in both compartments.

Influence of sodium extrusion through NKA

Our experiments so far showed that the recovery from local sodium loads is considerably faster in dendrites than in the soma. To analyse the mechanisms of sodium extrusion from these two compartments, we bath-applied ouabain (100 μM), a specific blocker of the NKA. Somatic sodium signals were studied in cells bolus-loaded with SBFI-AM. For measurement of dendritic sodium signals, neurons were subjected to whole-cell patch-clamp with a pipette saline containing 1 mM SBFI. After dye loading, cells were perfused with physiological saline and baseline sodium determined before switching to saline containing ouabain (Fig. 4*A* and *B*).

Within 1–2 min after starting the ouabain application, somatic sodium began to rise by 1.8 ± 0.6 mM min^{-1} (n = 86 cells), a value that is in accordance with earlier work (Rose & Ransom, 1997; Despa *et al.* 2002). For an average somatic surface area of 300 μm^2 (Ascoli *et al.* 2007; Beguin *et al.* 2013), this value corresponded to a sodium flux of 0.006 ± 0.002 mM min^{-1} μm^{-2}. In dendrites, ouabain caused a sodium increase by 0.5 ± 0.1 mM min^{-1} (n = 8 cells). For an average dendrite diameter of

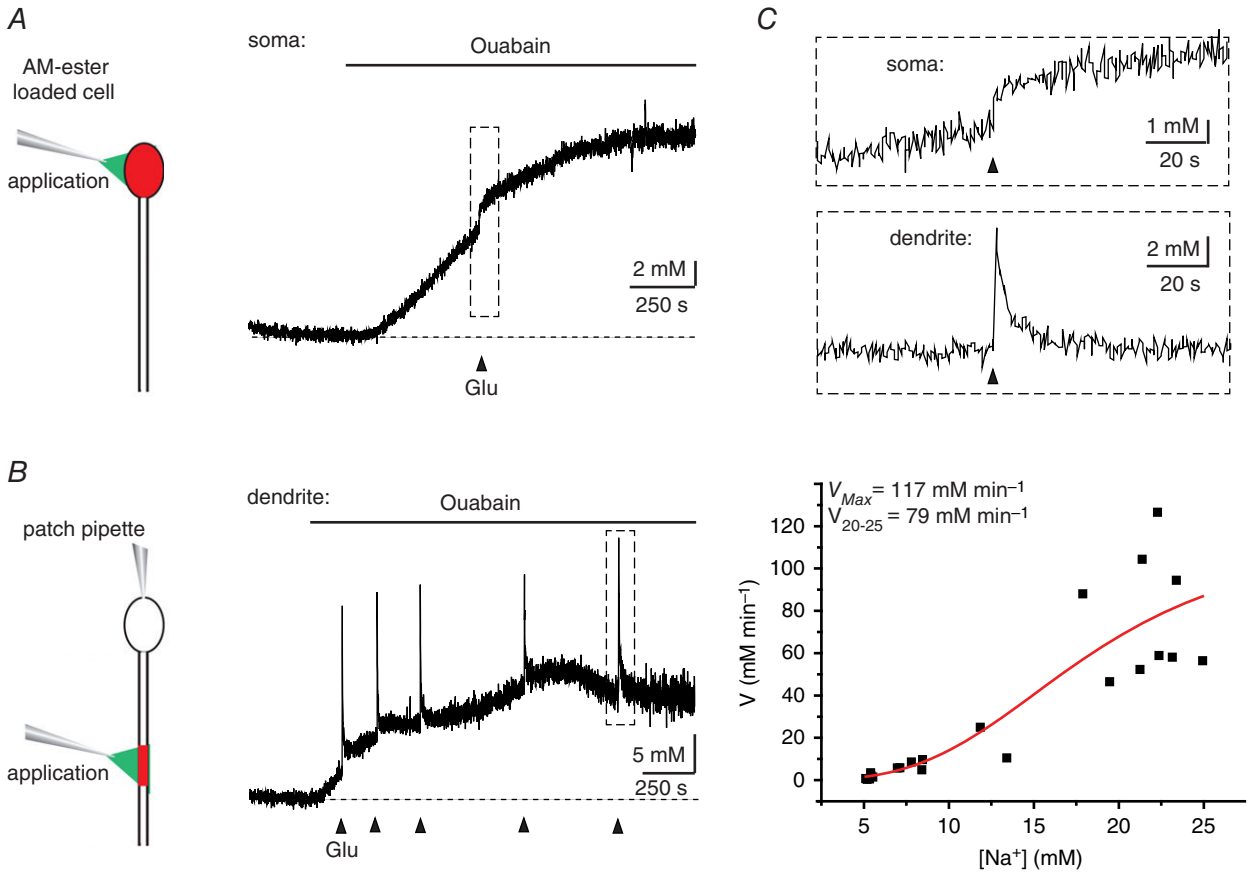

Figure 4. Role of NKA on recovery from sodium loads
A, left: scheme of the experimental design: glutamate was focally applied to the soma (green area) and sodium signals were measured from the soma as indicated by the red area in a bolus-loaded neuron. Right: changes in somatic sodium concentration upon perfusion with the NKA inhibitor ouabain (100 μM) as indicated by the bar. During perfusion with ouabain, glutamate was pressure-applied (0.5 mM, 100 ms) as indicated by the arrowhead. The area indicated by the dotted box is shown enlarged in (*C*). *B*, as described in (*A*) but with focal glutamate application to the dendrite and measurement of dendritic sodium signals. Note that dendritic sodium transients still recover in the presence of ouabain. Right: relationship between sodium concentration and decay velocity (*V*) as obtained during the first few seconds after the sodium peak. The data were fitted with a Hill equation (red curve). *C*, glutamate-induced sodium signals as shown in (*A*) (dotted area, top trace) and (*B*) (dotted area, bottom trace) at an enlarged time scale.

0.75 μm (Araya *et al.* 2006) and a surface of 47.1 μm^{-2}, this corresponds to a sodium flux of 0.01 mM min^{-1} μm^{-2}. These values indicate that basal pump rates and constitutive sodium influx are in the same range in both compartments. In soma, as well as in dendrites, sodium kept increasing until a plateau of 40–50 mM was reached (Fig. 4*A* and *B*).

To evoke local sodium signals, glutamate was focally pressure applied either close to the soma (Fig. 4*A*) or close to the primary dendrite (Fig. 4*B*). In the presence of ouabain, glutamate-evoked sodium increases in somata added to the strong on-going increase in 'baseline' sodium ($n = 22$) (Fig. 4*A* and *C*). Recovery from glutamate-induced sodium loads was not observed and sodium levels just continued to rise until the plateau was reached (Fig. 4*A* and *C*). Thus, in the presence of ouabain, sodium extrusion from the soma was completely blocked.

In dendrites, the situation was quite different. Here, glutamate application, in the presence of ouabain, evoked sodium transients that recovered quickly on the top of the on-going increase in baseline sodium ($n = 22$) (Fig. 4*B* and *C*). Measuring the maximal slope, plotting it against the sodium concentration and fitting it with a Hill equation (Fig. 4*B*) revealed a V_{max} of 116.8 (96.6, 136.9) mM min^{-1} and $V_{20–25}$ amounted to 78.7 ± 29.5 mM min^{-1} ($n = 7$ signals, $N = 3$ cells). These values were quite similar to those obtained in the absence of ouabain (Fig. 3*C*). Thus, although inhibition of the NKA blocked sodium extrusion from the soma completely, local sodium increases in dendrites recovered with essentially the same speed as under control conditions.

These results strongly indicate that NKA activity is not *per se* required for the recovery from local sodium loads in dendrites. An additional pathway in this compartment might be diffusion of sodium into neighbouring, non-stimulated regions.

NKA activity *vs.* diffusion

To test for the role of diffusion in recovery from glutamate-induced sodium transients, we performed experiments in which glutamate was pressure-applied with a wide-tip pipette, resulting in non-focal stimulation of essentially the entire cell (Fig. 5*A*). Under this condition, the recovery from sodium signals as determined in the dendrite was dramatically slowed. V_{max} was reduced to 15.5 (12.8, 18.1) mM min^{-1} ($n = 25$, $N = 7$ cells) and $V_{20–25}$ to 15.7 ± 1.8 mM min^{-1} ($n = 3$, $N = 3$) (Fig. 5*A*). Maximum dendritic sodium efflux thus amounted to 0.33 ± 0.03 mM min^{-1} μm^{-2}. The Hill plot revealed an apparent K_M of 15.4 mM and a saturation of pump activity at ~30 mM. Although flux rates thus differed by a factor of ~10 compared to the soma, dendritic values for V_{max}, K_M and saturation were similar to somatic ones (Fig. 3*B*), indicating a similar sodium sensitivity of the NKA in both compartments.

To obtain further evidence for the differential influence of NKA activity on the recovery from local sodium transients in soma *vs.* dendrites, we performed experiments at near physiological temperature (34°C). Switching to 34°C caused an acceleration of the initial recovery rate from glutamate-induced sodium transients by a factor of 2.56 in somata, resulting in a Q_{10} of 1.97 ($n = 36$, $N = 4$) (Fig. 5*B*). With local application of glutamate to dendrites, in contrast, recovery was unaltered when switching to high temperature ($Q_{10} = 0.94$; $n = 8$, $N = 8$ for both temperatures) (Fig. 5*C*).

We next probed for lateral diffusion of sodium along dendrites. To this end, we performed experiments in which glutamate was applied focally to a dendrite and resulting sodium transients were determined in two to three different dendritic ROIs: one ROI located directly within the ejection stream of the pressure application pipette, and further ROIs positioned more proximal to the soma ($n = 17$, $N = 3$) (Fig. 5*D*). As observed before, a fast rise in sodium followed by a mono-exponential recovery phase was detected close to the application pipette. In dendritic regions located further away from the stimulation pipette, rise times increased, peak amplitudes decreased and the delay between the stimulation events and peaks increased (Fig. 5*D*). Based on the assumption that this phenomenon was largely a result of the intracellular diffusion of sodium, its apparent diffusion coefficient was calculated. To this end, the distance between the two ROIs was determined using the centre of each as anchor point. The delay between peak sodium concentrations was determined and the parameters time and distance were introduced in the one-dimensional diffusion equation ($D \sim x^2/2t$), resulting in a D_{Na+} of 328 ± 20 μm^2 s^{-1} for sodium diffusion along dendrites ($n = 17$; $N = 3$).

Finally, we probed for diffusion of sodium from somata into dendrites. To this end, glutamate was applied locally to the cell body of a patch-clamped cell and a region of interest set on the dendrite. Upon glutamate application, sodium transients were also detected in dendrites ($n = 4$, $N = 4$) (Fig. 5*E*). These, however, exhibited slow rise times, small amplitudes and blunted peaks, indicating that they were mostly a result of the diffusion of sodium from out of the soma along the dendrites.

Taken together, these results suggest that, although the NKA is the major mechanism responsible for the recovery from sodium loads from cell bodies, lateral diffusion is the predominant pathway for the recovery from local sodium increases in dendrites. Also, lateral diffusion provides for a much faster sodium extrusion from dendrites with a more than 10-fold higher rate compared to NKA-mediated extrusion observed in the soma.

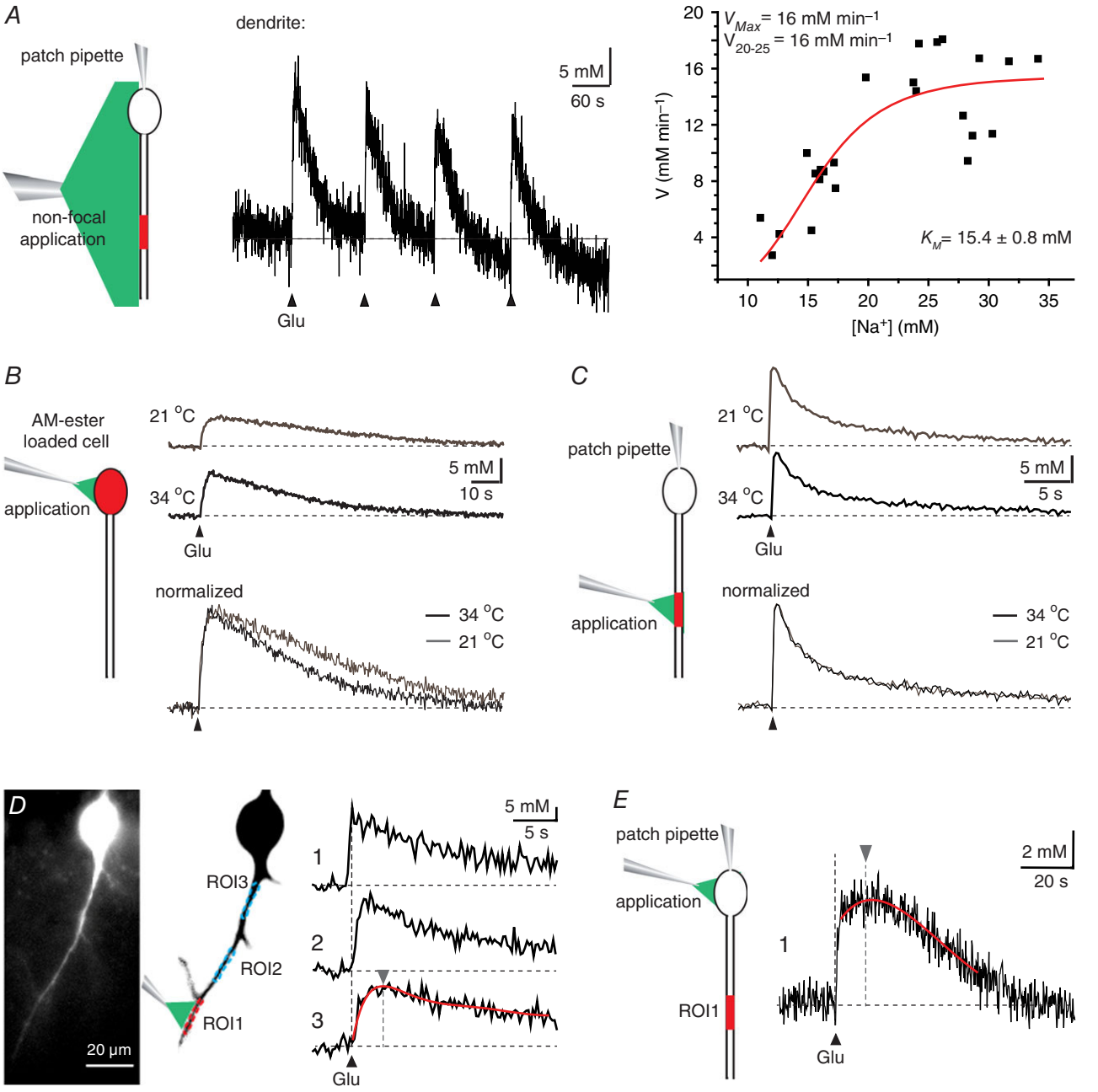

Figure 5. Role of diffusion on recovery from sodium loads
A, left: scheme of the experimental design: glutamate was applied non-focally with a wide-tip pipette and the sodium signals were measured in the dendrite (red area). Centre: changes in dendritic sodium concentration upon glutamate application. Right: relationship between sodium concentration and decay velocity (*V*) as obtained during the first few seconds after the sodium peak. The data were fitted with a Hill equation, the results for V_{max} and $V_{20–25}$ are indicated. *B*, left: scheme of the experimental design: glutamate was focally applied to the soma (green area) and sodium signals were measured in the soma as indicated by the red area. Top right: changes in somatic sodium concentration at room temperature (21°C) compared to 34°C. Bottom right: overlay of the sodium transients with amplitudes normalized. *C*, left: scheme of the experimental design: glutamate was focally applied to the dendrite (green area) and sodium signals were measured as indicated by the red area. Top right: changes in dendritic sodium concentration at room temperature (21°C) compared to 34°C. Bottom right: overlay of the sodium transients with amplitudes normalized. *D*, left: wide-field-fluorescence image of a pyramidal neuron, filled with SBFI through a patch-pipette. Both soma and primary dendrite are clearly visible. Centre: inverted image indicating regions of interest and position of glutamate application pipette for experiment shown on the right. Right: dendritic sodium transients induced by brief glutamate application (arrowhead) close to the stimulation

Recovery from sodium loads under conditions of energy deprivation

Whereas diffusion is only dependent on the existence of ion gradients and does not primarily break down energy, NKA activity is a major energy consumer in neural cells. Consequently, and based on our results obtained so far, reduction of cellular ATP levels should not have an immediate impact on the recovery of local sodium transients in dendrites, but should strongly affect sodium extrusion from somata.

To test this hypothesis, we perfused slices with saline containing 4 mM sodium fluoride (NaF). NaF decreases cellular pyruvate and ATP levels by inhibition of enolase, which catalyses the second to last step of the glycolysis (Cox & Bachelard, 1982; Lees, 1991; Bizzozero *et al.* 1999). To gain evidence that NaF resulted in a decrease in neuronal ATP concentration in our preparation, we monitored changes in intracellular free Mg^{2+} concentration using the fluorescent indicator dye MgG, as described previously (Chatton *et al.* 2003; Magistretti & Chatton, 2005; Fernandez-Moncada & Barros, 2014). Free magnesium provides an indirect evaluation of intracellular ATP levels because ATP exhibits ∼10-fold higher affinity for Mg^{2+} than ADP and binds a large proportion of cellular magnesium (Leyssens *et al.* 1996). To this end, neurons were bolus-loaded with MgG-AM and baseline fluorescence was monitored before adding NaF.

Upon perfusion with NaF, MgG fluorescence emission started to increase until it reached a stable level, which was 25 ± 21% higher than the initial baseline fluorescence, indicating an increase in the intracellular free magnesium concentration ($n = 11$; $N = 3$) (Fig. 6*A*). Removal of extracellular magnesium during this phase caused a drop in MgG fluorescence by 10 ± 7% ($n = 12$, $N = 3$) (Fig. 6*A*). Although this suggests that influx of magnesium from the extracellular space might have contributed to the NaF-induced increase, this result also demonstrated that the greater part of the signal was the result of an intracellular magnesium source, most probably its unbinding from ATP in the course of a decrease in intracellular ATP levels.

To analyse recovery from sodium loads under this condition, neurons were filled with SBFI via a patch pipette upon which the pipette was carefully retracted. After resealing of the cell, slices were perfused with NaF for 20 min and then subjected, repetitively, to puffs of glutamate to evoke sodium transients. When glutamate was focally pressure-applied to the soma, the first one to two applications to neuronal somata resulted in well detectable sodium transients with an average amplitude of 4.8 ± 2.5 mM ($[Na^+]_i$ = 18.3 ± 2.5 mM). Sodium transients recovered only slightly slower than those in the same range of concentrations under control conditions [maximum rate in the absence of NaF: 3.7 ± 1.5 mM min^{-1} ($n = 192$, $N = 50$); at 20 min of NaF perfusion: 3.2 ± 2.0 mM min^{-1} ($n = 72$, $N = 28$)] (Fig. 6*B*). However, with repeated glutamate application, peak amplitudes decreased, recovery slowed and sodium started to accumulate (Fig. 6*B*). Accordingly, the somatic recovery rate dropped to 1.0 ± 1.0 mM min^{-1} after 25 min in the presence of NaF ($n = 133$, $N = 36$) (Fig. 6*B*).

Again, the situation was completely different when glutamate was locally applied to dendrites. Here, and as observed before, recovery from sodium loads was much faster than in the soma (rate at the same range of sodium concentrations (14.2 ± 1.8 mM) was 35.5 ± 25.9 mM min^{-1} in the control ($n = 13$, $N = 8$) (Fig. 6*C*). Moreover, transients remained largely unaltered even in continued presence of NaF and no increase in the sodium baseline was seen [extrusion rate: 26.9 ± 19.5 mM min^{-1} after 20 min ($n = 6$, $N = 3$) and 28.8 ± 13.7 mM min^{-1} after 25 min ($n = 12$, $N = 3$)] (Fig. 6*C*).

Finally, we repeated these experiments with non-focal application of glutamate to evoke sodium transients throughout the entire cell, preventing the generation of intracellular sodium concentration gradients and diffusion. As opposed to focal glutamate application in the presence of NaF, dendritic sodium transients now dramatically changed with repeated stimulation and an increase in baseline sodium was observed ($n = 9$, $N = 3$) (Fig. 6*D*). Although the recovery rate was 26.8 ± 23.8 mM min^{-1} after 20 min of NaF perfusion ($n = 9$), it dropped significantly to 4.9 ± 7.7 mM min^{-1} after 30 min ($n = 6$) (Fig. 6*D*).

Taken together, our data show that impairment of energy metabolism significantly influences the recovery from sodium transients in the soma, in agreement with the demonstrated main role of NKA, and its dependence on cellular ATP, for sodium extrusion. In dendrites, in contrast, recovery from local sodium loads is unaffected by periods of up to 30 min of metabolic impairment, supporting its independence on ATP on this time frame and emphasizing the predominant role of sodium diffusion in this process.

pipette (ROI1) and more proximal to the soma (ROI2 and 3, respectively). Sodium signals in ROI2 and 3 are delayed, reduced in amplitude and exhibit slower kinetics than those in ROI1, indicating sodium diffusion. The red line represents a curve fit of the data to reveal the peak. *E*, left: scheme of the experimental design: glutamate was focally applied to the soma (green area) and sodium signals were measured in the dendrite as indicated by the red area. Right: changes in dendritic sodium concentration upon application of glutamate to the soma. The red line represents a curve fit of the data to reveal the peak.

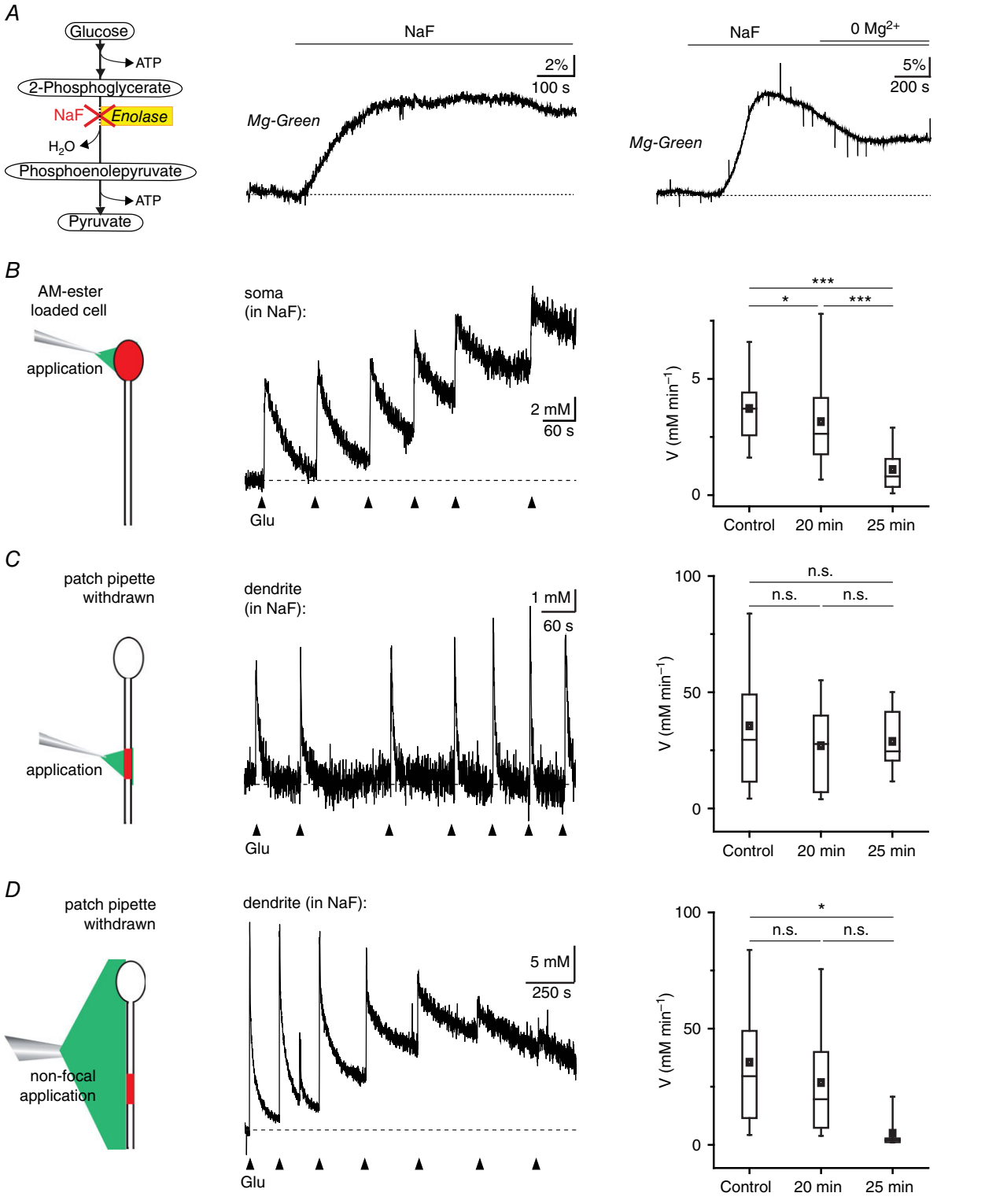

Figure 6. Sodium extrusion under metabolic stress
A, left: schematic drawing indicating mechanism of inhibition of glycolysis by NaF. Centre: increase in Mg-Green fluorescence relative to baseline fluorescence upon bath perfusion with NaF as indicated by the bar. Right: changes in MgG fluorescence induced by bath perfusion with NaF and during additional removal of extracellular magnesium (0 Mg^{2+}) as indicated by the bars. *B*, left: scheme of the experimental design: glutamate was focally applied to the soma and sodium signals were measured from the soma as indicated by the red area in a neuron loaded with SBFI-AM. Centre: somatic sodium concentration recorded 20 min after starting perfusion with the

Numerical modelling of somatic and dendritic Na^+ extrusion

To test the validity of our experimental findings, we applied a numerical simulation (see Methods), employing the parameters for NKA pump rate, K_M, sodium flux and diffusion determined experimentally. Sodium influx was first placed onto the soma to obtain an increase by ~18–20 mM in this compartment (Fig. 7*A*, left). With NKA active, somatic sodium recovered mono-exponentially from this increase. In addition, diffusion-based sodium increases developed in the two adjacent dendritic segments, whereas, in the third (quasi infinite) dendritic compartment, almost no sodium increase occurred

glycolysis inhibitor NaF. Arrowheads indicate repetitive focal application of glutamate (0.5 mM, 100 ms) to the soma. Right: sodium extrusion rate (*V*) as determined during the first few seconds after the sodium peak under control conditions and 20 and 25 min after starting perfusion with NaF. *C*, as in (*B*) but with focal glutamate applications in the proximity of the dendrite and recorded in the red area; the patch pipette was retracted from the soma. There is no significant difference in extrusion rates between control and after perfusion with NaF. *D*, as in (*C*) but glutamate was applied to a large area of a cell. *B*–*D*, boxes represent quartiles, whiskers correspond to the 95% confidence interval. Middle lines show the median and squares the mean value. n.s., not significant, $^*0.01 \leq P < 0.05$, $^{***}P < 0.001$.

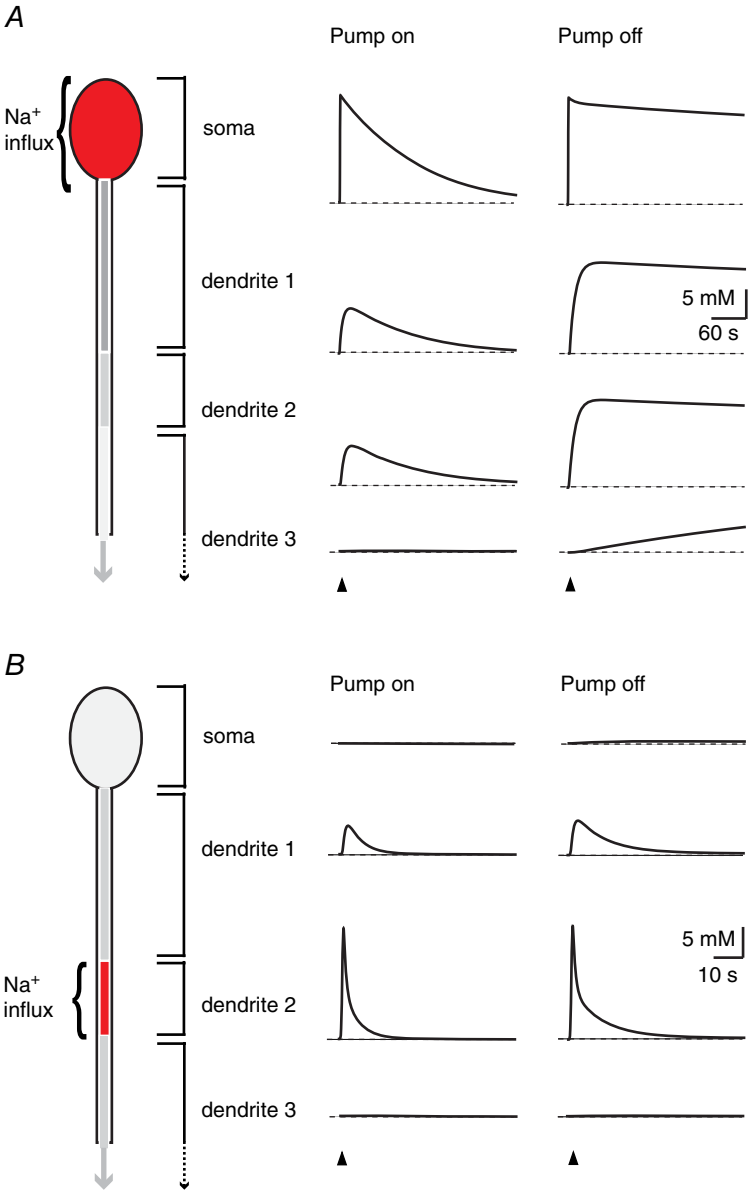

Figure 7. Numerical simulation of sodium recovery
A, left: scheme of the simulated experiment: sodium influx was placed on the soma (indicated by red area) which was coupled to a dendrite that was divided into three compartments of 50, 20 and 500 μm in length as indicated. Right: changes in sodium concentrations in the different compartments with NKA on (left) or turned off (right). *B*, left: scheme of the simulated experiment: sodium influx was placed on the second dendritic segment (indicated by red area). Right: changes in sodium concentrations in the different compartments with NKA on (left) or turned off (right).

(Fig. 7*A*, left). Recovery from the somatic sodium load was strongly dependent on NKA. With pumps turned off, sodium recovery towards baseline was extremely slowed in the soma and the two adjacent dendritic compartments, accompanied by a slow sodium increase in the third dendritic compartment (Fig. 7*A*, right).

Next, sodium influx was placed on the second dendritic compartment to mimic the local application of glutamate onto this compartment. Dendrites recovered quickly from this sodium load, and sodium diffusion resulted in a detectable increase in the neighbouring proximal dendritic compartment (Fig. 7*B*, left). By stark contrast to what was seen in the soma, dendritic sodium also recovered efficiently with pumps turned off, albeit recovery was slowed especially in the later phase (Fig. 7*B*, right).

In summary, these simulations support our conclusion that NKA-mediated extrusion is critical for recovery from somatic sodium loads. Although diffusion of sodium from the soma into the proximal apical dendrite is visible, it does not mediate efficient clearance of somatic sodium when NKA is blocked. On the other hand, diffusion is the dominating mechanism for the initial fast recovery from local sodium loads from dendrites, whereas NKA-mediated extrusion shapes and accelerates recovery at later phases.

Discussion

Using ratiometric imaging with the sodium indicator SBFI, we demonstrate that local puff application of glutamate induces transient sodium increases in mouse CA1 pyramidal neurons. Glutamate-evoked changes in sodium as reported by SBFI are not dependent on the concentration of the dye, demonstrating that it does not visibly buffer, nor distort sodium transients. Recovery from somatic sodium transients followed a mono-exponential time course. A Hill plot revealed a maximum sodium recovery rate of 8 mM min^{-1}, corresponding to a flux of 0.03 mM min^{-1} μm^{-2}, and an apparent K_M of 19 mM. Somatic sodium extrusion was completely blocked in the presence of the NKA blocker ouabain and significantly hampered upon inhibition of glycolysis by NaF. In addition, somatic recovery rates were doubled by an increase in temperature by 10°C. In dendrites, maximum sodium recovery rates were more than 10-fold faster than in the soma with local glutamate application. Moreover, dendritic recovery was largely unaltered at elevated temperature and, in the time frame studied, by ouabain or during inhibition of glycolysis. With non-focal application of glutamate, in contrast, dendritic sodium recovery rates were reduced to those found in the soma and were diminished during application of NaF. Numerical modelling supports the conclusion that NKA activity is required for recovery from somatic sodium loads, whereas diffusion is the dominating mechanism for recovery from local sodium loads in dendrites.

SBFI as a reporter of intracellular sodium concentration

Ratiometric imaging with SBFI is a reliable tool for the quantitative measurement of intracellular sodium concentrations (Minta & Tsien, 1989; Levi *et al.* 1994; Rose & Ransom, 1997; Chatton *et al.* 2000; Diarra *et al.* 2001). Although the relationship between SBFI fluorescence and sodium concentration generally follows Michaelis–Menten kinetics (Donoso *et al.* 1992; Rose *et al.* 1999), there is an acceptable linear correlation in the concentration range between ~5 and 40 mM, as reported previously (Meier *et al.* 2006) and in the present study. Within this concentration range, such linearization enables the calculation of absolute changes in sodium concentration without the need to know the baseline concentration of each individual cell (and cellular compartment, respectively).

In the present study, we also employed a new approach for the determination of baseline sodium concentration in cell bodies of CA1 neurons. By comparing SBFI ratio levels before and after loading the cell with a known sodium concentration through dialysis with the intracellular saline of a patch-pipette, we obtained a value of ~13 mM, which is in good accordance with earlier studies (Donoso *et al.* 1992; Langer & Rose, 2009; Kelly & Rose, 2010*a*; Azarias *et al.* 2012; Karus *et al.* 2015*a*). Chemical ion indicator dyes bind an ion of choice selectively and therefore may exert a buffering effect which distorts ion signals. This is especially relevant for high-affinity calcium indicator dyes such as Fura-2 or Oregon-Green (Neher & Augustine, 1992; Zhou & Neher, 1993; Maravall *et al.* 2000). SBFI has a K_D of ~24 mM (Donoso *et al.* 1992; Jung *et al.* 1992; Rose *et al.* 1999; Sheldon *et al.* 2004; Meier *et al.* 2006). Relevant buffering of sodium is therefore not expected because applicable dye concentrations (0.1–1 mM) are far below this value (Sabatini *et al.* 2001). However, because this has not yet been confirmed experimentally, we tested this theoretical prediction by investigating whether glutamate-induced sodium signals were altered during loading of the dye to concentrations of up to 1 mM, an approach that has been introduced previously (Neher, 1995; Helmchen *et al.* 1996). Although the amplitudes of single-wavelength fluorescence emission signals (F_{380}) increased with increasing dye concentrations, the calculated ratio signals ($F_{340/380}$) were not altered. Our data thus clearly demonstrate that the presence of SBFI does not imply a relevant distortion of intracellular sodium transients, a finding that is of critical importance for the correct interpretation of the further results of the present study.

Sodium extrusion from somata

To study extrusion of sodium in neurons, we imposed transient intracellular sodium increases by puff application of glutamate, which results in influx of sodium through AMPA and NMDA receptor channels (Rose & Konnerth, 2001; Lamy & Chatton, 2011). As reported previously (Rose *et al.* 1999; Bennay *et al.* 2008), recovery from transient sodium loads followed a mono-exponential decay and was characterized by large decay time constants. In whole-cell patch-clamped cells, the maximum velocity at which sodium recovered was ∼135 mM min^{-1}. This value was more than 15-fold higher than in bolus-loaded neurons (see below), indicating a rapid diffusional exchange between the soma and the pipette as described previously (Pusch & Neher, 1988). In AM-ester loaded cells, recovery from somatic sodium transients was considerably slower, reaching a maximum rate of ∼8 mM min^{-1} under control conditions. This peak rate is in the same range as those reported from cultured myocytes (Despa & Bers, 2003; Despa *et al.* 2004).

The recovery rate was dependent on the intracellular sodium concentration and a Hill plot revealed an apparent K_M of 19 mM with saturation above 30 mM. Recovery was completely blocked in the presence of ouabain, indicating that it was mediated by the export of sodium through NKA. Because NKA activity (but not diffusion) is highly temperature-sensitive, the dominating role of the NKA in sodium extrusion from somata was supported by the observation that an increase in the temperature by 10 °C accelerated the recovery rates by a factor of two (den Hertog & Ritchie, 1969; Skou & Esmann, 1992; Rose *et al.* 1999). Our simulation is in line with these experimental findings, predicting that NKA activity is required for recovery from somatic sodium loads.

Hippocampal neurons express two α-isoforms of the NKA, namely α1 and α3 (Sweadner, 1992). When expressed in HeLa cells, α1 has a low K_M for sodium (12 mM), whereas the K_M for sodium is 33 mM for α3 (Zahler *et al.* 1997). From these data, it was concluded that α1 sets baseline sodium concentrations and α3 specifically handles rapid recovery from large sodium increases in small compartments following neuronal activity (Munzer *et al.* 1994; Zahler *et al.* 1997). A recent study has provided evidence that α1 and α3 mediate functional sodium export from cultured rat neurons (Azarias *et al.* 2012), and the apparent K_M as determined in the present study (19 mM) probably reflects the activity of both isoforms. For dendrites, similar values for V_{max}, K_M and saturation were found, indicating a similar isoform expression profile as in somata.

NKA activity is strongly dependent on the availability of intracellular ATP and it is estimated that the pump consumes ∼50% of all the energy needed by the CNS (Ames, 2000). To challenge cellular metabolism, we inhibited glycolysis with NaF. This resulted in an increase in cellular MgG fluorescence, indicating an increase in free magnesium and suggesting a decrease in ATP as reported before (Chatton *et al.* 2003; Magistretti & Chatton, 2005; Fernandez-Moncada & Barros, 2014). NaF perfusion also resulted in a gradual impairment of recovery from glutamate-induced transient sodium loads, as well as in a gradual build-up of intracellular sodium in cell bodies, indicative of a reduction in NKA activity.

At an intact mitochondrial respiration, the prominent influence of inhibition of glycolysis on sodium export is at first surprising. Glycolysis produces only ∼5% of the cellular ATP (Erecinska & Silver, 1989), which will certainly not be sufficient to feed NKA. Inhibition of glycolysis, on the other hand, will ultimately result in a reduction of pyruvate and thereby also decrease the availability of substrates for the tricarboxylic acid cycle and for mitochondrial respiration. Along those lines, a previous study provided evidence that the NKA is mainly fuelled by ATP produced by oxidative phosphorylation (Fernandez-Moncada & Barros, 2014), which, in the light of the high energy demand of the NKA, indeed appears to be conclusive.

Recovery from sodium loads in dendrites

With focal puff application of glutamate, the maximum rate for sodium recovery in dendrites was in the same range as that of somata of whole-cell patch-clamped cells, and 10-fold higher that of the somata of non-patched cells. Although perfusion with ouabain resulted in an immediate increase in intracellular sodium in dendrites, indicating inhibition of NKA, recovery from local sodium transients was still largely intact and $V_{20–25}$ under this condition was almost unaltered. By contrast to what was seen in the soma, recovery from dendritic sodium transients was also almost unchanged upon an increase in temperature to 34°C. Our numerical simulation demonstrated the feasibility of this experimental finding, predicting a rapid return of locally-induced dendritic sodium transients to baseline even with pumps turned off.

These results strongly indicate that recovery from local sodium loads in dendrites is largely governed by lateral diffusion along the dendrite and independent from NKA activity. A similar result has been obtained in axon initial segments of layer 5 pyramidal neurons. Here, the recovery from action-potential induced sodium transients was not significantly altered by ouabain, indicating that sodium clearance was mainly mediated by passive diffusion (Fleidervish *et al.* 2010). Our experiments also revealed an estimate for sodium diffusion along primary dendrites. The resulting value of ∼330 μm^2 s^{-1} is around half that reported from frog muscle fibres (600 μm^2 s^{-1}), and significantly smaller than that of large lizard axons

(1300 $\mu m^2\ s^{-1}$) (David & Barrett & Barrett, 1997), indicating that diffusion in rodent dendrites is considerably hindered compared to the cell types and compartments described above.

The notion that fast diffusion dominates over NKA activity for recovery from local sodium transients in dendrites was also supported by experiments in which glutamate was applied non-focally to eliminate sodium gradients and diffusion. Under this condition, dendritic V_{max} dropped from 120 to ~16 mM min^{-1} and $V_{20–25}$ decreased from 80 to 15 mM min^{-1}, probably now primarily reflecting dendritic NKA activity. Calculated peak sodium fluxes in dendrites were ~10-fold higher than those obtained with glutamate application to the soma (0.33 *vs.* 0.03 mM min^{-1} μm^{-2}). Thus, although maximum extrusion rates (mM min^{-1}) are two-fold higher in dendrites compared to somata, this difference multiplies for sodium fluxes, indicating that the much larger surface-to-volume ratio in dendrites also bring about much higher absolute sodium export rates by the sodium pump.

In cultured rat hippocampal neurons, a recent study reported initial extrusion rates of 34 mM min^{-1} from dendrites obtained after removal of extracellular potassium to block NKA (Azarias *et al.* 2012), a value more than twice that obtained in the present study. This difference in the concentration-based extrusion rates might result from a different surface-to-volume ratio of the compartment under study. Thus, a given membrane transport activity will result in a slower recovery rate in a larger compared to a smaller cellular compartment (e.g. a finer dendrite).

A direct consequence of the dominance of diffusion *vs.* local extrusion in dendrites was the primary independence of local dendritic sodium transients on an intact glycolysis. In dendrites, application of NaF (which resulted in gradual failure of sodium export from cell bodies), neither affected the amplitude, nor the recovery of sodium transients induced by repetitive focal glutamate application induced within the same time frame. Again, when diffusion was hampered by non-focal application of glutamate, dendrites experienced a similar build-up of sodium and failure of sodium extrusion than somata. These data indicate that reduced ATP availability does not hamper recovery from local sodium loads in dendrites, at least in the time frame investigated in the present study. As a reverse conclusion, local sodium transients will not *per se* induce a local increase in ATP consumption and will thus not represent a significant local challenge for metabolism. Of course, and as indicated by our measurements, sodium ions entering the cytosol will ultimately be exported through the NKA if there is no diffusion gradient for sodium and/or if there is an overall increase in cytosolic sodium.

Functional consequences and conclusions

Excitatory neuronal activity causes large sodium transients in central neurons as a result of the opening of sodium-permeable voltage- and ligand-gated ion channels (Rose, 2002). These sodium transients can either be local, as is the case for local activation of glutamatergic synapses (Rose & Konnerth, 2001), encompass the entire dendritic tree as is the case for back-propagating action potentials (Jaffe *et al.* 1992; Rose *et al.* 1999), or even occur as global network oscillations as described during epileptiform activity (Karus *et al.* 2015*a*). The results reported in the present study show that recovery from these sodium transients is mediated by two central mechanisms: lateral intracellular diffusion to neighbouring, non-stimulated areas and extrusion through the plasma membrane by the NKA. The relative weight and the contribution of these two mechanisms depend on the form of activity and the cellular compartment.

Our data emphasize that the NKA is the central mechanism for export of sodium from neurons. For recovery from sodium transients, this general principle, is, however, only valid for cell bodies and for global sodium loads imposed on the entire cell. When its function is compromised, either by ouabain or by energy depletion, sodium homeostasis and recovery from additional sodium loads fail. In dendrites, after localized sodium influx, sodium is mainly removed by fast lateral diffusion. Consequently, our data also suggest that sodium increases in cellular microdomains, such as those generated during excitatory synaptic activity (Lasser-Ross & Ross, 1992; Knopfel *et al.* 2000; Rose & Konnerth, 2001; Bennay *et al.* 2008), will probably not require a local increase in ATP consumption, nor energy metabolism.

The concept of 'diffusion over extrusion' also implies that sodium recovery in dendrites is one order of magnitude faster than if it was mediated by local NKA activity only. Although sodium ions will be pumped out by the NKA at some point, our study thus suggests that energy requirements will not surge locally after a local sodium increase but rather be disseminated to and shared with the entire cell. However, when subjected to global cellular sodium increases, such as during synchronized epileptiform discharges, sodium recovery will be mediated by NKA only and even small-amplitude sodium increases will thus be maintained for a relatively long time as shown recently (Karus *et al.* 2015*a*). It can be assumed that, under such conditions, support of neuronal metabolism and sodium homeostasis by astrocytes will be especially critical (Allaman *et al.* 2011; Barros, 2013; Karus *et al.* 2015*a*). Moreover, an additional weakening or impairment of energy metabolism during global sodium increases will have direct and immediate consequences on the capacity of neurons to maintain low intracellular sodium (Karus *et al.* 2015*a*; Karus *et al.* 2015*b*) and thereby promote additional

fatal consequences such as the reversal of sodium-calcium exchange and calcium load (Hertz, 2008).

References

Allaman I, Belanger M & Magistretti PJ (2011). Astrocyte–neuron metabolic relationships: for better and for worse. *Trends Neurosci* **34**, 76–27.

Allbritton NL, Meyer T & Stryer L (1992). Range of messenger action of calcium ion and inositol 1,4,5-trisphosphate. *Science* **258**, 1812–2815.

Ames A, 3rd (2000). CNS energy metabolism as related to function. *Brain Res Brain Res Rev* **34**, 42–28.

Araya R, Eisenthal KB & Yuste R (2006). Dendritic spines linearize the summation of excitatory potentials. *Proc Natl Acad Sci USA* **103**, 18799–28804.

Ascoli GA, Donohue DE & Halavi M (2007). NeuroMorpho.Org: a central resource for neuronal morphologies. *J Neurosci* **27**, 9247–2251.

Astrup J, Sorensen PM & Sorensen HR (1981). Oxygen and glucose consumption related to Na^+-K^+ transport in canine brain. *Stroke* **12**, 726–230.

Azarias G, Kruusmagi M, Connor S, Akkuratov EE, Liu XL, Lyons D, Brismar H, Broberger C & Aperia A (2012). A specific and essential role for Na,K-ATPase alpha3 in neurons co-expressing alpha1 and alpha3. *J Biol Chem* **288**, 2734–2743.

Barros LF (2013). Metabolic signalling by lactate in the brain. *Trends Neurosci* **36**, 396–404.

Beguin S, Crepel V, Aniksztejn L, Becq H, Pelosi B, Pallesi-Pocachard E, Bouamrane L, Pasqualetti M, Kitamura K, Cardoso C & Represa A (2013). An epilepsy-related ARX polyalanine expansion modifies glutamatergic neurons excitability and morphology without affecting GABAergic neurons development. *Cereb Cortex* **23**, 1484–2494.

Bennay M, Langer J, Meier SD, Kafitz KW & Rose CR (2008). Sodium signals in cerebellar Purkinje neurons and Bergmann glial cells evoked by glutamatergic synaptic transmission. *Glia* **56**, 1138–2149.

Bizzozero OA, Sanchez P & Tetzloff SU (1999). Effect of ATP depletion on the palmitoylation of myelin proteolipid protein in young and adult rats. *J Neurochem* **72**, 2610–2616.

Capendeguy O & Horisberger J-D (2004). Functional effects of Na^+,K^+-ATPase gene mutations linked to familial hemiplegic migraine. *Neuromolecular medicine* **6**, 105–216.

Chatton JY, Marquet P & Magistretti PJ (2000). A quantitative analysis of L-glutamate-regulated Na^+ dynamics in mouse cortical astrocytes: implications for cellular bioenergetics. *Eur J Neurosci* **12**, 3843–2853.

Chatton JY, Pellerin L & Magistretti PJ (2003). GABA uptake into astrocytes is not associated with significant metabolic cost: implications for brain imaging of inhibitory transmission. *Proc Natl Acad Sci USA* **100**, 12456–22461.

Close B (1997). *Euthanasia of Experimental Animals*. Office for Official Publications of the European Communities, Luxembourg.

Cox DW & Bachelard HS (1982). Attenuation of evoked field potentials from dentate granule cells by low glucose, pyruvate + malate, and sodium fluoride. *Brain Res* **239**, 527–234.

David G, Barrett JN & Barrett EF (1997). Spatiotemporal gradients of intra-axonal [Na+] after transection and resealing in lizard peripheral myelinated axons. *J Physiol* **498**, 295–207.

De Carvalho Aguiar P, Sweadner KJ, Penniston JT, Zaremba J, Liu L, Caton M, Linazasoro G, Borg M, Tijssen MA, Bressman SB, Dobyns WB, Brashear A & Ozelius LJ (2004). Mutations in the Na^+/K^+-ATPase alpha3 gene ATP1A3 are associated with rapid-onset dystonia parkinsonism. *Neuron* **43**, 169–275.

den Hertog A & Ritchie JM (1969). A comparison of the effect of temperature, metabolic inhibitors and of ouabain on the electrogenic componen of the sodium pump in mammalian non-myelinated nerve fibres. *J Physiol* **204**, 523–238.

Despa S & Bers DM (2003). Na/K pump current and $[Na]_i$ in rabbit ventricular myocytes: local $[Na]_i$ depletion and na buffering. *Biophys J* **84**, 4157–2166.

Despa S, Islam MA, Weber CR, Pogwizd SM & Bers DM (2002). Intracellular Na(+) concentration is elevated in heart failure but Na/K pump function is unchanged. *Circulation* **105**, 2543–2548.

Despa S, Kockskamper J, Blatter LA & Bers DM (2004). Na/K pump-induced $[Na]_i$ gradients in rat ventricular myocytes measured with two-photon microscopy. *Biophys J* **87**, 1360–2368.

Diarra A, Sheldon C & Church J (2001). In situ calibration and $[H^+]$ sensitivity of the fluorescent Na^+ indicator SBFI. *Am J Physiol Cell Physiol* **280**, C1623–C2633.

Donoso P, Mill JG, O'Neill SC & Eisner DA (1992). Fluorescence measurements of cytoplasmic and mitochondrial sodium concentration in rat ventricular myocytes. *J Physiol* **448**, 493–209.

Erecinska M & Silver IA (1989). ATP and brain function. *J Cereb Blood Flow Metab* **9**, 2–29.

Erecinska M & Silver IA (1994). Ions and energy in mammalian brain. *Prog Neurobiol* **43**, 37–21.

Fernandez-Moncada I & Barros LF (2014). Non-preferential fuelling of the Na(+)/K(+)-ATPase pump. *Biochem J* **460**, 353–261.

Fleidervish IA, Lasser-Ross N, Gutnick MJ & Ross WN (2010). Na^+ imaging reveals little difference in action potential-evoked Na^+ influx between axon and soma. *Nat Neurosci* **13**, 852–260.

Grundy D (2015). Principles and standards for reporting animal experiments in *The Journal of Physiology and Experimental Physiology*. *J Physiol* **593**, 2547–2549.

Hallermann S, de Kock CP, Stuart GJ & Kole MH (2012). State and location dependence of action potential metabolic cost in cortical pyramidal neurons. *Nat Neurosci* **15**, 1007–2014.

Harootunian AT, Kao JP, Eckert BK & Tsien RY (1989). Fluorescence ratio imaging of cytosolic free Na^+ in individual fibroblasts and lymphocytes. *J Biol Chem* **264**, 19458–29467.

Harris JJ, Jolivet R & Attwell D (2012). Synaptic energy use and supply. *Neuron* **75**, 762–277.

Helmchen F, Imoto K & Sakmann B (1996). Ca^{2+} buffering and action potential-evoked Ca^{2+} signalling in dendrites of pyramidal neurons. *Biophys J* **70**, 1069–2081.

Helmchen F & Tank DW (2000). A single-compartment model of calcium dynamics in nerve terminals and dendrites. In *Imaging Neurons*, ed. Yuste R, Lanni F & Konnerth A, pp. **33**.31–23.11. Cold Spring Harbor Press, Cold Spring Harbor, NY.

Hertz L (2008). Bioenergetics of cerebral ischemia: a cellular perspective. *Neuropharmacology* **55**, 289–209.

Jaffe DB, Johnston D, Lasser-Ross N, Lisman JE, Miyakawa H & Ross WN (1992). The spread of Na^{+} spikes determines the pattern of dendritic Ca^{2+} entry into hippocampal neurons. *Nature* **357**, 244–246.

Jung DW, Apel LM & Brierley GP (1992). Transmembrane gradients of free Na^{+} in isolated heart mitochondria estimated using a fluorescent probe. *Am J Physiol Cell Physiol* **262**, C1047–C2055.

Kaplan JH (2002). Biochemistry of Na,K-ATPase. *Annu Rev Biochem* **71**, 511–235.

Karus C, Mondragao MA, Ziemens D & Rose CR (2015*a*). Astrocytes restrict discharge duration and neuronal sodium loads during recurrent network activity. *Glia* **63**, 936–257.

Karus C, Ziemens D & Rose CR (2015*b*). Lactate rescues neuronal sodium homeostasis during impaired energy metabolism. *Channels (Austin)* **9**, 200–208.

Kelly T & Rose CR (2010*a*). Ammonium influx pathways into astrocytes and neurones of hippocampal slices. *J Neurochem* **115**, 1123–2136.

Kelly T & Rose CR (2010*b*). Sodium signals and their significance for axonal function. In *New Aspects of Axonal Structure and Function*, ed. Feldmeyer D & Lübke JHR. Springer Verlag, Berlin.

Knopfel T, Anchisi D, Alojado ME, Tempia F & Strata P (2000). Elevation of intradendritic sodium concentration mediated by synaptic activation of metabotropic glutamate receptors in cerebellar Purkinje cells. *Eur J Neurosci* **12**, 2199–2204.

Kole MH, Ilschner SU, Kampa BM, Williams SR, Ruben PC & Stuart GJ (2008). Action potential generation requires a high sodium channel density in the axon initial segment. *Nat Neurosci* **11**, 178–286.

Kushmerick MJ & Podolsky RJ (1969). Ionic mobility in muscle cells. *Science* **166**, 1297–2298.

Lamy CM & Chatton JY (2011). Optical probing of sodium dynamics in neurons and astrocytes. *Neuroimage* **58**, 572–278.

Langer J & Rose CR (2009). Synaptically induced sodium signals in hippocampal astrocytes in situ. *J Physiol* **587**, 5859–2877.

Lasser-Ross N & Ross WN (1992). Imaging voltage and synaptically activated sodium transients in cerebellar Purkinje cells. *Proc Biol Sci* **247**, 35–29.

Lees GJ (1991). Inhibition of sodium-potassium-ATPase: a potentially ubiquitous mechanism contributing to central nervous system neuropathology. *Brain Res Brain Res Rev* **16**, 283–200.

Lennie P (2003). The cost of cortical computation. *Curr Biol* **13**, 493–297.

Levi AJ, Lee CO & Brooksby P (1994). Properties of the fluorescent sodium indicator 'SBFI' in rat and rabbit cardiac myocytes. *J Cardiovasc Electrophysiol* **5**, 241–257.

Leyssens A, Nowicky AV, Patterson L, Crompton M & Duchen MR (1996). The relationship between mitochondrial state, ATP hydrolysis, $[Mg^{2+}]_i$ and $[Ca^{2+}]_i$ studied in isolated rat cardiomyocytes. *J Physiol* **496**, 111–228.

Magistretti PJ & Chatton JY (2005). Relationship between L-glutamate-regulated intracellular Na^{+} dynamics and ATP hydrolysis in astrocytes. *J Neural Transm* **112**, 77–25.

Maravall M, Mainen ZF, Sabatini BL & Svoboda K (2000). Estimating intracellular calcium concentrations and buffering without wavelength ratioing. *Biophys J* **78**, 2655–2667.

Meier SD, Kafitz KW & Rose CR (2008). Developmental profile and mechanisms of GABA-induced calcium signalling in hippocampal astrocytes. *Glia* **56**, 1127–2137.

Meier SD, Kovalchuk Y & Rose CR (2006). Properties of the new fluorescent Na^{+} indicator CoroNa Green: comparison with SBFI and confocal Na^{+} imaging. *J Neurosci Methods* **155**, 251–259.

Minta A & Tsien RY (1989). Fluorescent indicators for cytosolic sodium. *J Biol Chem* **264**, 19449–29457.

Moseley AE, Williams MT, Schaefer TL, Bohanan CS, Neumann JC, Behbehani MM, Vorhees CV & Lingrel JB (2007). Deficiency in Na,K-ATPase alpha isoform genes alters spatial learning, motor activity, and anxiety in mice. *J Neurosci* **27**, 616–226.

Munzer JS, Daly SE, Jewell-Motz EA, Lingrel JB & Blostein R (1994). Tissue- and isoform-specific kinetic behaviour of the Na,K-ATPase. *J Biol Chem* **269**, 16668–26676.

Neher E (1995). The use of fura-2 for estimating Ca buffers and Ca fluxes. *Neuropharmacology* **34**, 1423–2442.

Neher E & Augustine GJ (1992). Calcium gradients and buffers in bovine chromaffin cells. *J Physiol* **450**, 273–201.

Pusch M & Neher E (1988). Rates of diffusional exchange between small cells and a measuring patch pipette. *Pflügers Arch* **411**, 204–211.

Rose CR (2002). Na^{+} signals at central synapses. *Neuroscientist* **8**, 532–239.

Rose CR & Konnerth A (2001). NMDA receptor-mediated Na^{+} signals in spines and dendrites. *J Neurosci* **21**, 4207–2214.

Rose CR, Kovalchuk Y, Eilers J & Konnerth A (1999). Two-photon Na^{+} imaging in spines and fine dendrites of central neurons. *Pflügers Arch* **439**, 201–207.

Rose CR & Ransom BR (1997). Regulation of intracellular sodium in cultured rat hippocampal neurones. *J Physiol* **499**, 573–287.

Sabatini BL, Maravall M & Svoboda K (2001). Ca(2+) signalling in dendritic spines. *Curr Opin Neurobiol* **11**, 349–256.

Schmidt H & Eilers J (2009). Spine neck geometry determines spino-dendritic cross-talk in the presence of mobile endogenous calcium binding proteins. *J Comput Neurosci* **27**, 229–243.

Schreiner AE & Rose CR (2012). Quantitative imaging of intracellular sodium. In *Current Microscopy Contributions to Advances in Science and Technology*, ed. Méndez-Vilas A, pp. 119–229. Formatex Research Centre, Badajoz.

Sheldon C, Cheng YM & Church J (2004). Concurrent measurements of the free cytosolic concentrations of H(+) and Na(+) ions with fluorescent indicators. *Pflügers Arch* **449**, 307–218.

Skou JC & Esmann M (1992). The Na,K-ATPase. *J Bioenerg Biomembr* **24**, 249–261.

Somjen GG (2002). Ion regulation in the brain: implications for pathophysiology. *Neuroscientist* **8**, 254–267.

Sweadner KJ (1989). Isozymes of the Na^+/K^+-ATPase. *Biochim Biophys Acta* **988**, 185–220.

Sweadner KJ (1992). Overlapping and diverse distribution of Na-K ATPase isozymes in neurons and glia. *Can J Physiol Pharmacol* **70 Suppl**, S255–S259.

Whittam R (1962). The dependence of the respiration of brain cortex on active cation transport. *Biochem J* **82**, 205–212.

Zahler R, Zhang ZT, Manor M & Boron WF (1997). Sodium kinetics of Na,K-ATPase alpha isoforms in intact transfected HeLa cells. *J Gen Physiol* **110**, 201–213.

Zhou Z & Neher E (1993). Mobile and immobile calcium buffers in bovine adrenal chromaffin cells. *J Physiol* **469**, 245–273.

Additional information

Competing interests

The authors declare that they have no competing interests.

Author contributions

All imaging experiments were performed at the Institute of Neurobiology, Heinrich Heine University Duesseldorf, Germany. Modelling was performed at the Carl-Ludwig-Institute for Physiology, Medical Faculty, University of Leipzig, Liebigstrasse 27, 04103 Leipzig, Germany. MAM, HS and CRR were responsible for the conception and design of the experiments. MAM, HS, JL, CK, KWK and CRR were responsible for the collection, assembly, analysis and interpretation of data. MAM, HS, JL, CK, KWK and CRR were responsible for drafting the article or revising it critically for important intellectual content. All authors contributed to critical revision of the manuscript for intellectual content and final approval of version to be published. All persons designed as authors qualify for authorship and all those who qualify for authorship are listed.

Funding

This work was supported by the Deutsche Forschungsgemeinschaft (German Research Foundation; Ro2327/6-1).

Acknowledgements

We thank Simone Durry and Claudia Roderigo for excellent technical assistance.

8.4 Rapid sodium signaling couples glutamate uptake to breakdown of ATP in perivascular astrocyte endfeet

Status: Eingereicht am 11.07.2016 in „The Journal of Neuroscience“.

Persönlicher Beitrag: 15%. Ich war an der Erstellung des Konzepts und der Durchführung eines Teils der Experimente beteiligt. Zur Analyse der zugehörigen Experimente und Interpretation der betreffenden Daten habe ich beigetragen.

The Journal of Neuroscience

http://jneurosci.msubmit.net

JN-RM-2196-16

Rapid sodium signaling couples glutamate uptake to breakdown of ATP in perivascular astrocyte endfeet

Julia Langer, University of Duesseldorf
Niklas Gerkau, University of Duesseldorf
Amin Derouche, University of Frankfurt
Christian Kleinhans, University of Duesseldorf
Behrouz Moshrefi-Ravasdjani, University of Duesseldorf
Michaela Fredrich, University of Frankfuert
Karl Kafitz, University of Duesseldorf
Gerald Seifert, University of Bonn
Christian Steinhaeuser, University of Bonn
Christine Rose, University of Duesseldorf

9 Danksagung

Ich bedanke mich mit der größtmöglichen Herzlichkeit bei Frau Prof. Dr. Christine Rose, die mich als Fachfremden in ihre Arbeitsgruppe aufgenommen und mir ein großes Maß an Vertrauen entgegengebracht hat. So war es mir möglich, in diesem hochaktuellen und interessanten Fachgebiet diese Arbeit anzufertigen. Mit aller gebotenen Bescheidenheit kann ich sagen: Ich habe viel gelernt. Auch die zahllosen Gespräche und Diskussionen waren stets motivierend und hilfreich.

Ein besonderer Dank gilt Herrn Prof. Dr. Kurt Gottmann für die Übernahme des Koreferats und des Mentorings sowie die hilfreichen Hinweise beim Verfassen dieser Arbeit.

Herrn Dr. Karl Kafitz möchte ich nicht nur für die hervorragende fachliche Betreuung, sondern auch die Bereitstellung und Pflege einer technischen Infrastruktur danken, die weit über das Selbstverständliche hinausgeht. Seine Hilfsbereitschaft, die nicht auf das Institut beschränkt war, war außergewöhnlich. Auch die ein oder andere heitere Bastelstunde im „Zweiphotonen“ wird mir in Erinnerung bleiben.

Ein großer Dank geht an ein wahres Multitalent, Herrn Dr. Peter Hochstrate. Er beweist, dass sich eine akademische Laufbahn und der Erfolg als Youtube-Star, Comiczeichner, Schulbuchautor („Physik – frei von Zahlen, nah am Menschen, für Europa“) und Conférencier nicht ausschließen muss. Seine naturwissenschaftliche Beschlagenheit, sein didaktisches Geschick, allen voran aber seine Persönlichkeit werden mir stets ein Vorbild sein.

Ich danke Claudia Roderigo und Simone Durry für die Hilfe im Labor und für den andauernden Kampf gegen Murphy’s Law, das uns sonst sicher öfter zum Verhängnis geworden wäre. Tanja Schöttler sei gedankt für die Hilfe in so ziemlich jeder bürokratischen Frage, aber auch für den ein oder anderen gewohnt liebenswert vorgetragenen Ordnungsruf. Es war mir eine Freude! Auch Fatma Demir möchte ich für die Hilfe danken, ebenso wie für die verschiedenen kulinarischen Köstlichkeiten.

Vielen Dank an diejenigen Kollegen, die mich als bereits erfahrene Experimentatoren eingearbeitet haben und von denen ich sehr viel lernen durfte: Dr. Julia Langer, zurecht Trägerin des goldenen Auslassungszeichens der Deutschen Antizipativen Gesellschaft, und Dr. Jonathan Stephan, der jedem Preußen in Sachen Korrektheit spielend noch etwas vormachen kann. Ein ebenso herzliches Dankeschön geht an die werten Kollegen, die mein Schicksal als Promotionsstudent mit mir geteilt haben. Danke an Dr. Claudia Karus für die schönsten Duette der Laborgeschichte, Behrouz Moshrefi für seine Pubquiztaugliche Allgemeinbildung, Niklas Gerkau für die geopferten Nerven, Daniel „Bengel“ Ziemens für allgemeinen Wahnsinn, Dr. Miguel Mondragao für seinen angenehmen Zynismus, Eric Berlinger für seinen Whiskysachverstand und Lennart Ramses Müller-Thomsen für den Pyramidenverleih.
Auch die zahlreichen Bachelor- und Masterstudenten, von denen viele kamen und einige gingen, haben zu einer äußerst angenehmen Atmosphäre beigetragen.

Für die Zeit im „Maison Herzog 21“, für die seit der 7. Klasse währende Freundschaft, für Geistreichtum und die Freude am distinguierten Herrenwitz, für die Duelle in Frank’s Billardcafé und einiges mehr möchte ich Herrn Dr. Georg Oeltzschner meine größte Reverenz erweisen.

Meiner Freundin Dana kann ich kaum genug danken für das Verständnis, die Rücksichtnahme und die Zuneigung, ohne die ich nicht nur diese Arbeit nie geschafft hätte. Danke für jede gemeinsam verbrachte Minute!

Ich danke meiner Familie, allen Freunden, Mitstreitern und Leidensgenossen, die namentlich unerwähnt geblieben, aber immer wertgeschätzt sind.

Schließlich bedanke ich mich bei meinen Eltern, auf die ich immer und überall zählen kann. Was wäre ich ohne Euch.

10 Referenzen

Adrian M, Kusters R, Wierenga CJ, Storm C, Hoogenraad CC, Kapitein LC (2014) Barriers in the brain: resolving dendritic spine morphology and compartmentalization. Frontiers in neuroanatomy 8:142.

Allbritton NL, Meyer T, Stryer L (1992) Range of messenger action of calcium ion and inositol 1,4,5-trisphosphate. Science 258:1812-1815.

Alvarez VA, Sabatini BL (2007) Anatomical and physiological plasticity of dendritic spines. Annual review of neuroscience 30:79-97.

Araque A, Parpura V, Sanzgiri RP, Haydon PG (1999) Tripartite synapses: glia, the unacknowledged partner. Trends in neurosciences 22:208-215.

Araya R, Eisenthal KB, Yuste R (2006a) Dendritic spines linearize the summation of excitatory potentials. Proceedings of the National Academy of Sciences of the United States of America 103:18799-18804.

Araya R, Vogels TP, Yuste R (2014) Activity-dependent dendritic spine neck changes are correlated with synaptic strength. Proceedings of the National Academy of Sciences of the United States of America 111:E2895-2904.

Araya R, Jiang J, Eisenthal KB, Yuste R (2006b) The spine neck filters membrane potentials. Proceedings of the National Academy of Sciences of the United States of America 103:17961-17966.

Araya R, Nikolenko V, Eisenthal KB, Yuste R (2007) Sodium channels amplify spine potentials. Proceedings of the National Academy of Sciences of the United States of America 104:12347-12352.

Arellano JI, Benavides-Piccione R, Defelipe J, Yuste R (2007) Ultrastructure of dendritic spines: correlation between synaptic and spine morphologies. Front Neurosci 1:131-143.

Azarias G, Kruusmagi M, Connor S, Akkuratov EE, Liu XL, Lyons D, Brismar H, Broberger C, Aperia A (2012) A specific and essential role for Na,K-ATPase alpha3 in neurons co-expressing alpha1 and alpha3. The Journal of biological chemistry.

Baartscheer A, Schumacher CA, Fiolet JW (1997) Small changes of cytosolic sodium in rat ventricular myocytes measured with SBFI in emission ratio mode. Journal of molecular and cellular cardiology 29:3375-3383.

Bailey CH, Kandel ER, Harris KM (2015) Structural Components of Synaptic Plasticity and Memory Consolidation. Cold Spring Harb Perspect Biol 7.

Baranauskas G, David Y, Fleidervish IA (2013) Spatial mismatch between the Na+ flux and spike initiation in axon initial segment. Proceedings of the National Academy of Sciences of the United States of America 110:4051-4056.

Biess A, Korkotian E, Holcman D (2007) Diffusion in a dendritic spine: the role of geometry. Physical review E, Statistical, nonlinear, and soft matter physics 76:021922.

Biess A, Korkotian E, Holcman D (2011) Barriers to diffusion in dendrites and estimation of calcium spread following synaptic inputs. PLoS computational biology 7:e1002182.

Blom H, Ronnlund D, Scott L, Spicarova Z, Widengren J, Bondar A, Aperia A, Brismar H (2011) Spatial distribution of Na+-K+-ATPase in dendritic spines dissected by nanoscale superresolution STED microscopy. BMC Neurosci 12:16.

Bloodgood BL, Giessel AJ, Sabatini BL (2009) Biphasic synaptic Ca influx arising from compartmentalized electrical signals in dendritic spines. PLoS Biol 7:e1000190.

Bosch M, Castro J, Saneyoshi T, Matsuno H, Sur M, Hayashi Y (2014) Structural and molecular remodeling of dendritic spine substructures during long-term potentiation. Neuron 82:444-459.

Bourne JN, Harris KM (2008) Balancing structure and function at hippocampal dendritic spines. Annual review of neuroscience 31:47-67.

Bywalez WG, Patirniche D, Rupprecht V, Stemmler M, Herz AV, Palfi D, Rozsa B, Egger V (2015) Local postsynaptic voltage-gated sodium channel activation in dendritic spines of olfactory bulb granule cells. Neuron 85:590-601.
Dao L, Glancy B, Lucotte B, Chang LC, Balaban RS, Hsu LY (2015) A Model-based approach for microvasculature structure distortion correction in two-photon fluorescence microscopy images. Journal of microscopy 260:180-193.
David G, Barrett JN, Barrett EF (1997) Spatiotemporal gradients of intra-axonal [Na+] after transection and resealing in lizard peripheral myelinated axons. The Journal of physiology 498 (Pt 2):295-307.
Denk W, Strickler JH, Webb WW (1990) Two-photon laser scanning fluorescence microscopy. Science 248:73-76.
Denk W, Sugimori M, Llinas R (1995) Two types of calcium response limited to single spines in cerebellar Purkinje cells. Proceedings of the National Academy of Sciences of the United States of America 92:8279-8282.
Diaspro A, Bianchini P, Vicidomini G, Faretta M, Ramoino P, Usai C (2006) Multi-photon excitation microscopy. Biomedical engineering online 5:36.
Ellis-Davies GC (2007) Caged compounds: photorelease technology for control of cellular chemistry and physiology. Nature methods 4:619-628.
Fleidervish IA, Lasser-Ross N, Gutnick MJ, Ross WN (2010) Na+ imaging reveals little difference in action potential-evoked Na+ influx between axon and soma. Nature neuroscience 13:852-860.
Garcia-Lopez P, Garcia-Marin V, Freire M (2007) The discovery of dendritic spines by Cajal in 1888 and its relevance in the present neuroscience. Progress in neurobiology 83:110-130.
Grunditz A, Holbro N, Tian L, Zuo Y, Oertner TG (2008) Spine neck plasticity controls postsynaptic calcium signals through electrical compartmentalization. The Journal of neuroscience : the official journal of the Society for Neuroscience 28:13457-13466.
Gu L, Kleiber S, Schmid L, Nebeling F, Chamoun M, Steffen J, Wagner J, Fuhrmann M (2014) Long-term in vivo imaging of dendritic spines in the hippocampus reveals structural plasticity. The Journal of neuroscience : the official journal of the Society for Neuroscience 34:13948-13953.
Harnett MT, Makara JK, Spruston N, Kath WL, Magee JC (2012) Synaptic amplification by dendritic spines enhances input cooperativity. Nature 491:599-602.
Harris KM, Jensen FE, Tsao B (1992) Three-dimensional structure of dendritic spines and synapses in rat hippocampus (CA1) at postnatal day 15 and adult ages: implications for the maturation of synaptic physiology and long-term potentiation. The Journal of neuroscience : the official journal of the Society for Neuroscience 12:2685-2705.
Hell SW (2007) Far-field optical nanoscopy. Science 316:1153-1158.
Helmchen F, Denk W (2005) Deep tissue two-photon microscopy. Nature methods 2:932-940.
Holcman D, Schuss Z (2011) Diffusion laws in dendritic spines. Journal of mathematical neuroscience 1:10.
Holtmaat A, Svoboda K (2009) Experience-dependent structural synaptic plasticity in the mammalian brain. Nature reviews Neuroscience 10:647-658.
Karus C, Ziemens D, Rose CR (2015a) Lactate rescues neuronal sodium homeostasis during impaired energy metabolism. Channels (Austin) 9:200-208.
Karus C, Mondragao MA, Ziemens D, Rose CR (2015b) Astrocytes restrict discharge duration and neuronal sodium loads during recurrent network activity. Glia 63:936-957.
Kelly T, Rose CR (2010) Ammonium influx pathways into astrocytes and neurones of hippocampal slices. J Neurochem 115:1123-1136.
Kim SJ, Linden DJ (2007) Ubiquitous plasticity and memory storage. Neuron 56:582-592.

Kleinhans C, Kafitz KW, Rose CR (2014) Multi-photon intracellular sodium imaging combined with UV-mediated focal uncaging of glutamate in CA1 pyramidal neurons. J Vis Exp:e52038.
Koch C, Zador A (1993) The function of dendritic spines: devices subserving biochemical rather than electrical compartmentalization. The Journal of neuroscience : the official journal of the Society for Neuroscience 13:413-422.
Korkotian E, Holcman D, Segal M (2004a) Dynamic regulation of spine-dendrite coupling in cultured hippocampal neurons. Eur J Neurosci 20:2649-2663.
Korkotian E, Oron D, Silberberg Y, Segal M (2004b) Confocal microscopic imaging of fast UV-laser photolysis of caged compounds. Journal of neuroscience methods 133:153-159.
Kushmerick MJ, Podolsky RJ (1969) Ionic mobility in muscle cells. Science 166:1297-1298.
Lobo VM (1993) Mutual diffusion coefficients in aqueous electrolyte solutions. Pure & Appl Chem 65:2613-2640.
Loew LM, Hell SW (2013) Superresolving dendritic spines. Biophysical journal 104:741-743.
Lorincz A, Rozsa B, Katona G, Vizi ES, Tamas G (2007) Differential distribution of NCX1 contributes to spine-dendrite compartmentalization in CA1 pyramidal cells. Proceedings of the National Academy of Sciences of the United States of America 104:1033-1038.
Magee JC (2000) Dendritic integration of excitatory synaptic input. Nature reviews Neuroscience 1:181-190.
Malenka RC (1994) Synaptic plasticity in the hippocampus: LTP and LTD. Cell 78:535-538.
Matsuzaki M, Honkura N, Ellis-Davies GC, Kasai H (2004) Structural basis of long-term potentiation in single dendritic spines. Nature 429:761-766.
McKenzie S, Eichenbaum H (2011) Consolidation and reconsolidation: two lives of memories? Neuron 71:224-233.
Meier SD, Kovalchuk Y, Rose CR (2006) Properties of the new fluorescent Na+ indicator CoroNa Green: comparison with SBFI and confocal Na+ imaging. Journal of neuroscience methods 155:251-259.
Meyer D, Bonhoeffer T, Scheuss V (2014) Balance and stability of synaptic structures during synaptic plasticity. Neuron 82:430-443.
Minta A, Tsien RY (1989) Fluorescent indicators for cytosolic sodium. The Journal of biological chemistry 264:19449-19457.
Nagerl UV, Willig KI, Hein B, Hell SW, Bonhoeffer T (2008) Live-cell imaging of dendritic spines by STED microscopy. Proceedings of the National Academy of Sciences of the United States of America 105:18982-18987.
Neumann E, Toensing K, Kakorin S, Budde P, Frey J (1998) Mechanism of electroporative dye uptake by mouse B cells. Biophysical journal 74:98-108.
Nevian T, Helmchen F (2007) Calcium indicator loading of neurons using single-cell electroporation. Pflugers Archiv : European journal of physiology 454:675-688.
Nimchinsky EA, Sabatini BL, Svoboda K (2002) Structure and function of dendritic spines. Annual review of physiology 64:313-353.
Nobelprize.org (2014) The Nobel Prize in Chemistry 2014. In: http://www.nobelprize.org/nobel_prizes/chemistry/laureates/2014/.
Noguchi J, Matsuzaki M, Ellis-Davies GC, Kasai H (2005) Spine-neck geometry determines NMDA receptor-dependent Ca2+ signaling in dendrites. Neuron 46:609-622.
Olofsson J, Nolkrantz K, Ryttsen F, Lambie BA, Weber SG, Orwar O (2003) Single-cell electroporation. Current opinion in biotechnology 14:29-34.
Palma-Cerda F, Auger C, Crawford DJ, Hodgson AC, Reynolds SJ, Cowell JK, Swift KA, Cais O, Vyklicky L, Corrie JE, Ogden D (2012) New caged neurotransmitter analogs selective for glutamate receptor sub-types based on methoxynitroindoline and nitrophenylethoxycarbonyl caging groups. Neuropharmacology 63:624-634.

Periasamy A, Skoglund P, Noakes C, Keller R (1999) An evaluation of two-photon excitation versus confocal and digital deconvolution fluorescence microscopy imaging in Xenopus morphogenesis. Microscopy research and technique 47:172-181.
Rose CR, Konnerth A (2001) NMDA receptor-mediated Na+ signals in spines and dendrites. The Journal of neuroscience : the official journal of the Society for Neuroscience 21:4207-4214.
Rose CR, Kovalchuk Y, Eilers J, Konnerth A (1999) Two-photon Na+ imaging in spines and fine dendrites of central neurons. Pflugers Archiv : European journal of physiology 439:201-207.
Ryttsen F, Farre C, Brennan C, Weber SG, Nolkrantz K, Jardemark K, Chiu DT, Orwar O (2000) Characterization of single-cell electroporation by using patch-clamp and fluorescence microscopy. Biophysical journal 79:1993-2001.
Sabatini BL, Oertner TG, Svoboda K (2002) The life cycle of Ca(2+) ions in dendritic spines. Neuron 33:439-452.
Sala C, Segal M (2014) Dendritic spines: the locus of structural and functional plasticity. Physiol Rev 94:141-188.
Schmidt H, Eilers J (2009) Spine neck geometry determines spino-dendritic cross-talk in the presence of mobile endogenous calcium binding proteins. J Comput Neurosci 27:229-243.
Schreiner AE, Rose CR (2013) Quantitative Imaging of Intracellular Sodium. In: Current Microscopy Contributions to Advances in Science and Technology (Méndez-Vilas A, ed), pp 119-129. Badajoz, Spain: Formatex.
Segal M, Vlachos A, Korkotian E (2010) The spine apparatus, synaptopodin, and dendritic spine plasticity. The Neuroscientist : a review journal bringing neurobiology, neurology and psychiatry 16:125-131.
Soler-Llavina GJ, Sabatini BL (2006) Synapse-specific plasticity and compartmentalized signaling in cerebellar stellate cells. Nature neuroscience 9:798-806.
Spacek J, Harris KM (1997) Three-dimensional organization of smooth endoplasmic reticulum in hippocampal CA1 dendrites and dendritic spines of the immature and mature rat. The Journal of neuroscience : the official journal of the Society for Neuroscience 17:190-203.
Stosiek C, Garaschuk O, Holthoff K, Konnerth A (2003) In vivo two-photon calcium imaging of neuronal networks. Proceedings of the National Academy of Sciences of the United States of America 100:7319-7324.
Strange BA, Witter MP, Lein ES, Moser EI (2014) Functional organization of the hippocampal longitudinal axis. Nature reviews Neuroscience 15:655-669.
Svoboda K, Tank DW, Denk W (1996) Direct measurement of coupling between dendritic spines and shafts. Science 272:716-719.
Takasaki K, Sabatini BL (2014) Super-resolution 2-photon microscopy reveals that the morphology of each dendritic spine correlates with diffusive but not synaptic properties. Frontiers in neuroanatomy 8:29.
Tønnesen J, Katona G, Rozsa B, Nagerl UV (2014) Spine neck plasticity regulates compartmentalization of synapses. Nature neuroscience 17:678-685.
Trigo FF, Corrie JE, Ogden D (2009) Laser photolysis of caged compounds at 405 nm: photochemical advantages, localisation, phototoxicity and methods for calibration. Journal of neuroscience methods 180:9-21.
Tsay D, Yuste R (2004) On the electrical function of dendritic spines. Trends in neurosciences 27:77-83.
Wang M, Orwar O, Olofsson J, Weber SG (2010) Single-cell electroporation. Analytical and bioanalytical chemistry 397:3235-3248.
Wiegert JS, Oertner TG (2013) Long-term depression triggers the selective elimination of weakly integrated synapses. Proceedings of the National Academy of Sciences of the United States of America 110:E4510-4519.

Wijetunge LS, Angibaud J, Frick A, Kind PC, Nagerl UV (2014) Stimulated emission depletion (STED) microscopy reveals nanoscale defects in the developmental trajectory of dendritic spine morphogenesis in a mouse model of fragile X syndrome. The Journal of neuroscience : the official journal of the Society for Neuroscience 34:6405-6412.

Xin WK, Kwan CL, Zhao XH, Xu J, Ellen RP, McCulloch CA, Yu XM (2005) A functional interaction of sodium and calcium in the regulation of NMDA receptor activity by remote NMDA receptors. The Journal of neuroscience : the official journal of the Society for Neuroscience 25:139-148.

Yamanaka M, Smith NI, Fujita K (2014) Introduction to super-resolution microscopy. Microscopy (Oxf) 63:177-192.

Yuste R (2013) Electrical compartmentalization in dendritic spines. Annual review of neuroscience 36:429-449.

Yuste R, Denk W (1995) Dendritic spines as basic functional units of neuronal integration. Nature 375:682-684.

Yuste R, Bonhoeffer T (2001) Morphological changes in dendritic spines associated with long-term synaptic plasticity. Annual review of neuroscience 24:1071-1089.

Zipfel WR, Williams RM, Webb WW (2003) Nonlinear magic: multiphoton microscopy in the biosciences. Nature biotechnology 21:1369-1377.

Erklärung des Autors

Hiermit versichere ich, dass ich die vorliegende Arbeit selbständig angefertigt und keine anderen Hilfsmittel und Quellen verwendet habe als die erlaubten. Textstellen oder Abbildungen, die wörtlich oder abgewandelt aus anderen Arbeiten stammen, habe ich mit einer Quellenangabe versehen. Diese Arbeit wurde weder vollständig noch in Teilen einem anderen Prüfungsamt zur Erlangung eines akademischen Grades vorgelegt.

Christian Kleinhans Datum